ANL/HEP 7364

97,268

Measurement of the Differential Cross Section at 3, 4, 5, 6 GeV/c for the Reactions $\pi^- p \to K^o \Lambda^o$ and $\pi^- p \to K^o \Sigma^o$ and of Λ^o Polarization at 5 GeV/c*

ABRAHAM LESNIK+

The Department of Physics

The University of Chicago

Chicago, Illinois 60637

and

High Energy Physics Division

Argonne National Laboratory

Argonne, Illinois 60439

December, 1973

*Work supported by the U. S. Atomic Energy Commission

+A thesis submitted to The Department of Physics, The University of Chicago, in partial fulfillment of the requirements for the Ph. D. Degree.
Present address: Department of Physics, Ohio State University, Columbus, OH 43210

TABLE OF CONTENTS

ACKNOWLEDGMENT 1

LIST OF TABLES 3

LIST OF ILLUSTRATIONS 4

ABSTRACT 7

Chapter

I. INTRODUCTION AND THEORETICAL FRAMEWORK 8

I. Historical Framework
II. Introduction and Motivation for Experiment
A. Experimental
B. Theoretical
III. Theoretical Background
A. Variables
B. Crossing Symmetry and OPE
C. Peripheral Model
D. OPE and Regge Theory
E. Phenomenology and Peripheral Model
F. SU(3) Symmetry
G. Applications of SU(3)
1. Barger-Cline Sum Rule
2. Dual Absorptive Model
H. Input for Amplitude Analysis

II. RESOLUTION AND EXPERIMENTAL METHOD 26

I. General Description
II. Event Identification and Analysis
III. Resolution
IV. Experimental Apparatus
A. Beam Spectrometer
B. Electronics and Logic
C. Spark Chambers
1. Magnetostrictive readout
D. Data Transmission
E. On-line Computer
1. Complete on-line analysis
F. Programs
1. General description
2. Detailed descriptions
3. Momentum analysis

III. DATA AND ERROR ANALYSIS 64

I. Introduction
II. Corrections Derived from the Data
A. Corrections to the Beam Flux
B. Program Efficiencies
1. Reconstruction efficiency
2. Momentum analysis efficiency
3. Track coalescence
C. Kinematic Ambiguity
D. Background
1. t-dependence
2. Inelastics
E. Hypothesis Failures
III. Corrections Independent of Data
A. Acceptance
B. Double Counting; Decays and Absorption
C. Consistency Checks

IV. POLARIZATION MEASUREMENT AND ERROR ANALYSIS 113

I. Introduction
A. Calculation of Polarization
II. Sources of Error
A. Survey
B. Non-Uniform Efficiencies
C. Scattering Plane Errors
III. Overall Check Using Four-Constraint Fit
A. Detection Efficiency
B. Calibration of Angle Measurements
IV. Conclusion

V. PRESENTATION OF RESULTS AND DISCUSSION 130

I. Features of the Data
A. Diffraction Peak
B. Energy Dependence
C. Break in $\frac{d\sigma}{dt}$ at $\sim .4$
D. No Turnover of $\frac{d\sigma}{dt}$ at Small t
II. I = 1/2 Exchange
III. Models
IV. Qualitative Observations

APPENDIX 150

LIST OF REFERENCES 155

ACKNOWLEDGMENT

I am indebted to many people for their help in the course of this work, and it is a pleasure to acknowledge here those with whom I have worked most closely.

It has been my good fortune to have had the benefit of guidance and support from my thesis advisor, Dr. Drasko Jovanovic, and to have had the opportunity to learn from him ways of approaching the technical and physics problems in experimental high energy physics. I thank him also for his good humor and for many enlightening discussions, not all restricted to the subject of physics.

Dr. Charlie Ward has been a valuable collaborator. His scrupulous attention to the many problems that arose in the course of the experiment was certainly appreciated. The on-line software package for the EMR-6050 computer was the result of his efforts.

I have enjoyed working with Dr. Dave Rust, whose ingenuity made possible major components of our apparatus, and who originated the amplitude analysis for the Λ^o and Σ^o reactions.

A rare sense of old world craftsmanship and care marks every piece of equipment designed and built by Ivars Ambats. I also thank Ivars for introducing me to the new art form of epoxy sculpture.

Thanks are due Dr. Tom Meyer for valuable work on the acceptance calculation and for assistance throughout the experiment. Tom's experience with small French cars was also a valuable lesson for our entire group.

I would also like to thank our collaborators in the construction of the effective mass spectrometer: Dr. R. E. Diebold, Dr. D. S. Ayres, Dr. A. F. Greene, Dr. S. L. Kramer, and Dr. A. B. Wicklund. Particular thanks to Barry Wicklund for developing the precise and fast momentum analysis program used in our experiment, and also for many interesting discussions.

I am indebted to Mrs. Barb Perington for her fine work in typing this thesis, and for putting up with me throughout that arduous task. Thanks are due the staff and operating personnel of the ZGS for their continuing support during all phases of the experiment.

I am pleased to thank Professor Roland Winston for his sponsorship and assistance.

Thanks are due Professor Carl W. Akerlof of the University of Michigan whose original work on the EMR-6050 computer programs formed the basis, in part, from which our system was developed.

Finally, I want to express my love and thanks to my family, which is my pride and joy, wife Bonita and son Julian.

LIST OF TABLES

Table		Page
1.	Compilation of Data on Hypercharge Exchange	9
2.	Corrections for Λ^o, Σ^o Cross Contamination and Cuts on Missing Mass	35
3.	Program Inefficiencies found by Scanning	68
4.	FITT Program Inefficiency (Scanning)	73
5.	Summary of Corrections Applied to the Data	103
6.	The Measured Differential Cross Sections, $K^o\Lambda^o/\Sigma^o$	132
7.	The Measured Λ^o Polarization at 5 Gev/c	134
8.	Slope A and Intercept b in $d\sigma/dt=Ae^{bt}$	137
9.	Peripheral Total Cross Sections	138

LIST OF ILLUSTRATIONS

Figure		Page
1.	High Energy Scattering Diagrams	15
2.	Experimental Tests of the Barger-Cline Sum Rule, Differential and Total Cross Sections	23
3.	Experimental Layout	27
4.	Effective Mass Distributions for $\pi^+\pi^-$	29
5.	Missing Mass Distributions	30
6.	Fit to the Missing Mass Distribution	34
7.	Beam Spectrometer	37
8.	Momentum Hodoscope Distributions	38
9.	Hand Drawn Curves through Momentum Hodoscope Distributions	40
10.	Wire Spark Chamber, Expanded View	43
11.	CRT Display of the Apparatus	53
12.	Resolution of Momentum Analysis Program	63
13.	K^o Effective Mass Distribution for Large and Normal FITT χ^2 Values	70
14.	Number of Reconstructed K^o's as Function of $\pi^+\pi^-$ Horizontal Track Separation	75
15.	Reconstructed K^o's vs. Track Separation, Inclined Readout View	77
16.	Study of e^+e^- Effective Mass as Source of Contamination	79
17.	K^o and Λ^o Effective Mass for Front Coalesced Events.	80
18.	K^o, Λ^o Cross Contamination Studies--K^o Effective Mass	82

19. K^o, Λ^o Cross Contamination Studies--Λ^o Effective Mass for Events Identified as K^o's 83

20. K^o, Λ^o Cross Contamination Studies--Missing Mass from Λ^o's in Figure 19 84

21. Missing Mass from Λ^o's in Figure 19, Hypothesized as K^o's 85

22. t-dependence Studies of Background. K^o Missing Mass for t above and below $|t| = .2$, 3 GeV/c 87

23. t-dependence Studies at 6 GeV/c 88

24. Inelastic Contamination Studies. 90

25. Hypothesis Failure Studies; e^+e^- Effective Mass for Events not Fitting K^o, Λ^o Hypothesis 92

26. Vertex Distribution along the Beam Axis for e^+e^- Events in Figure 25 93

27. Detection Efficiency Due to Λ^o Decay in $\pi^-p \to K^o\Lambda^o$, Effect of Energy Loss 98

28. Monte Carlo Acceptance 99

29. Decay Correction vs. Program Inefficiencies. 104

30. Final Program Corrections. 105

31. Mode 1 Acceptance 106

32. Mode 3 Acceptance 109

33. Mode 1 and Mode 3 Acceptance Normalized to Agree at Large $|t|$. 110

34. Comparison of $d\sigma/dt$ Data for Mode 1 and Mode 3 Running Conditions 111

35. Angular Deviation of Elastic Scatter Tracks, (Predicted-Measured) 116

36. Horizontal Angular Deviations for Elastic Scattering Tracks 117

37. Vertical Angular Deviations for Elastic Scattering Tracks 118

38. Frequency of Tracks vs. Position in the Side Spark Chambers 120

39. Events vs. $\frac{\cos\theta}{\cos\theta_{max}}$, where $\cos\theta = \hat{p}_{Lambda} \cdot \hat{p}_{proton}$ Ratio of Measured Angle to Maximum Possible Laboratory Decay Angle, for $|t| < .25$ 121

40. Same as Figure 39, for Events with $|t| > .25$ 122

41. Distribution of Proton Decay Angles for $\Lambda^o \to p\pi^-$, Measured in the Λ^o Center of Mass Frame, where the Λ^o was Produced in $\pi^- p \to K^o \Lambda^o$ 124

42. Same as Figure 41, where the Nine Distributions Show Events having Ranges in t between $|t| \leq .1$ and $|t| \geq .7$. 125

43. The Decay $\Lambda^o \to p\pi^-$. Deviations of the Calculated Angles (Obtained by a Four-Constraint Fit) from the Measured Angles 127

44. Differential Cross Sections $d\sigma/dt$ for $\pi^- p \to K^o \Lambda^o$, $\pi^- p \to K^o \Sigma^o$ 131

45. Λ^o Polarization in $\pi^- p \to K^o \Lambda^o$ at 5 GeV/c Incident Beam Momentum 133

46. The Slope Parameter b in $\frac{d\sigma}{dt} = Ae^{bt}$ for Hypercharge Exchange Reactions 135

47. The Total Peripheral Cross Section $\sigma_{tot} = \int_{t_{min}}^{t_1} \frac{d\sigma}{dt} dt$ for Hypercharge Exchange Reactions. 136

48. Comparison of 4 GeV/c Data with Abramovich, Ref. 60. 140

49. Comparison of 6 GeV/c Data with Crennel, Ref. 61 . . 141

50. Comparison of Differential Cross Sections $\frac{d\sigma}{dt}$ of $\pi^- p \to K^o \Sigma^o$ and $\pi^+ p \to K^+ \Sigma^+$ 143

51. α_{eff}: Effective Regge Trajectories, from Ref. 64 . . 145

52. Elastic Scattering Data, $\frac{d\sigma}{dt}$, from Ref. 69 147

53. Elastic Scattering Data, Polarization, from Ref. 70 . 149

54. Amplitude Moduli and Phase Angle 154

ABSTRACT

The differential cross section in the reaction $\pi^- p \to K^o \Lambda^o$, $\pi^- p \to K^o \Sigma^o$ has been measured at incident beam momenta of 3, 4, 5, and 6 GeV/c and at momentum transfers to t $\sim$-2.0. The polarization of Λ^o has also been measured at 5 GeV/c using the parity violating decay $\Lambda^o \to p\pi^-$. Wire spark chambers with magnetostrictive readout, scintillators, and Cerenkov counters were used and most of the calculations were performed on-line with an EMR-6050 computer. Due to the experimental method our results, Figure 44 and Table 6, have much smaller error than previous bubble chamber measurements.

CHAPTER I

INTRODUCTION AND THEORETICAL FRAMEWORK

I. Historical Review

The period from 1944 to 1953 saw an accumulation of evidence[1] from cosmic ray data for the existence of particles having some puzzling properites.

i) The particles decayed to proton and π^-, also to $\pi^+\pi^-$, (the marked "V" pattern formed by the decay in cloud chambers resulted in the name "V-particles").

ii) The lifetime of the V particles ranged from 10^{-8} to 10^{-10} seconds.

iii) The V particles were produced in strong interactions.

What was "strange" about these particles was that they apparently violated the principle of microscopic reversibility.[2] A typical interaction time for strongly interacting particles was 10^{-23} sec., whereas the decay rates for the V particles was many orders of magnitude different. This principle had been used previously to show that the muon was not the strongly interacting meson predicted by Yukawa.

The hypothesis of "associated production" for V particles,

TABLE 1

MEASUREMENTS OF ASSOCIATED PRODUCTION REACTIONS

First author and date		Reaction ($\pi p \to$)	Detector (Chamber)	Energy (GeV)	Approx. # events
York	(1953)	$\Lambda^{o} \to p\pi^{-}$	Cloud	Cos. ray	2
Fowler	(1953)	$K\Lambda$	Cloud	1.4	9
Cowan	(1954)	$K\Lambda$	Cloud	Cos. ray	2
Walker	(1955)	$K\Lambda$	Cloud	1.0	2
Eisler	(1957)	$K\Lambda/\Sigma$	Bubble	0.91, 1.3	263
Brown	(1957)	$K\Lambda/\Sigma$	Bubble	1.1	60
Leipuner	(1958)	$K\Lambda/\Sigma$	Bubble	0.96	53
Crawford	(1959)	$K\Sigma$	Bubble	1.09	100
Bertanza	(1962)	$K\Lambda$	Bubble	0.77-0.87	1100
Keren	(1964)	$K\Lambda$	Bubble	1.02	1800
Wangler	(1965)	KY	Bubble	3.0	600
Kim	(1966)	$K\Lambda/\Sigma$	Spark	1.17, 1.32	1800
Goussu	(1966)	$K\Lambda/\Sigma$	Bubble	1.59	1000
Ehrlich	(1966)	KX	Bubble	7.91	800
Bartsch	(1966)	$K\Lambda/\Sigma$	Bubble	4.0	1500
Kobler	(1967)	$K\Lambda/\Sigma$	Bubble	3.23	380
Dahl	(1967)	$K\Lambda/\Sigma/Y^{*}$	Bubble	1.5-4.2	1500
Hoang	(1967)	$K\Lambda/\Sigma$	Spark	4.0	2200
Pruss	(1968)	$K\Sigma$	Spark	3.0-7.0	40000
Bertolucci	(1969)	KY	Spark	6.0-11.2	200
Abramovich	(1970)	$K\Lambda/\Sigma$	Bubble	3.9	3000
Kalbaci	(1971)	$K\Sigma/Y^{*}$	Spark	3.0-7.0	1000
Akerlof	(1971)	$K\Sigma$	Spark	5.0	1000
Bashian	(1972)	$K\Sigma/Y^{*}$	Spark	3.5-14.0	10000
Crennel	(1972)	$K\Lambda/\Sigma/Y^{*}$	Bubble	4.5, 6.0	3000
Foley	(1973)	$K\Lambda/\Sigma$	Spark	8.0-15.7	23000
This exp.	(1973)	$K\Lambda/\Sigma$	Spark	3.0-6.0	40000

proposed by Pais,[3] stated that only certain combinations of V particles could be produced in strong interactions. The first direct evidence for associated production came in a cloud chamber exposure by R. P. Shutt at the Berkeley Cosmotron in 1952. The great interest in the V-particles soon resulted in considerable experimental data.[4] Subsequently the introduction of the strangeness quantum number and the strangeness classification scheme of Gell-Mann and Nishijima[5] proved successful in correlating and explaining the data on associated production. Associated production thereafter became simply another example of an interesting class of reactions.

A variety of experimental techniques for measuring these reactions evolved over the years. The earliest observations were of cosmic ray interactions in cloud chambers. Subsequently, data was accumulated by means of cloud and bubble chambers at accelerators. More recently, counter experiments have measured associated production reactions. As an illustrative summary, we present Table 1.

This work describes a measurement of two associated production reactions using modern techniques involving wire spark chamber and scintillation counters, in the energy range 3 - 6 GeV/c. The same reactions have been studied with similar techniques by Foley et al.[6] in the energy range 8 - 15 GeV/c.

II. Introduction and Motivation for Experiment

A. Experimental

Two-body meson baryon scattering with hypercharge exchange is an interesting subject for study from several points of view.

There is the virtue on the experimental side, of having appreciable cross sections (∿100 μbarns) and of having charged particles in the final state, (or charged decays from the neutral modes). Using the complete and sometimes over-constrained kinematic information, various cuts may be performed on the data to isolate hypothesized contamination having known properties. In addition, strange baryons are produced in these reactions and many of these have weak, parity-violating decays. This allows the simultaneous measurement of the differential cross section $\frac{d\sigma}{dt}$ and the polarization P of the produced strange baryon, without the added experimental complexity of using a polarized proton target.

B. Theoretical

On the theoretical side, these reactions are interesting to study because they have a simple amplitude structure in the t-channel. This allows clear comparisons to be made between several hypercharge reactions using the charge independence of strong interaction, comparisons which in turn may be used to determine iso-spin contribution to the scattering amplitude. Finally, SU(3) symmetry may be used to relate hypercharge exchange processes, and to extract the scattering amplitudes when a sufficient number of dynamic quantities have been specified by measurement.

There is as yet no fundamental theory that can describe the broad class of existing high energy scattering data in a quantitative way.[7] Existing ideas, including absorption models, Regge poles, and geometrical models, have been used to represent

portions of the data. These ideas require many free parameters in their fits,[8] and have not yet been able to meet the twin requirements of providing an overall picture theoretically, while meeting all the experimental tests. These circumstances, and the availability of new experimental information[9-11] have resulted in new work in extracting the underlying scattering amplitudes directly from the data.[12-15]

Despite the large errors in present data, these amplitude analyses have placed sufficient constraints on the amplitudes to cause non-trivial rethinking in the case of the absorption model.[16-20] They have also provided information on how to correct some Regge pole contribution in πN scattering.[21]

This thesis describes an experiment to measure the differential cross section and polarization in the two body reactions $\pi^- p \to K^o \Lambda^o / \Sigma^o$. In addition, these measurements, complemented with assumptions of SU(3) symmetry (to be discussed later) are then used to construct the amplitudes which completely describe these reactions.[22]

In Chapter I we will give the theoretical framework in which we present the data. In Chapter II we describe the method of analyzing the events and discuss the experimental resolution. The bulk of Chapter II discusses the experimental method with descriptions of the major components of the apparatus. In Chapter III we discuss the data analysis, and give the corrections which were applied to the raw data distributions. Chapter IV describes the analysis of the polarization data. Finally, we present the results in Chapter V. The amplitude analysis,[22]

using SU(3) Clebsch-Gordan coefficients at the meson-baryon-meson vertex, is reviewed in Appendix 1.

III. Theoretical Background

A. Variables

This is a convenient point to define our variables and to outline the theoretical framework for our discussion. We restrict ourselves to two body meson baryon scattering, represented by Figure 1(a): 1+2→3+4. For spinless particles we denote the amplitude for the scattering by $T(p_1,q_1;p_2,q_2)$ where the meson four momentum changes from q_1 to q_2 and the baryon four momentum from p_1 to p_2. The sixteen arguments of T are reduced to only two independent variables by applying the requirements of Lorentz invariance, and of four-momentum conservation. We choose these to be the Mandelstam[23] variables:

$$\begin{aligned} s &= -(q_1+p_1)^2 \\ t &= -(q_2-q_1)^2 \\ u &= -(p_2-q_1)^2. \end{aligned} \qquad \text{(I-1)}$$

Only two of these are independent, since $s+t+u = m_1^2+m_2^2+m_3^2+m_4^2$. Taking the spin of the nucleon into account, we write the amplitude as:[24]

$$T(s,t,u) = \bar{u}(p_2)\{A(s,t,u)+1/2\gamma^{\mu}(q_1+q_2)_{\mu}B(s,t,u\}u(p_1). \qquad \text{(I-2)}$$

T is the amplitude computed in perturbation theory following the standard Feynman rules. The reduction to the independent functions A+B is the result of the work by Chew, Goldberger, Low, Nambu.[25] $\bar{u}$ and u are the spinors for the final and

initial state baryons, A and B the Lorentz invariant scattering amplitudes, and γ^μ the Dirac matrices. We rewrite this in terms of the spin flip and spin nonflip amplitudes $f_{\pm}f_{\pm}$, (independent of kinematic singularities):[26]

$$f_{\pm} = (4m-t)A+m(s-u)B$$
$$f_{\pm} = B. \qquad \text{(I-3)}$$

In general for spin 1/2 two body scattering there are four independent amplitudes f_{+}, f_{-}, $f_{\pm}$, $f_{\mp}$, which give the amplitude for having initial and final spin states: up-up, down-down, up-down, down-up. Using parity and time invariance conservation gives two relations among these amplitudes: $f_{+} = f_{-}$ and $f_{\pm} = -f_{\mp}$. Hence, the scattering of spin 0 and spin 1/2 particles is completely specified by knowledge of the two complex amplitudes $f_{+}f_{\pm}$, (four numbers in all) as a function of the two independent kinematic variables s and t. In the amplitude analysis we will describe,[27] the $f_{+}f_{\pm}$ are determined from the data and from SU(3) relations (see Appendix 1).

B. Crossing Symmetry and OPE

Consider two other reactions that are related to Figure 1(a) by crossing the particle lines and changing particle to anti-particle, as in Figure 1(c) and 1(d). We can denote reaction I and the related reactions as:

1+2→3+4	I	Fig. 1(b)	s-channel	
1+3→2+4	II	Fig. 1(c)	t-channel	(I-4)
3+2→1+4	III	Fig. 1(d)	u-channel	

For concreteness, let I be $\pi^- p \to \pi^- p$; the related reactions II and

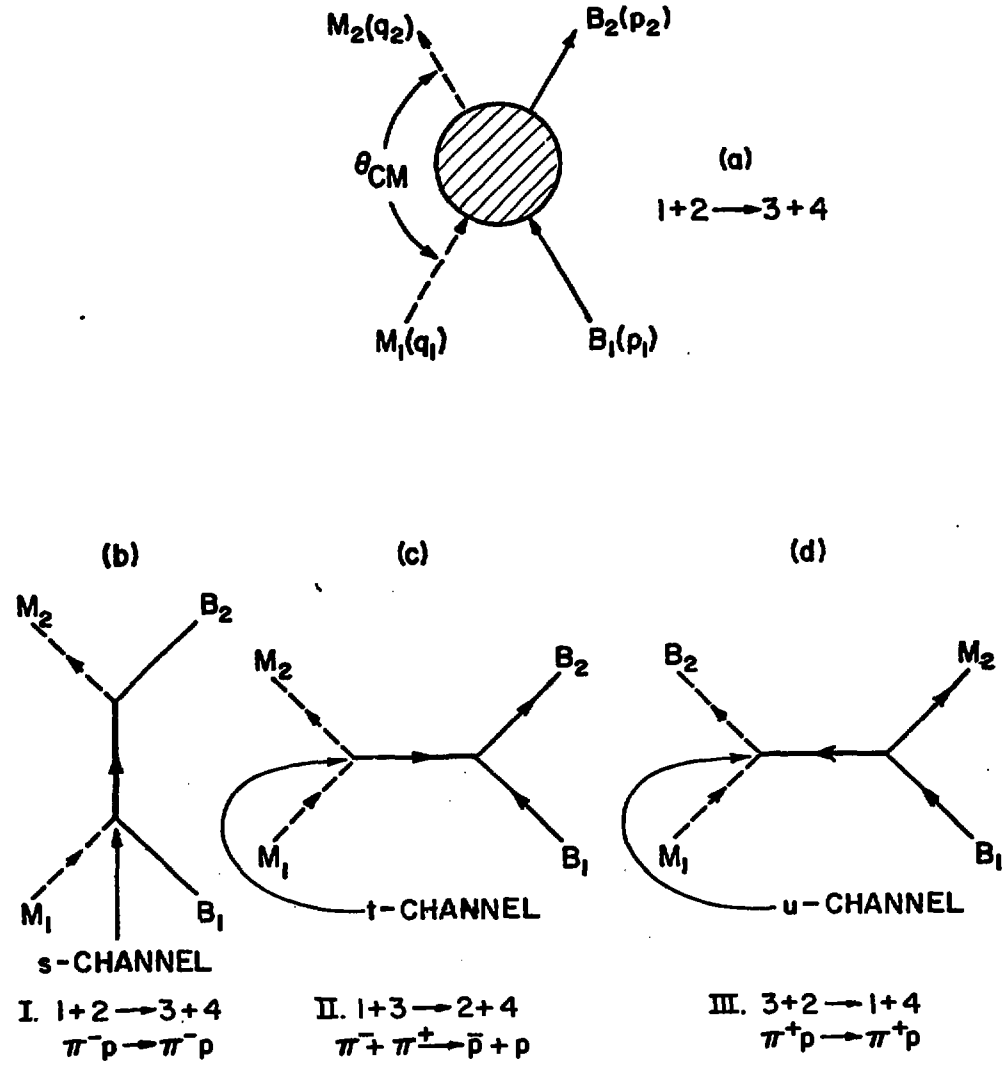

Fig. 1.--High energy scattering diagrams. (a) general diagram for two body reactions; (b) reaction as viewed in s-channel; (c) reaction as viewed in t-channel; (d) reaction as viewed in u-channel

III are then $\pi^- + \pi^+ \rightarrow \bar{p}+p$ and $\pi^+ p \rightarrow \pi^+ p$, respectively. The variables s, t, and u are related for these three channels, since changing a particle into its antiparticle changes the sign of its four vector. For channel I, the "s" channel, s is the c.m. energy squared, and t the momentum transfer squared. In channel II, the "t" channel, the variable s becomes the momentum transfer, and t the c.m. energy variable. Finally, in channel III, the "u" channel, u is the c.m. energy and t the momentum transfer variable. The idea of Crossing Symmetry is that there exists a complex amplitude T(s,t,u) that describes the scattering in all three channels. The amplitude is analytically continued in the variables s, t, and u to regions where these take on physical values corresponding to channels I, II, or III.

C. Peripheral Model

We can interpret some of the contributions to the scattering amplitude T. A branch point in T signifies that the threshold of a new particle reaction was reached. A pole on the real energy axis (in the s and u channels at fixed to) signifies the existence of a single particle intermediate state. Another idea known as the One Particle Exchange (OPE) mechanism,[28-29] proposes that there may be contributions to the amplitude in the physical s-channel, from poles due to the existence of single particle intermediate states in the t channel. At constant s the amplitude is a function of t, and as the c.m. scattering angle goes from 0° to 180°, t goes from zero to negative values. If pion exchange contributes to the amplitude, then T(s,t,u) will have a pole at $t = m_\pi^2$, which is an unphysical (positive)

value of t for the s channel process. The s channel amplitude thus has a contribution from the exchange of a particle in the t channel. Since the same function describes the scattering in all three channels, single particle intermediate states in any one channel influence the amplitude in any other channel. Modifying OPE by adding the postulate that in the physical region (in s, t, u) closest to a pole the amplitude is dominated by that pole, has the consequence that small t (small c.m. angle) scattering is most probable. This is in fact what is experimentally observed[30-31] at high energies. This version of OPE is known as the peripheral model. Small t corresponds to long range interactions taking place at the periphery of the nucleon, so to speak.

D. OPE and Regge Theory

For an s channel scattering process (neglecting spin and setting masses of the scattering particles equal) the Feynman amplitude for the t channel exchange of a single meson of spin J and mass m_J is (see Figure 1(c)):[32]

$$T(s,t) = g(-(s/s_o))^J/(m_J^2-t) \qquad \text{(I-5)}$$

in the limit as $s\to\infty$. g is the coupling constant at the vertices and s_o an energy scale factor. If we allow the exchanged particle to be a series of particle reccurances with spins, $J = 1,3,5 \ldots$ (known as a Regge trajectory), then the amplitude due to a sum of the simple exchanges of particles on this trajectory is:[33-34]

$$T(s,t) = \sum_{J=o}^{\infty} \frac{g_J^2}{m_J^2-t}\left(\frac{(-1)^J-1}{2}\right)(s/s_o)^J \qquad \text{(I-6)}$$

Assuming all the coupling constants g_J^2 to be equal, and parametrizing $m_J^2 = \mu^2$ (J-a) (strongly suggested by empirical classification of particles)[35] the sum is evaluated to be:

$$T(s,t) = \frac{-g^2}{2\mu^2} \frac{(1-e^{2\Pi\alpha(t)})}{\sin \Pi\alpha(t)} (s/s_o)^{\alpha(t)} \qquad \text{(I-7)}$$

We will discuss two body scattering in terms of the peripheral model, where amplitudes are dominated by t channel exchanges of Regge trajectories.

E. Phenomenology and Peripheral Model

This picture is supported by the following features of experimental data. There seems to be a strong correlation between the presence or absence of peripheral forward and backward peaks in scattering data, and the existence or nonexistence of particles (trajectories) which can be exchanged in the t or u channels.[36] For example:

i) in the reaction $\pi^+ p \to K^+ \Sigma^+$ [37-38]

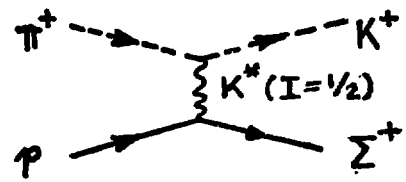

two I = 1/2 strange mesons, [$K^*(890)$ and $K^*(1420)$] are allowed to be exchanged in the t channel* and two I = 1 and I = 0 strange baryons (Σ,Λ) to be exchanged in the u channel. The data shows a pronounced forward peak and also a backward peak, consistent with the peripheral model since there

---

*allowed by spin and parity conservation.

exist particles with the allowed exchange quantum numbers in both channels.

ii) For $K^- p \to \bar{K}^0 n$, the allowed t channel exchange is of a non-strange I = 1 meson, the allowed u channel exchange is of a 1 = 1 or 0 strangeness + 1 baryon. The data[39] shows a peak at small t, corresponding to the existence of the ρ and A_2 I = 1 mesons, but there is no backward peak and significantly also no known I = 1,0 strangeness + 1 baryon.

iii) As a final example, we consider the reaction $\pi^- p \to K^+ \Sigma^-$. Here the t channel exchange must be of a doubly charged meson, while the u channel exchange must be a strange I = 1,0 baryon. Again, the data[40-41] shows no peak at small t, consistent with the fact that no doubly charged meson is known to exist, and a peak at small u, corresponding to the exchange of the Λ and Σ.

We note also that for the above examples, which involved charge and hypercharge exchange, the exchanged objects (when they are found to exist) fall into the SU(3) octet classification scheme. The I = 3/2 doubly charged meson required for the t channel exchange in $\pi^- p \to K^+ \Sigma^-$ would not fit into any SU(3) octet classification. Mesons not belonging in the SU(3) classification scheme are known as exotic mesons. This experimental circumstance, along with the success of the Barger-Cline[42] sum rule which we will discuss next, provide strong evidence for the dominance of octet exchange in the charge and hypercharge reactions.

F. SU(3) Symmetry

We continue to restrict ourselves to two body pseudoscalar meson-baryon scattering. Whether it is valid to apply SU(3) symmetry to scattering amplitudes at all is yet to be settled. Early work[43] to relate reactions through SU(3) made no attempt to deal with the inherent dynamics of the 4-particle amplitude. Some of the cross section relations, as a result, were in considerable disagreement with the experiment. The nature of the dynamics evidently accounts for deviations from exact SU(3) relations. For example, cross sections in reactions where strange mesons are exchanged show a faster decrease with energy than those in reactions where non strange mesons are exchanged. Barger and Olssen[44] addressed themselves to the problem of finding a context in which SU(3) could be successfully applied, to relate scattering at high energy. They suggested that one way to avoid symmetry breaking due to dynamic effects was to use SU(3) to compare amplitudes only among reactions which had similar exchanges. They apply SU(3) symmetry within the dynamical framework of the peripheral model outlined above, treating reactions where the amplitude is dominated by peripheral exchanges, and explicitly accounting for symmetry breaking effects such as non degenerate masses and direct channel resonances.

G. Applications of SU(3)

1. Barger-Cline sum rule

SU(3) symmetry is applied to the three particle vertices in exchange diagrams like Figure 1(c). An example of this is

provided by the charge exchange reactions. We have:

$$\begin{aligned} &\pi^- p \to \pi^0 n && \rho \text{ - exchange} \\ &\pi^- p \to \eta n && A_2 \text{ - exchange} \\ &K^- p \to \bar{K}^0 n && \rho, A_2 \text{ - exchange} \\ &K^+ n \to K^0 p && \rho, A_2 \text{ - exchange.} \end{aligned} \tag{I-8}$$

From the allowed t channel exchanges, the following couplings occur at the meson vertex:

$$\rho^+\pi^-\pi^0,\ K^-K^0\rho^+,\ K^-K^0\rho^-,\ \pi^-\rho A_2,\ K^-K^0A_2^+. \tag{I-9}$$

SU(3) can be used to find the relative strengths of these couplings, and from this the four reactions can then be related. The SU(3) invariant couplings[45] for vector meson exchange are obtained by taking the trace of (MMV), and for tensor exchange by taking the trace of (MMT), where M,V, T are the SU(3) invariant matrices for the pseudoscalar, vector and tensor mesons, respectively (see Ref. 45.). The amplitudes for vector and tensor exchanges are independent and have definite G parity. The former is labeled the F amplitude (G=1), and the latter the D amplitude (G=-1). The SU(3) Clebsch-Gordan coefficients and the two amplitudes F and D then give the meson couplings:

$$\begin{aligned} C = g_F\{&\sqrt{2}\pi^-\pi^0\rho + K^-K^0\rho - K^+\bar{K}^0\rho\} \\ &+ g_D\{K^-K^0A_2 + \sqrt{2/3}\pi^-\eta A_2^+ - K^+\bar{K}^0A_2^-\} \end{aligned} \tag{I-10}$$

The charge exchange amplitudes are obtained from this:

$$\begin{aligned} \langle \pi^- p | \pi^0 n \rangle &= -\sqrt{2}F \\ \langle K^- p | \bar{K}^0 n \rangle &= F + D \\ \langle K^+ n | K^0 p \rangle &= -F + D \\ \langle \pi^- p | \pi^0 n \rangle &= \sqrt{2/3}D \end{aligned} \tag{I-11}$$

The coupling at the baryon-meson-baryon vertex is fixed for these exchanges and so need not be considered for purposes of relating the reactions. Thus, there are four processes given in terms of two amplitudes, so that two sum rules can be obtained. These are the Barger Cline[46] sum rules,

$$\begin{aligned} \frac{d\sigma}{dt}: \quad & (K^-p\to\bar{K}^0n)+(K^+n\to K^0p) = (\pi^-p\to\pi^0n)-3(\pi\bar{p}\to\eta n) \\ \sigma_{tot}: \quad & \langle K^-p|\bar{K}^0n\rangle-\langle K^+n|K^0p\rangle = -\sqrt{2}\langle\pi^-p|\pi^0n\rangle \\ & (K^-p-K^-n)-(K^-p-K^+n) = (\pi^-p)-(\pi^+p) \end{aligned} \qquad \text{(I-12)}$$

which are well verified by the data (Figure 2). This illustrates a successful application of SU(3) symmetry applied in a dynamical framework which will also be used to analyze our data. We note here that SU(3) invariance places no restriction on the s or t dependence of the F and D amplitudes. The data used to test the sum rule above is all at small t, and we will also be applying SU(3) to data at small t.

2. Dual Absorptive Model

The work of Loos and Mathews[47] provides additional confirmation for SU(3) predictions of coupling constants at three particle vertices. Using the Dual Absorptive Model (DAM) of Harari,[48-49] these amplitudes are parametrized by forms like:

$$\begin{aligned} &\mathrm{Im}f_{\ddagger}(s,t)\sim g(s/s_o)^{\alpha(t)}e^{At}J_o(r\sqrt{-t}) \\ &\mathrm{Re}f_{\ddagger}(s,t)\sim g(s/s_o)^{\alpha(t)}e^{At}\{1+at+bt^2+ct^3\}e^{Bt}\tan\tfrac{1}{2}\alpha(o) \end{aligned} \qquad \text{(I-13)}$$

and similar expressions (with J_1 instead of J_o) for the spin flip amplitudes. They fit the experimental data with these forms, allowing the coupling constants g, the exponential slope parameters A and B, the polynomial coefficients a, b, c, and the

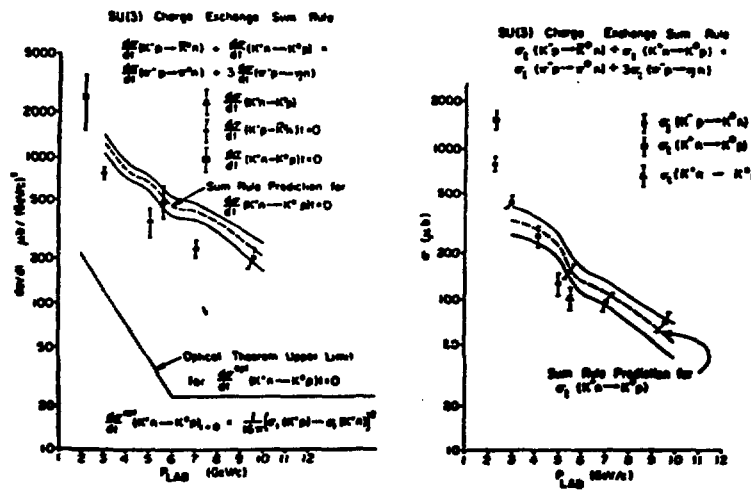

Fig. 2.

Fig. 2.--Experimental tests of the Barger-Cline Sum Rule; differential and total cross sections, from Reference 26

interaction radius r to be parameters determined by the data. $\alpha(t)$ is the Regge trajectory, taken to be the ρ and A_2 trajectory for vector and tensor exchange, respectively, and s_o is the energy scale factor, taken to be 1 GeV^2. With the parameters determined, the result is an amplitude analysis on the basis of DAM. Loos and Mathews compare their amplitudes with the model independent amplitudes of Halzen and Michaels[50] and obtain good agreement. There is excellent agreement, moreover, between the coupling constants from the DAM fit and the coupling constants from SU(3) symmetry at the three particle vertices. We take this as additional indication for the validity of applying SU(3) symmetry at three particle vertices, in the context of the peripheral model.

H. Input for Amplitude Analysis

Until now we have been preparing the groundwork for the amplitude analysis for our data carried out by Rust and Ward.[51] We have defined the kinematic variables, written down the general amplitude for two body pseudoscalar meson-baryon scattering, used crossing symmetry to outline the features of the peripheral model, and shown a successful application of SU(3) in relating the charge exchange reactions. We are now ready to state the assumptions to be used in the amplitude analysis.

The amplitudes for the two reactions:

$$\pi^- p \to K^o \Lambda^o$$

$$\pi^- p \to K^o \Sigma^o \text{ at 5 GeV/c incident beam momentum}$$

are found by using the measurements of $d\sigma/dt$ and polarization, and the SU(3) Clebsch-Gordan coefficients at the baryon-meson-baryon

vertex. In general there are four numbers needed to specify each reaction completely. There are actually only three quantities that can be determined in each reaction - the magnitude of the spin flip and spin non flip amplitudes and the phase angle between them. Thus, for the two above reactions six quantities are to be determined. For $\pi^- p \to K^o \Lambda^o$, we have measured the differential cross section and polarization as a function of t, giving two quantities, and for $\pi^- p \to K^o \Sigma^o$, we have measured the differential cross section and we take the polarization from the P measurement in $\pi^+ p \to K^+ \Sigma^+$.*

This gives four of the six quantities needed to completely specify the two reactions. The SU(3) Clebsch-Gordan coefficients provide the additional two constraints.

Rust and Ward[51] carry this procedure out. We outline their method and present the amplitudes and further discussion in Chapter V and Appendix 1.

---

*See Chapter V.

CHAPTER II

RESOLUTION AND EXPERIMENTAL METHOD

I. General Description

In $\pi^- p$ interactions $\sigma_{tot} \sim 40$ mb, while $\sigma_{tot} \sim 150$ μb for the particular final states we studied. Accordingly, we had to discriminate by one part in $\sim 10^4$ or better against all processes other than the ones in which we were interested. In addition, the Λ^o and Σ^o masses are separated by ~77 MeV, and in our initial planning we had to take particular care to maintain high kinematic resolution in order to cleanly separate these two interesting reactions. Wire spark chambers are well suited to providing high resolution since they are of low mass (small amount of multiple scattering) and have high spatial resolution ($\sigma \sim 0.25$ mm). Figure 3 shows the plan view of the apparatus.

Events of interest had the beam pion (entering from the left in Figure 3) interacting in a liquid hydrogen target. K^o_s's thus produced then decayed to $\pi^+\pi^-$ at a point downstream of the veto counters. (All other pion interactions leading to a final state with charged particles were vetoed.) Both decay pions then passed through the magnet gap and through the counter hodoscope and the spark chambers at the rear of the magnet. The result was that we knew the identity and momentum of the incident particle and the

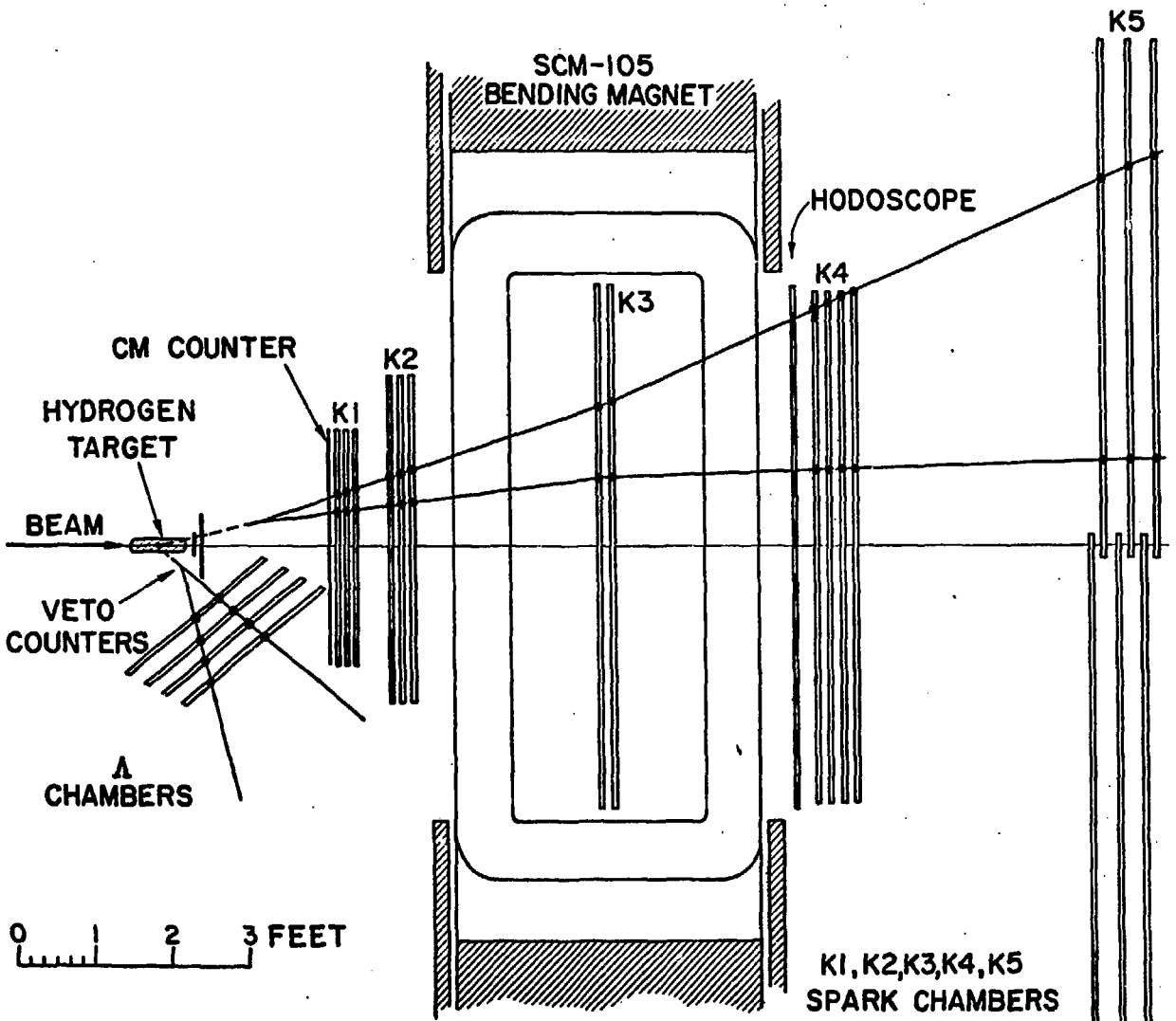

Fig. 3.

Fig. 3.--Experimental layout

momenta of the two (or more) particles passing through the spectrometer.

II. Event Identification and Analysis

Conservation of energy and momentum at the production and decay vertices gives:

$$p_\pi + p_p = p_{K^o} + p_{recoil}$$

(p = 4 momentum) (II-1)

$$p_{K^o} = p_\pi + p_\pi$$

These relations, and the hypothesis that the spectrometer particles were pions, provided more than enough information to completely specify the kinematics of the reactions we studied. K^o's were identified by calculating the invariant mass of the $\pi^+\pi^-$ pair in the spectrometer, and requiring that this agree with the known value of K^o mass to within the experimental uncertainty.

$$M^2_{K^o} = (p_\pi + p_\pi)^2 = 2m^2_\pi + 2(E_\pi E_\pi - \vec{p}_\pi \cdot \vec{p}_\pi) \qquad \text{(II-2)}$$

Figure 4 shows the $\pi^+\pi^-$ invariant mass distributions for incident pion momenta of 3, 4, 5, and 6 GeV/c. The true K^o mass value is then used as a constraint in a fit to adjust the measured $\pi^+\pi^-$ momenta. Finally, the recoiling baryon is identified by calculating the missing mass:

$$MM^2 = E^2_{recoil} - p^2_{recoil} = (E_\pi + m_p - E_{K^o})^2 - (\vec{p}_\pi - \vec{p}_{K^o})^2 \qquad \text{(II-3)}$$

Figure 5 shows this distribution for our data. The two peaks correspond to events where the recoil baryon is a Λ^o or Σ^o particle. The precision with which we can make unambiguous separation of events, using the identification procedure above,

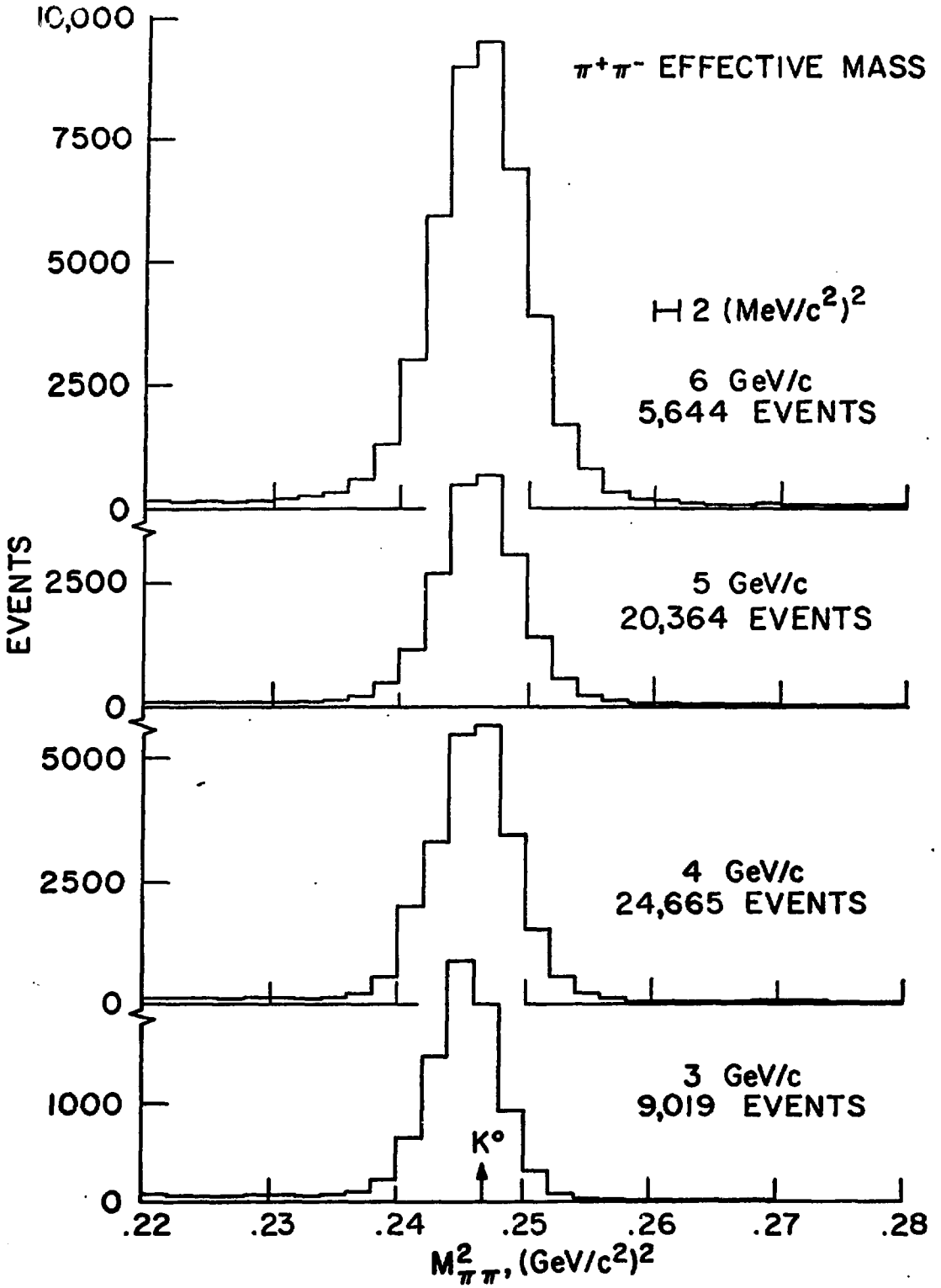

Fig. 4.

Fig. 4.--Effective mass distributions for $\pi^+\pi^-$

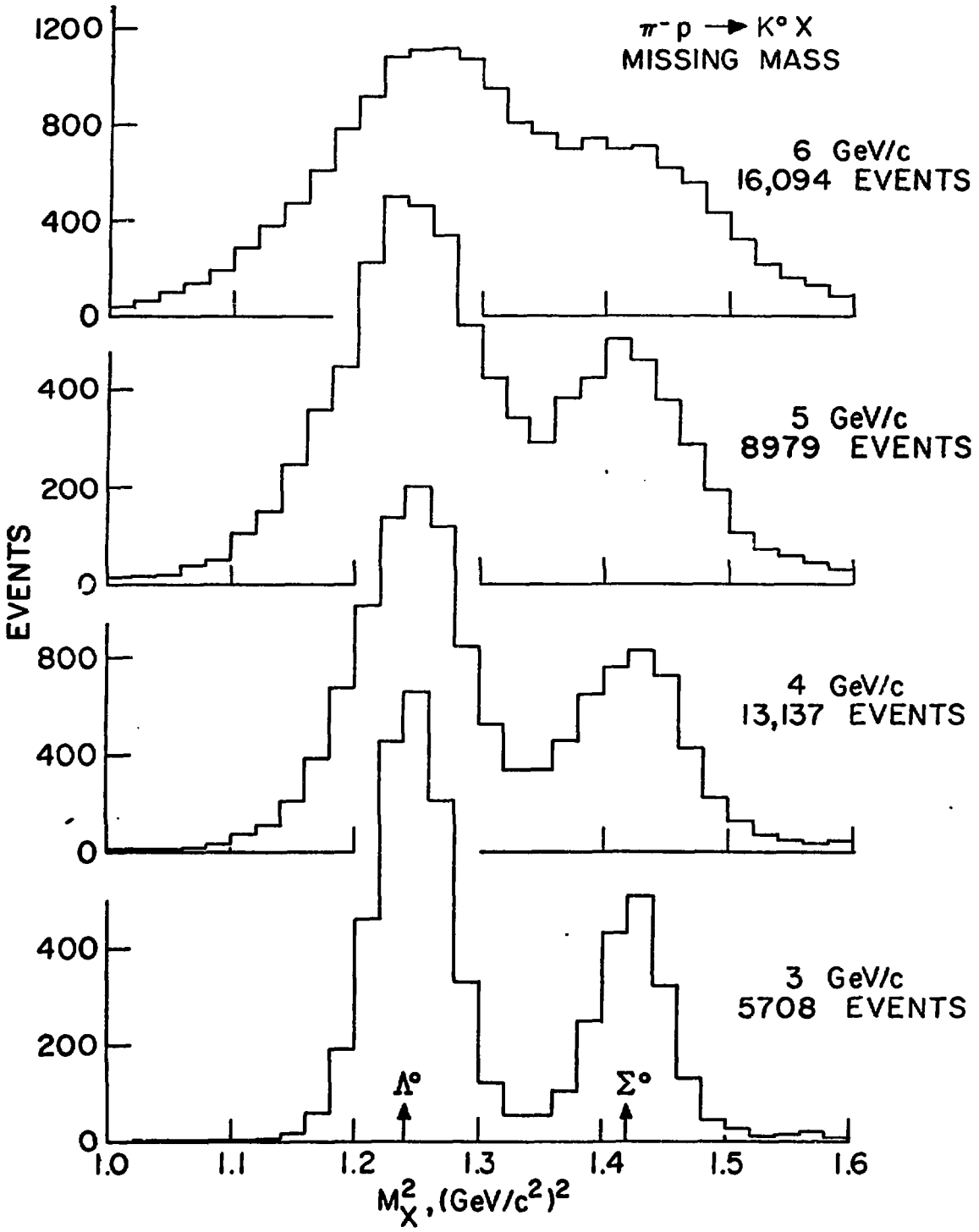

Fig. 5.

Fig. 5.--Missing mass distributions

is specified by the experimental resolution with which we can measure kinematic quantities. We discuss this next.

III. Resolution

Separation of K^oA^o from $K^o\Sigma^o$ events had to be done solely on the basis of kinematics, since both final states satisfied the trigger requirement of the apparatus. Using the measured momentum of the beam and the reconstructed momentum of the K^o, the missing mass of the recoiling strange baryon was calculated using Equation II-3. With infinite experimental precision the missing mass distribution would show peaks of zero width at the A^o and Σ^o masses. However, effects such as multiple Coulomb scattering in the spark chambers, energy loss, delta rays, limited positional accuracy due to having a given number of wires per inch in the spark chambers, spark formation jitter, and effects due to electronic digitization of coordinates, all introduced errors in the measured quantities of an event. The errors are distributed approximately in a Gaussian about "true" values of the measured quantities, and this accounts for the widths in the peaks in Figure 5.

Assuming gaussian distributed errors, we can calcualte the missing mass resolution in terms of the momentum and angle resolution on the beam and spectrometer particles, since

$$\Delta MM^2 = f\left(\frac{\Delta p_\pi}{p_\pi}, \frac{\Delta p_{K^o}}{p_{K^o}}, \Delta\theta_{\pi K^o}\right) \qquad \text{(II-4)}$$

For present purposes we neglect any correlations between errors in the angle measurement θ and the momentum measurements p_π and p_{K^o}.

Thus:

$$\Delta MM^2 = \left(\frac{\partial MM^2}{\partial p_{K^o}}\right)^2 \Delta p_{K^o}^2 + \left(\frac{\partial MM^2}{\partial p_\pi}\right)^2 \Delta p_\pi^2 + \left(\frac{\partial MM^2}{\partial \theta}\right)^2 \Delta\theta_{\pi K^o}^2$$

$$\frac{\partial MM^2}{\partial p_\pi} = -2\{\beta_\pi (E_{K^o} - m_p) - p_{K^o}\cos\theta\} \qquad \text{(II-5)}$$

$$\frac{\partial MM^2}{\partial p_{K^o}} = -2\{\beta_{K^o} (E_\pi + m_p) - p_\pi \cos\theta\}$$

$$\frac{\partial MM^2}{\partial \theta} = 2 p_\pi p_{K^o}$$

If we approximate $\beta_\pi = \beta_{K^o} = Mp \tilde{\sim} 1$, pick typical values for p_π, p_{K^o}, θ, and use the known values $\frac{\Delta p_\pi}{p_\pi} \sim .2\%$, $\frac{\Delta p_{K^o}}{p_{K^o}} \sim .6\%$, $\Delta\theta \sim 2$ mr, we obtain the following calculated missing mass resolutions:

$$\Delta MM^2 = 12 \text{ MeV at } 3 \text{ GeV/c}$$

$$\Delta MM^2 = 37 \text{ MeV at } 6 \text{ GeV/c}$$

This agrees very well with the experimentally determined widths from Figure 5 of 13.5, 19, 25.5, 34 MeV, at 3 - 6 GeV/c. The missing mass resolution is dominated by the error in the K^o momentum determination, which worsens as a function of incident beam momentum. At higher beam momenta, the K^o momentum resolution worsens since the bend angle of tracks through the field decreases (from $\theta = \frac{\int B dl}{p}$).

We can calculate the effective mass resolution in a similar fashion to the above. The predicted rms values also compare well with measured values. Since such a calculation gives accurate results for the missing mass and effective mass resolutions, we also use it to predict the t resolution, where we have no independent measure of the resolution.

$$\Delta t^2 = \left(\frac{\partial t}{\partial p_\pi}\right)^2 \Delta p_\pi^2 + \left(\frac{\partial t}{\partial p_{K^o}}\right)^2 \Delta p_{K^o}^2 + \left(\frac{\partial t}{\partial \theta}\right)^2 \Delta\theta^2$$

$$\frac{\partial t}{\partial p_\pi} = -2\beta_\pi E_{K^o} + 2p_{K^o}\cos\theta \qquad \text{(II-6)}$$

$$\frac{\partial t}{\partial p_{K^o}} = -2\beta_{K^o} E, + 2p_\pi \cos\theta$$

$$\frac{\partial t}{\partial \cos\theta} = 2p_\pi p_{K^o}$$

Making the same approximations as before, and using the same values for $\frac{\Delta p_\pi}{p_\pi}$, $\frac{\Delta p_{K^o}}{p_{K^o}}$, $\Delta\theta$, as a function of beam momentum as before, we obtain the t resolution of $\pm.005$ $(\text{GeV/c})^2$ for $|t|<0.5$ $(\text{GeV/c})^2$.

We do the final separation of Λ^o from Σ^o events by the more precise method of fitting two gaussians to the missing mass distributions. The free parameters in the fit are:

1) the widths of the two gaussians

2) the height of the two gaussians

The mass difference between Λ^o and Σ^o was not allowed to vary. Figure 6 shows a typical fit to the data. The χ^2 per degree of freedom is large in the fit, and we believe this is because of non-gaussian contributions to the resolution, such as scattering in the chambers. Cuts are then applied to the data distributions. This implies that a correction is needed to account for events which are lost in the wings of the gaussian due to the cut. In addition, using these fits we obtain corrections due to the cross contamination of the Λ^o and Σ^o missing mass peaks. Table 2 shows these corrections as a function of beam momentum.

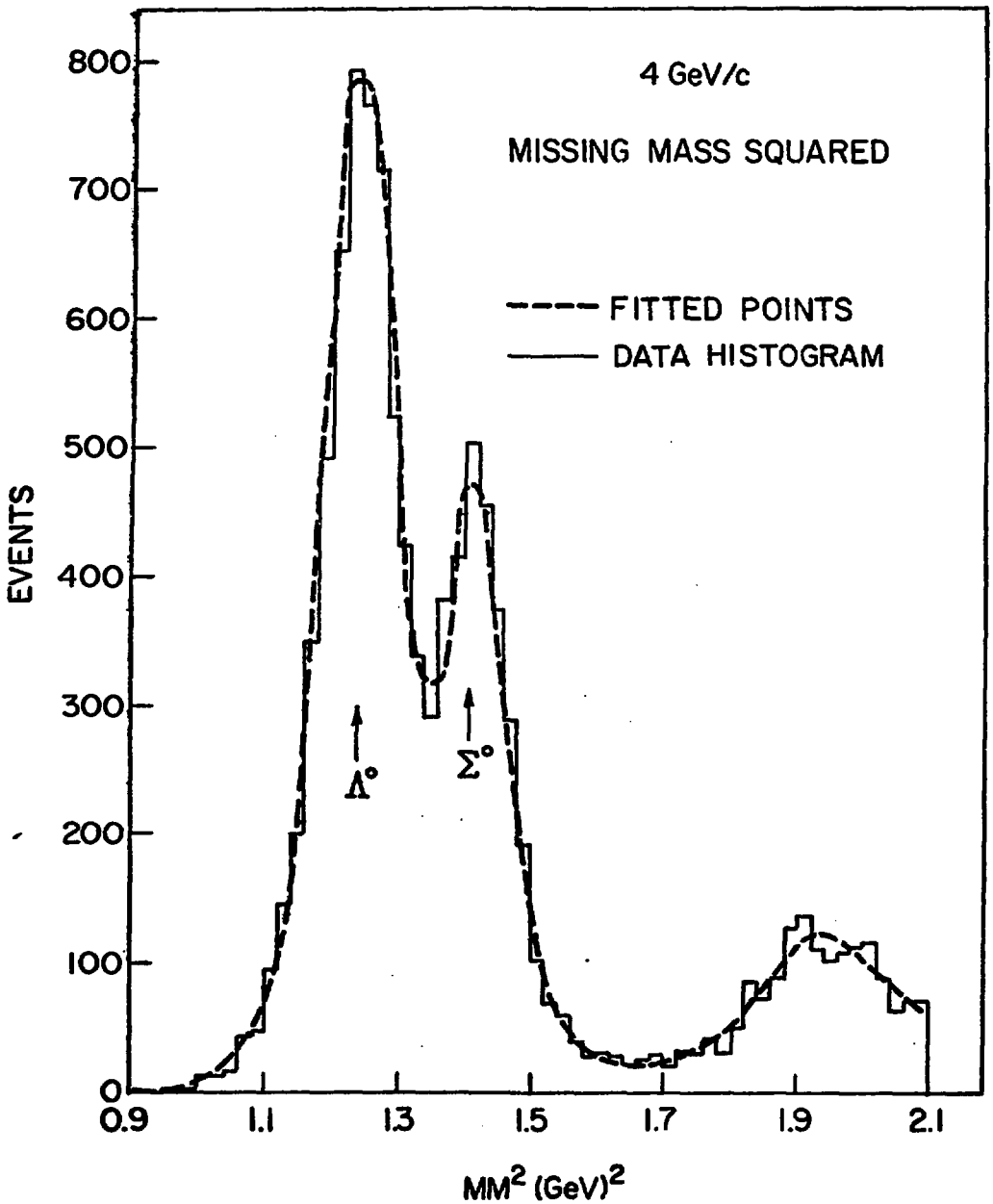

Fig. 6.

Fig. 6.--Fit to the missing mass distribution

TABLE 2

CORRECTION FOR EVENTS LOST IN GAUSSIAN WINGS[a]

Energy	a	b	c	d
3	.9979	.0051	.0002	.9669
4	.9800	.0367	.0052	.8976
5	.9538	.0869	.0166	.8268
6	.8797	.1515	.0694	.7405

[a]Let Λ^o and Σ^o denote the corrected number of Λ^o and Σ^o events, respectively. Let Λ' and Σ' denote the uncorrected number of Λ^o and Σ^o events within the respective missing mass cuts. Then the correction for cross contamination of the Λ^o and Σ^o peaks and for losses in the gaussian wings is given by:

$$\Lambda' = a\Lambda^o + b\Sigma^o$$

$$\Sigma' = c\Lambda^o + d\Sigma^o.$$

The corrections were applied separately at each $t' = t - t_{min}$.

IV. Experimental Apparatus

The remainder of this chapter is devoted to describing the experimental apparatus. The beam spectrometer is described in Section A. The fast electronics, which preselects events likely to be associated production events, is described in Section B. Spark chambers, the primary detectors in the spectrometer, are discussed in Section C. Sectin D gives a description of the data handling and transfer. The on-line computer operation is described in Section E, and the analysis programs in Section F.

A. Beam Spectrometer

The incident beam to the spectrometer, (Figure 7) comprised of π's, K's and $\bar{p}$'s, was produced by the interactions of the 12 GeV/c primary proton beam from the ZGS, with a seven interaction length copper target. The momentum was analyzed by a two stage beam spectrometer consisting of collimators, bending and quadrupole magnets, and counters. Particle separations were done by four threshold gas Cerenkov counters. A six counter hodoscope of 1/2" wide, 1/8" thick scintillators defined eleven momentum regions. At each chosen beam energy, particles having an $\sim$3% spread in momentum were selected by two bending magnets and then focussed by two quadrupole magnets onto the momentum hodoscope. The magnets transformed the momentum spread of the particles into a spread in their displacement in a horizontal plane about the beam center. Hence particles of, for example, 3 GeV/c $\pm$.0075 were focussed to be within a width $\pm$.08" about the beam center,

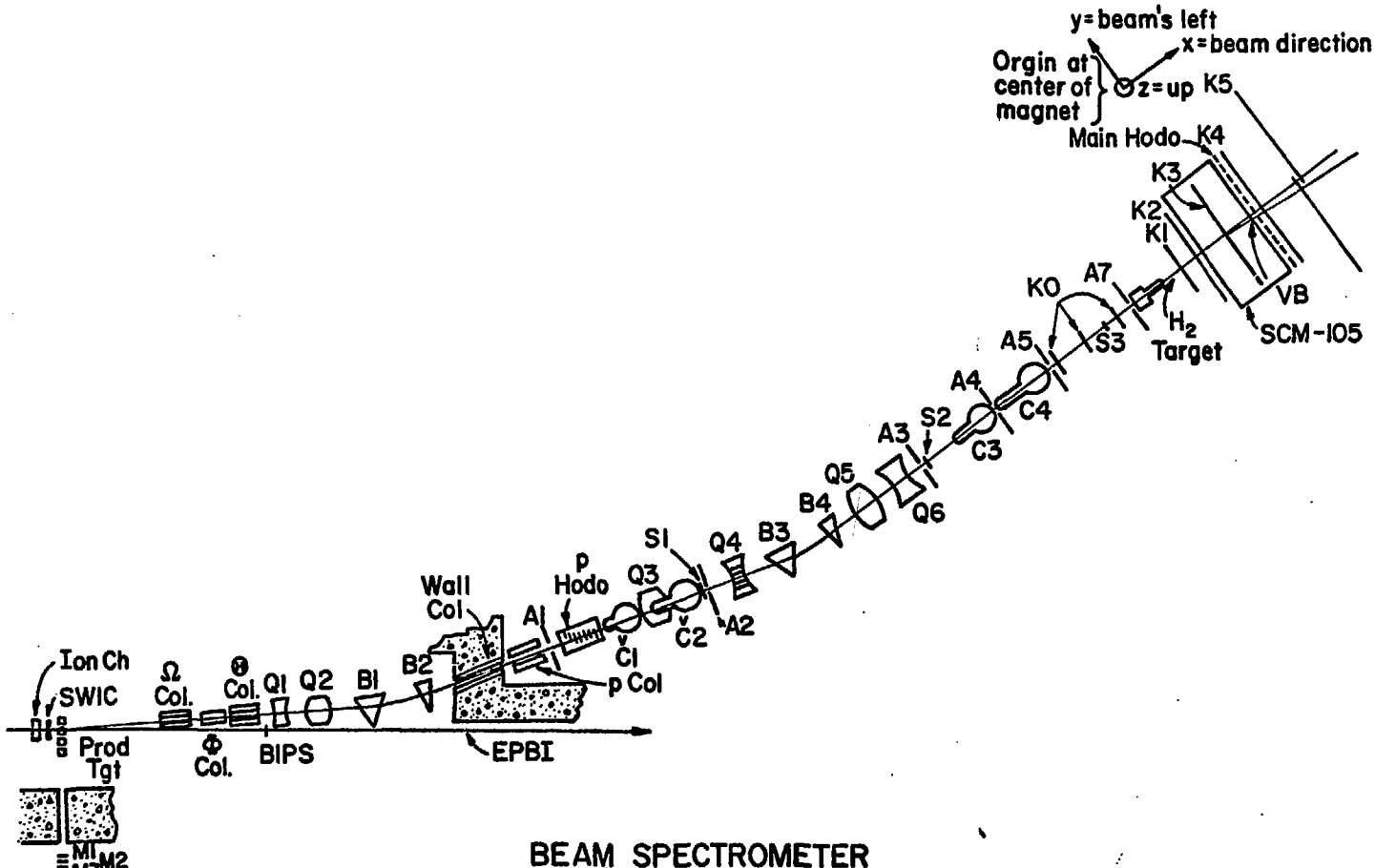

BEAM SPECTROMETER

Fig. 7.

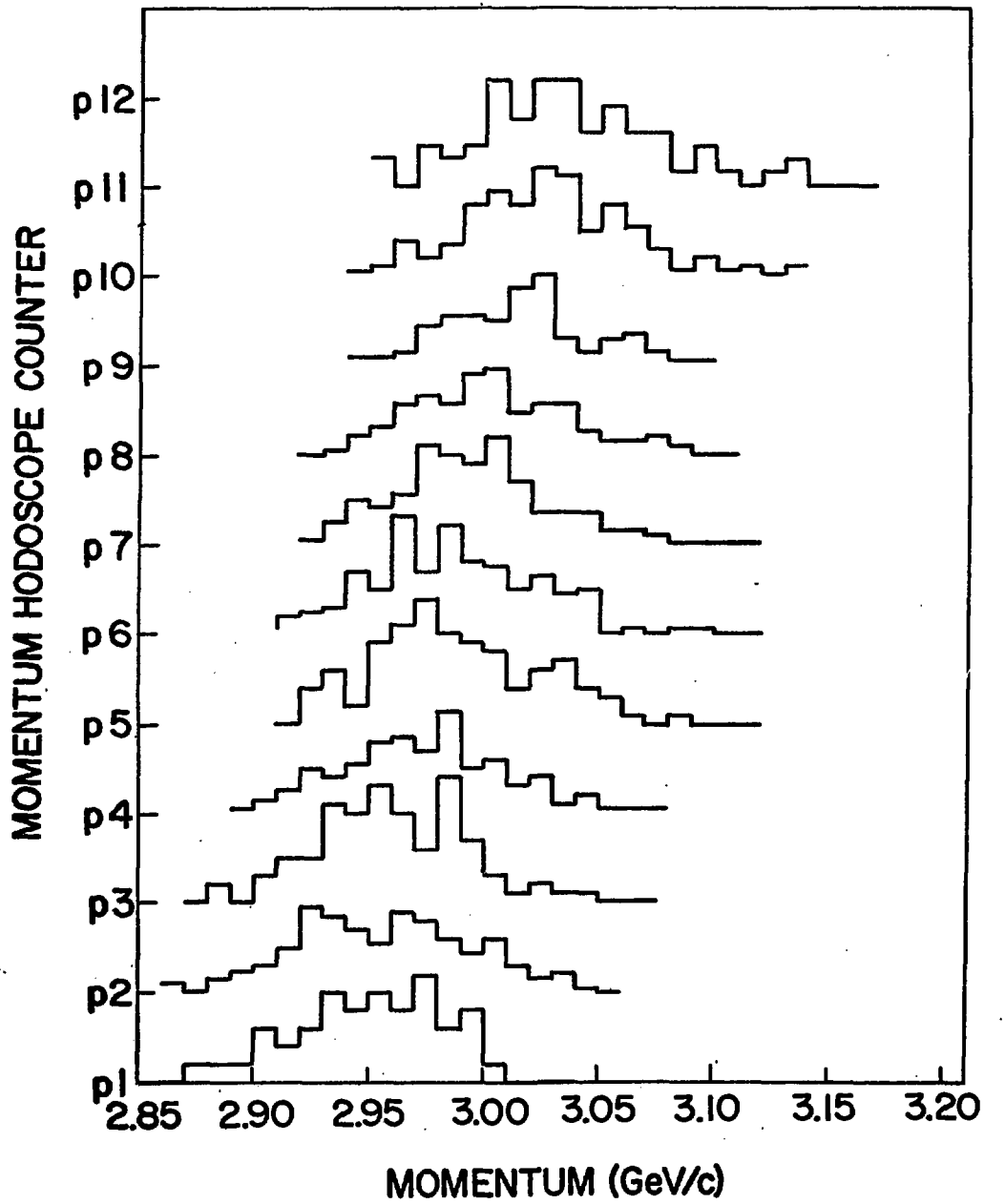

Fig. 8.

Fig. 8.--Momentum hodsocope distributions

where they were counted in the central momentum hodoscope region. Each such region specified a 0.25% interval in momentum. The second stage of the beam spectrometer consisted of more bending magnets and quadrupoles to refocus and steer the beam achromatically to the center of a hydrogen target. We obtained a spot size at the hydrogen target of about 1.6 cm diameter or less. The dispersion at the first focus was 0.076 cm per $\Delta p/p = 0.1\%$ and Figure 8 shows the beam resolution measured in the apparatus at 3 GeV/c. The momenta of the beam particles in each of the eleven hodoscope regions was analyzed using the effective mass spectrometer for this plot. The widths in the eleven peaks in Figure 9 hence have contributions due not only to the beam momentum resolution, but also the spectrometer momentum resolution. Using this data, we estimated the beam momentum resolution to be 0.243%, which compared very well with the design and expected value.

B. Electronics and Logic

The beam was defined by counts in scintillators $S_1S_2S_3$ (Figure 7), a count in at least one of the momentum hodoscope elements, and no count in any of the halo counters A_1 through A_7. The following pattern was taken to be the signature for an "interesting" event: A beam particle disappeared into the hydrogen target, charged tracks materialized downstream of the veto counters, and two charged tracks emerged from the rear of the magnet. The probability of producing a neutral final state at these energies (3 - 6 GeV/c) with pions is $\sim$3%, however, the added geometric requirements strongly selected the particular

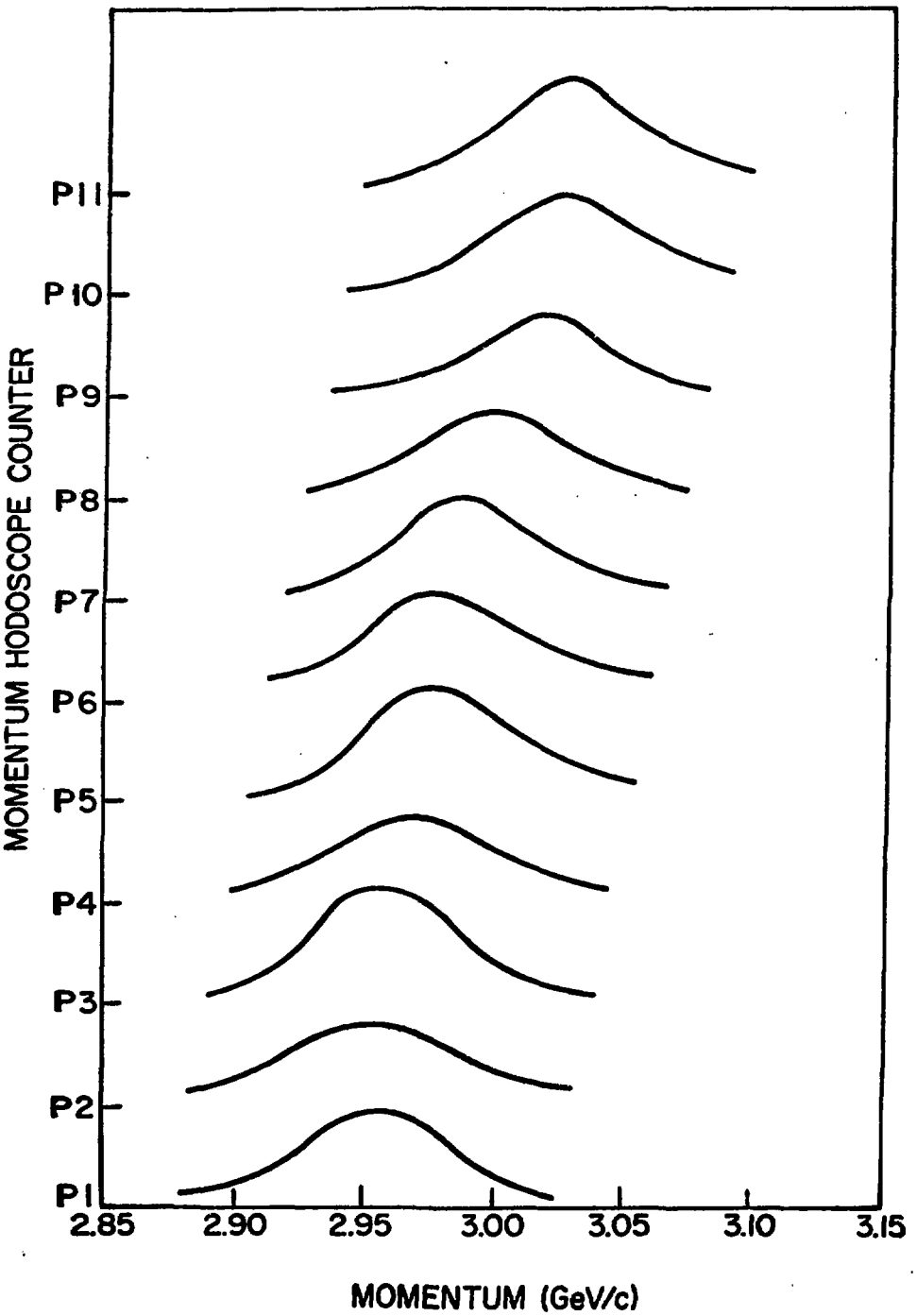

Fig. 9.

Fig. 9.--Hand drawn curves through momentum hodoscope distributions

neutral states which would cause a trigger, thus reducing the probability to 5×10^{-5}. We ended with a signal-to-noise ratio (in the triggers) of $\sim .1$, with the signal easily separable from the noise by analysis. The geometric reconstruction rejected most of the uninteresting triggers, and the kinematic requirements were used to eliminate other background.

The suppression of charged particle final states was achieved by using a three counter paddle, covering a 5" x 10" area 2" downstream of the hydrogen target. These counters were labelled VR, VL and VC (see Figure 3). The veto suppression achieved was 5×10^{-5}. We also had to guard against the possibility of triggering on events where the tracks originated at any point between the upstream end of the K-1 chambers and the trigger hodoscope. Such events lacked sufficient track information to be analyzed (for example, no momentum analysis was possible on a track originating at the magnet center). To suppress such triggers, we had a 36" x 15" x 1/8" counter (CM) in positive coincidence, so that a charged particle was required to materialize in the $\sim$21" drift space from 2" downstream of the target to just upstream of the first spark chamber set. This requirement also reduced other unwanted triggers by effectively eliminating ~ 0.65 gm/cm^2 mass of chambers and counters which might otherwise serve as a complex target for neutrons, or would facilitate gamma ray conversion. Finally, the two track trigger selection was done by a 40 counter hodoscope, covering the entire rear aperture of the magnet. Each counter was 4" wide by 13" high.

G. Spark Chambers

The major constituents of a wire spark chamber built at Argonne are best shown in an expanded diagram (Figure 10). The chamber frames, made of a fiberglass-epoxy bond (G-10 for short), were stressed so as to support a plane of wires which had been stretched to flatness having variations smaller than 1 mm. The wires (or rather ribbons) were of aluminum .001" thick and .015" wide, and in order to fasten on to a plane for stretching without breaking these rather delicate wires, we used the trick of bonding them to a .003" thick sheet of mylar; the force was then exerted on the mylar sheet. The planes had to be kept wrinkle free so that no wires would see large field gradients which might have caused breakdowns to occur. On the side of the mylar opposite to the wires was bonded a .0005" thick sheet of aluminum in order to distribute the high voltage pulse uniformly over the entire chamber area, and also so that the rise time of the high voltage at the chambers would be less than 50 nsec. It was observed that when the high voltage pulse was delivered to the wires directly, inductance in the wires slowed the propagation of the pulse across the chamber by about a factor of ten (as compared to propagation time across a conducting sheet). This produced the undesirable result of making the chamber more efficient at the voltage feed end during the (long) rise time. Using the aluminum backing sheet, the high voltage is coupled capacitively to the wires, with charge draining from the backing sheet to the wires via a bus bar. In addition, the chambers were terminated in an empirically determined

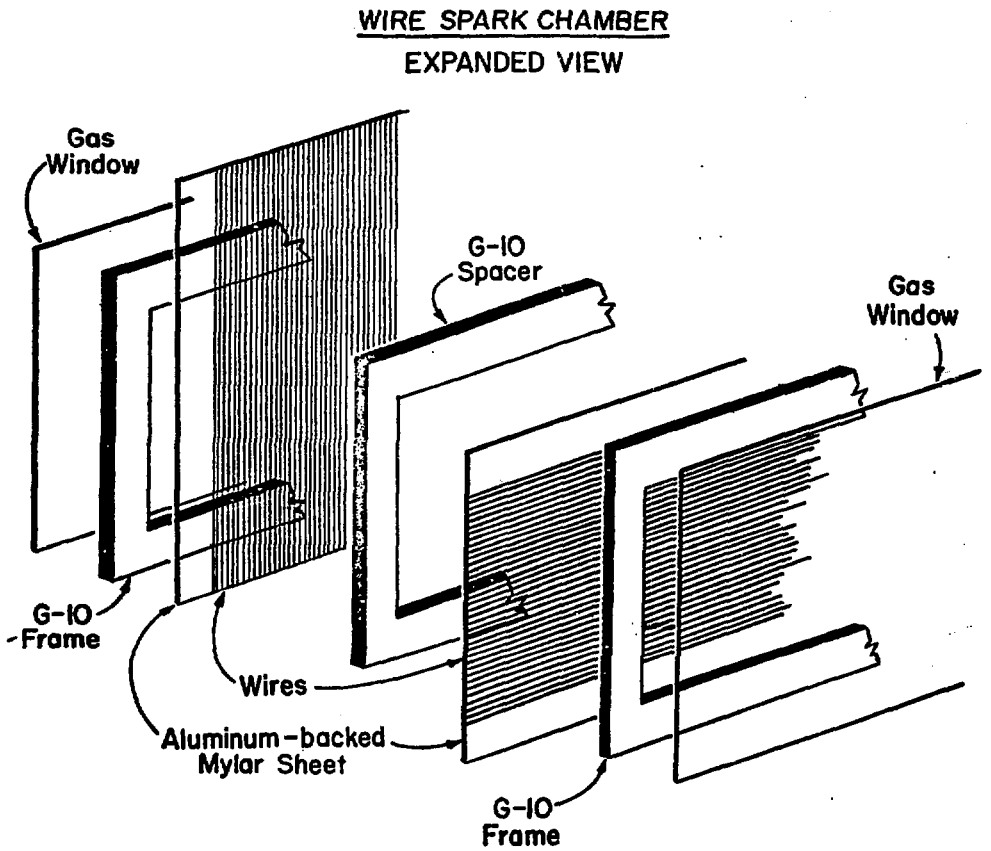

Fig. 10.

Fig. 10.--Wire spark chamber, expanded view

impedance, chosen to maximize the multiple track efficiency.

A Neon-helium gas mixture, with alcohol added at -5°C vapor pressure, was circulated through the chambers. Neon has a metastable level of 16.53 eV, and Helium an ionization energy of 15.76 eV. The primary charged particle causes some ionization directly, but also excites Ne to its metastable level. In collisions of these two atoms the excited Ne has a large cross section (order $10^{-16} cm^2$) for transferring its excitation energy to the He atom and ionizing it. (Penning effect.) A strong multiplication of charge takes place, leading to a high probability of avalanche formation. Impurities introduced as a result of leaks, outgassing, etc. were eliminated by means of a liquid Nitrogen cold trap, through which the chamber gas was passed.

1. Magnetostrictive readout

Ribbons of remendur* lay over the wires of each plane. The remendur (when magnetized) had the property that when a small region was perturbed at a point (by the fields due to a current pulse in a nearby wire) there was an acoustic propagation of the disturbance along the length of the ribbon. That is, there was a coupling (via the flipping of magnetic domains) of the magnetic and the mechanical properties of the remendur; the effect was the same as if the ribbon were plucked--a sound wave propagated

---

*Remendur is an alloy consisting of 49% iron, 49% cobalt, 2% vanadium.

away from the plucked point. Simultaneous* with the application of high voltage to the chambers, current was fed to two fiducial wires, and if sparks had occurred, the magnetostrictive line, figuratively speaking, was "plucked" at the start and stop fiducials, and at all locations between where sparks had occurred. This pulse train, the analogue representation of the spark coordinates, was transformed into a voltage pulse train by means of a pick up coil. The pulses were amplified and finally their time distributions were digitized as spark locations.

This readout technique required that the magnetostrictive ribbon have a definite magnetization along its entire length, serving as the propagation medium for pulses which represent the spark locations. The remendur was permanently magnetized according to some fixed convention, (e.g., north pole always toward peramplifier end). It was essential to shield the remendur ribbons from stray external magnetic fields since an appreciable field along the wire would constrain the magnetiziation of the ribbon, thereby attenuating the pulse amplitudes. Heavy iron shielding was therefore provided for all chamber readouts which were close to the fringe field of the analyzing magnet.

A special technique of chamber construction was used to solve this problem for the chamber set which was placed at the center of the magnet. This chamber, which had only vertical wires,

---

*In practice there was actually a difference of ∿500 nsec between the time current started to flow in the fiducials and in the wires struck by sparks. This systematic shift (amounting to ∿.10" equivalent in space) was determined by comparing the spark positions obtained from measurements of straight line tracks through the chambers with those expected from surveying the positions of the chambers.

was made to work by continuing the vertical wires on their mylar backing sheets out in a long apron to the bottom of the magnet gap, and then placing the readout line across the wires in a region where the field was weak.

D. Data Transmission

The quantities necessary to describe an event sufficiently, were the momenta and identities of the particles participating in the reaction. Energy momentum conservation permitted us to omit this measurement for some of the particles without losing the specification of the state. This is fortunate from the experimental point of view since it allows some choice in what is to be measured given a particular experimental technique or given existing technological limitations.

In our experiment the raw data consisted of the following:

- The coordinates of tracks at each spark chamber plane.
  For a normal $K_s^o \to \pi^+\pi^-$ decay in the spectrometers there were 160 coordinates in all.
- The fast logic configuration of the event.
  This included information on which scintillation counters and Cerenkov counters fired, and also what higher level logic conditions were satisfied. For example, when several alternative conditions could have triggered the spectrometer, the trigger type that did actually occur for a given event was identified in the fast logic and had to be recorded. Other examples of this kind of information are:

the identity of the beam particle, or whether the trigger was accompanied by the passage of a beam particle through the chambers.

- Other digital information on the event.

  This was pulse height in some counters (in our case the Cerenkov counters), the shunt voltage readings of magnets, and chosen scaled quantities.

- Fixed data.

  This was bookkeeping information such as run number, date, etc.

All of this data was transferred to a computer (EMR - Electro-Mechanical Research Inc. Model 6050) for on-line analysis and permanent storage on magnetic tape. The transfer to the computer proceeded sequentially via a buffered I/O channel. The data from the counters and chambers arrived in parallel (within less than a few hundred microseconds) and consequently had to be stored away in a hardware buffer until the computer was ready for each word of information.

The buffer consisted of units designed to store the different kinds of data mentioned above, along with a controller unit which scanned through the transferred data from each buffer location through an interface to the computer I/O channel. The buffer was a Scientific Accessories Corporation MIDAS (Multiple Input Data Acquisition) system, a brief description of which follows:

The unit which stored spark chamber coordinates, the Model 1148 Scaler Bin, consisted of sets of four scalers, with

each such set assigned to record the locations of sparks in one chamber readout. The input to a four-scaler set was a train of pulses (typical height 3V) where the first pulse represented the front fiducial and subsequent pulses represented the sparks and finally the rear fiducial. The pulse train is a temporal representation of the spatial distribution of sparks. A proportionality factor given by the speed of sound in remendur (5 μsec per inch) and the interfiducial distances, relates the time representation of the sparks to their actual position in space. Values for the spark coordinates in a view were given by the time separation between pulses and the start fiducial, multiplied by the above proportionality factor.

For each spark chamber plane, the data was stored in the four-scaler set as follows: The start fiducial pulse turned all scalers on so they counted at the rate of 20 MHz, subsequent pulses stopped the scalers sequentially--first pulse stopped first scaler, second stopped second scaler and so on. Up to four sparks could be digitized per chamber view; in practice there were usually two or three sparks and the rear fiducial was digitized as the last spark.

The experiment required 48 such four-scaler sets, which received the WSC data from each chamber plane in parallel and held the numbers until they were ready to be sent to the computer. A least count in the 20 MHz clock corresponded to 1/4 mm positional accuracy, however folding in the wire spacing and pulse characteristics resulted in a half mm positional accuracy per chamber view. Finally, each scaler was capable of storing up to

fourteen bits of information.

The fast logic data (tag bits), were stored in the Model 1105 Tagging Modules. Each such module consisted of eight bits where each bit could be assigned to a counter or to some derivative logic signal. A given bit was set in this unit when there was a coincidence between the input at that bit and a fast gate signal, usually derived from the trigger signal. Hence, for the ∿10 nsec after a trigger, the fast logic elements were viewed, that is, the gate was opened for the corresponding bits to be set.

Other digital information, such as scaler or digital voltmeter numbers, were buffered by means of a Model 1115 multiplexer. This was essentially an interface which converted logic levels used in devices such as TSI scalers or voltmeters to standard levels used in the SAC system. In addition, it had the capability of allowing the several devices attached to sequentially transfer their data. Again, the accuracy was up to fourteen bits.

Fixed data used for identification purposes, such as run number, date, run condition, was buffered by means of a Model 1107 Fixed Data Module. Each such unit was capable of storing four three-digit octal numbers set by hand using thumbwheel switches. These numbers were transferred to the computer and recorded along with other data.

We have now arrived at the point in this description where all the data of an event was stored in the buffer either in the form of scaler numbers, or bit configurations, or in devices which could be interrogated by the buffer system. The

next step was to sequentially step through each buffer unit, and through each location in that unit, and transfer the information contained to the computer. The control functions and logic necessary for this was provided by another SAC device, the Model 1204 Master Control, along with the Model 1206 scanner.

The above modules were all connected to each other and to the master controller by a common data bus which consists of twenty parallel lines. In addition, strobe lines emanating from the master controller (either directly or via slave scanners (Model 1206)) went to each module. Since each word of information had eventually to be transferred to the computer in sequence, an ordering of all the buffer locations was made. The order in which modules were interrogated was arbitrarily chosen; e.g., tagging modules first, scaler bins second, multiplexer next, and so on. Data was read out from a particular module when the master controller sent a strobe pulse to the module, causing its contents to be latched on to the data bus line. This description applies to those modules which contained or provided access to only one word of information. The scaler bin was an exception since it contained up to 96 words of spark chamber coordinates which had to be transferred, but had only one strobe line. Scaler bins, therefore, were provided with built in scanners, which accepted successive strobe pulses from the master controller, and routed them to successive scalers for readout until all scalers had been referenced. Only then was the next strobe pulse allowed through to be applied to some other module.

In summary, then, the data transfer for an event proceeded

as follows: The master controller, (MC), received a pulse notifying it that a trigger had occurred. The MC prepared for the data by first clamping all data modules in reset for a selected time interval (18 μsec) so that broadcast electromagnetic noise caused by chambers would not be registered. Simultaneously, the start input was disabled until data transfer for the event was complete, and a wait time was initiated during which all the modules filled up with their appropriate data. Finally, data transfer began when the MC sent a strobe to the first module, so that data appeared on the data bus lines. For each strobe pulse sent, the MC also sent a pulse to the computer notifying it that data was on the lines, ready to be entered in memory. The computer I/O channel and interface controlled the transfer from this point, and sent a signal back to the MC when word transfer was complete. This signal advanced the strobe to the next module or location containing data and then the process was repeated until all data for an event had been read into the computer. A signal from the SAC then notified the computer that data transfer was complete. The full buffer of data was transferred in about 1.5 msec.

E. On-Line Computer[52-53]

The on-line computer was characterized by its ability to communicate with the outside world in real time--by means of signal lines, priority and non-priority interrupts, and a display of chosen quantities as they were calculated. When a given interrupt occurred the computer stopped whatever calculating it was doing, (keeping track of its place, however, so that it

could return to complete the calculation after the interrupt had been handled) and proceeded to do whatever task was appropriate for the interrupt that had occurred. Pulses could be sent out at any point, to be used either for logic purposes (to instruct devices) or to keep track of frequencies of chosen calculated quantities. The human finger could also intervene to cause program branching or to get selected printout by means of six sense switches and 64 sense lines equipped with switches.

In our experiment we had priority interrupt lines which signalled the computer to recieve data, to initialize the data transfer by sending appropriate signals to the SAC buffer, and to branch to the calculation routines. Up-to-the-moment displays were made of spark chamber and counter information and of various data distributions. Of particular use was a CRT scope display of the apparatus showing the chamber fiducials, position of the magnet, counters, and also displaying the particle tracks as they occurred (Figure 11). There were also distributions of spark chamber efficiency, which served as continuous monitors of equipment performance, and which also allowed hardware problems to be traced down quickly. The CRT display proved useful in solving more difficult problems also, by allowing us to see what was happening to each trigger.

For example, we were able to trace the source of spurious background triggers by noticing in this display that many triggers originated at the center of the magnet, in the K-3 chambers. This problem was fixed by requiring a positive coincidence from a counter placed before the magnet.

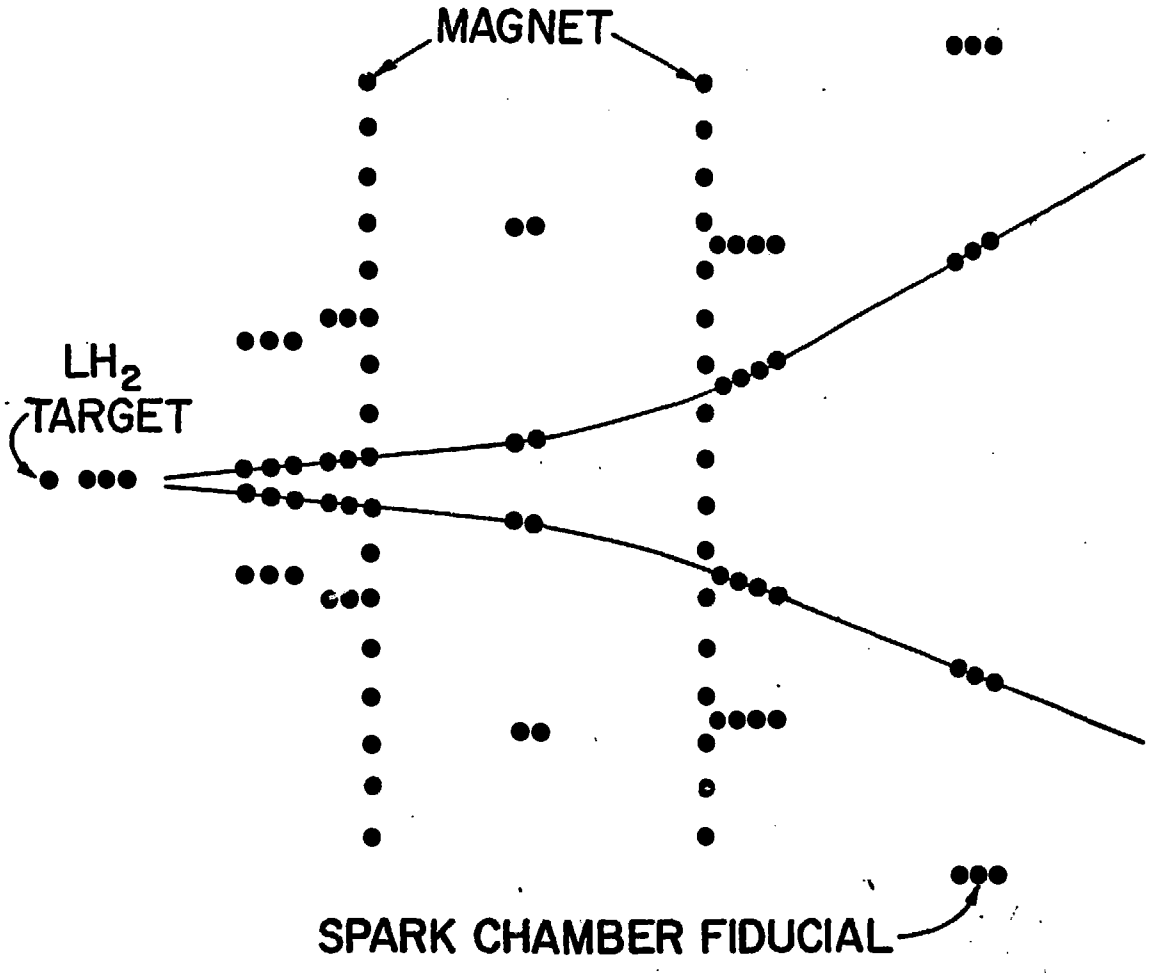

Fig. 11.

Fig. 11.--CRT display of the apparatus

The CRT display of the apparatus could also be used to selectively view particular classes of events. For example, only those events could be displayed which failed at a particular place in the programs (this will be discussed further in Chapter III).

1. Complete on-line analysis

The data rate for the reactions we studied was well matched to the computational speed of the computer. This made possible complete analysis of ∿90% of the events as they were being received in the apparatus and recorded on magnetic tape. We were able to view physics results almost immediately. This was an important advantage which allowed us to easily optimize the experimental run, and in a more general sense was also a satisfying way in which to proceed. We could accurately gauge the rate of data accumulation, and quickly judge how well we were achieving the goals of the experiment, or whether changes were needed.

Finally, the on-line computer proved a patient overseer of most of the operation of a run, once started. The shunt voltage of each magnet in the beam line, as well as the momentum analyzing SCM-105 was checked at least once every 30 seconds. If the reading was not within the specified tolerance, data taking would stop, and a message would be typed out to the experimenter telling him which magnet was off and by how much. The spark chamber readouts were tested for spurious noise each event, and interfiducial distances were required to be within tolerances, or again a message would notify the experimenter which chamber had the problem. The communication link with the SAC buffer and the

operation of the buffer was checked each ZGS pulse, by using a SAC Test Generator to load the buffer with known values, then testing whether these values were in fact received by the computer. The sequence of SAC words transferred is also checked, since part of the word contains its SAC address.

F. Programs

1. General description

During the data acquisition mode the computer cycled through a waiting loop of predetermined duration, where it received the priority interrupts, processed them, and then returned to wait for the next interrupt. When the last interrupt in a ZGS cycle (the end of flattop signal) was received, the data buffer was written out onto magnetic tape, and then control was transferred to an Executive routine. From there, calls were made to the calculation routines in sequence, the failure conditions that each routine set were checked, and appropriate program branches were determined. As each of the major calculation steps were successfully completed, a corresponding scaler was incremented. Hence, the experimenter could pinpoint problems quickly, and more importantly, had a continuous breakdown of the data into the various failure categories. This served as a long term monitor on operating conditions, and also allowed fairly accurate estimates to be made on the quality and quantity of the data at any point in time.

2. Detailed descriptions

The routine FIDDLE converted the spark chamber coordinates

to convenient units for calculations. The constants of the inter-fiducial distances (in space) which had been measured in the laboratory were prestored in the computer, as were the inter-fiducial distance (in units of counts on a SAC scaler).

The SAC scaler numbers were available for every event (for fewer than four sparks in the wand). When no sparks were detected, or there occurred sparks having values outside the fiducial region, a message was output (see above) and the event was skipped. Another important requirement made here was that one out of every ten events have a "stop" fiducial within specified limits. If this requirement were not satisfied, it could mean that the speed of sound in the remendur for a readout was faulty.

The routine COUNTR set a failure flag if the event had a beam track through the spectrometer, and also histogrammed the pulse heights of the Cenerkov counters. This routine also tested for several failure conditions: did the event have an unambiguous trigger? and an unambiguous momentum hodoscope configuration? If the answer to either question was no, then there was no unique specification of the incident beam, and the event had to be failed.

The routine PWC examined the beam wire spark chambers; it calculated the angles and position of the incident beam track and stored them for later use. If no beam track was present, or none could be recovered because of too few sparks, or too many tracks, then the event was failed at this point.

The routine TRAX performed the geometrical reconstruction of

tracks. It operated on the raw spark coordinates and found line segments in front of and behind the analyzing magnet. These line segments were subsequently linked up through the magnet by another routine (using information from the chambers at the magnet center and also the field map description) so that the path of a particle through the spectrometer was recoverd. A brief description of TRAX follows.

The basic strategy in this "filter" program was determined by the arrangement (spacing) of the spark chambers in the spectrometer volume. Ordinarily, one would want to measure the path of a particle at uniform intervals along its trajectory in the detection apparatus (an extreme example being a bubble chamber), since the best spatial resolution is achieved in this way. However, when the detector consists of spark chamber planes, i.e., limited number of digitizations, one may be led to impose other requirements. For example, one wants to be able to interleave counters with the chambers at selected points for greater flexibility in the selection of triggers, and to aid in separating track related sparks from spurious sparks due to chamber breakdowns. Breakdowns may occur at random times, usually in regions of the chambers where there are construction or readout faults. They may also occur in the beam region, where ions may not be cleared out efficiently, especially at high beam fluxes. These problems can be circumvented by grouping several chambers close together in sets, and having several such sets with gaps of empty space between them (available for counters), at intervals throughout the detection volume. Within such a chamber set it is much

easier to distinguish track related sparks from sparks due to other causes.

This arrangement suggested the algorithm of looking at each chamber set independently and trying to find line segments there, rather than attempting the more general approach of looking at all the chambers and trying to make line segments by linking of sparks in one gap with those in all the other gaps. Once a catalogue of all segments was established within all the chamber sets, the next step was to try (separately in the front and rear of the magnet, and separately in the horizontal and vertical views) to link segments between pairs of chamber sets. The technique here approaches a minimum chisquare fit, in the limit of a large number of gaps, and in the limit that the gap separation is large compared to WSC thickness. We drew a line between the centers of two segments in our catalogue, and calculated the sum of the squares of deviations of sparks in the segments about this line. Using reasonable limits, we then established a new catalogue of lines (these were now lines front and back of the magnet, not lines within chamber sets) ranked according to how good a "chisquare" the sparks had to the line drawn through them. Up to four "lines" in each view were found. This essentially completed the job, except that TRAX also used the information from the K1 chambers having wires inclined at ±30° to the vertical to relate the horizontal and vertical coordinates to a particular track, for lines in front of the magnet. (With orthogonal readouts there is an ambiguity as to which horizontal coordinate goes with which vertical coordinate, when there are

two or more tracks through the chambers.) In addition, TRAX set a variety of error flags for the Executive, identifying the reason for an event failure.

This program was written in the assembly language of the 6050 EMR computer. It did all integer arithmetic calculations, and due to the algorithm outlined above was fast enough to be a useful on-line tool. For example, it took about 200 msec to search for and completely analyze tracks due to a K^{O} decay. Background triggers, mostly from gamma ray and neutron conversions, were of course handled with greater dispatch, because they generally did not produce a clean pattern of tracks, and thus failed early in the program.

When TRAX "found" a line segment, it was still possible that there were sparks missing in some of the chambers. (As few as three sparks could comprise a perfectly acceptable line.) Accordingly, it was possible to find the chamber efficiencies by counting the number of lines found, and comparing this to the number of times a particular chamber contributed a spark to a line. These plots of chamber efficiencies were an important on-line tool, which enabled us to quickly discover problems in the operation of the spark chambers.

The remaining task in the analysis, before we could try fitting the event to various physics hypotheses, was to link up complete line segments through the magnet, and to calculate the momenta of the tracks. In the routine ORBIT, extrapolations were made of the lines from the front and from the rear to the center of the magnet. If the two extrapolations intersected at

the magnet center line to within a tolerance, an initial estimate was made of the momentum, and then an attempt was made to calculate the momentum of the particle through the field. A brief description of the momentum calculation routine follows.

3. Momentum analysis[54]

The geometrical reconstruction identified the measured coordinates at all the chambers and linked them together as points on a particle track. The momentum of the track was then calculated, in preparation to fitting the tracks to various possible kinematic hypotheses.

The momentum of a particle which traversed a region of magnetic field can be obtained from a knowledge of the field and a measure of the bend in the path of the particle in the field by

$$p = \frac{\int B \cdot dl}{\theta}$$

θ - bend angle

p - momentum

B - magnetic field

A good approximation to the numerator can be obtained (for each track) by expanding the field and the Lorentz force equations over small step distances and integrating along the length of the trajectory. The step distance is determined by the grid size of the measured field map. For example, to keep expansion terms up to quadratic order one would need to choose a step size to make the field vary no more than quadratically between measured points. As this method is very slow and required too much computer memory storage, a more economical method was used.

In this method (Predictor-Corrector) the Lorentz force equations were integrated analytically in four large ($\sim$20") steps

through the field. For each step, the integration limits (endpoints of the step) were chosen to correspond to nominal spark chamber locations. With the integrated force equations, coordinates and angles at an endpoint were expressed in terms of coordinates and angles at the beginning point, and also in terms of integrals of field components along particular orbit trajectories.

The integrals were of the form

$$\int_{y_1}^{y_2} A_n(y) B_n(x,y,z)\,dy \qquad (1)$$

where x, y, z, are the coordinate axes to the beam's right, along the beam, and vertical, respectively. The integral is the polynomial representation of the field along a given trajectory defined by x(y), z(y); A_n are coefficients depending only on y, and B_n are chosen polynomials in x and z. One way this method achieves economy is by avoiding storage of the many coefficients A_n at each point in space. Approximating B_n by a series, $\sum_{k=1}^{4} b_n^k f_k(y)$ then

(1) becomes $\sum_{k=1}^{4} b_n^k \int_{y_1}^{y_2} A_n(y) f_k(y)\,dy$.

This has the virtue of separating out the integrals which depend only on y, which are hence independent of particular orbits. These integrals need only be calculated once, and they contain in compact form the information resident in the polynomial coefficients. Instead of saving ∿20 of these coefficients along each step through the field, just one is saved--the integral of the

coefficients multiplied with known functions $f_k(y)$.

The coefficients in the series representation for B_n are the terms in the calculation of (1) which depend on particular orbits. The functions $f_k(y)$ were chosen in advance using the knowledge of the form of the polynomials $B_n(x,z)$. Terms in b_n were calculated starting with the measured coordinates and slopes at the beginning of an orbit, then calculating coordinates at the endpoint of a step, and finally checking once to correct the initial quantities. After one iteration, endpoint quantities were found to have converged sufficiently.

The precision of this predictor-corrector tracking method was tested by generating orbits of chosen momentum and angle through the field using the Runge-Cutta integration prescription. The orbits were then reconstructed by the predector-corrector technique, and since the "true" orbits were known the reconstruction error could then be obtained. The error in momentum was found to be small compared to momentum error due to spark chamber resolution and multiple scattering. Figure 12 shows Δp (reconstruction)/σ_p (wsc resolution) for 400 generated events.

The momentum, coordinates, and angles of a particle track at the production point are parameters in the orbit trace through the field. Starting with estimates for these parameters, the orbit is fitted to measured coordinates. Adjustments are made to parameters to minimize the χ^2 of the fit. For successfully converged fits, the momentum was then recovered as one of the final parameters for the orbit.

The efficiencies of the programs will be discussed in Chapter III.

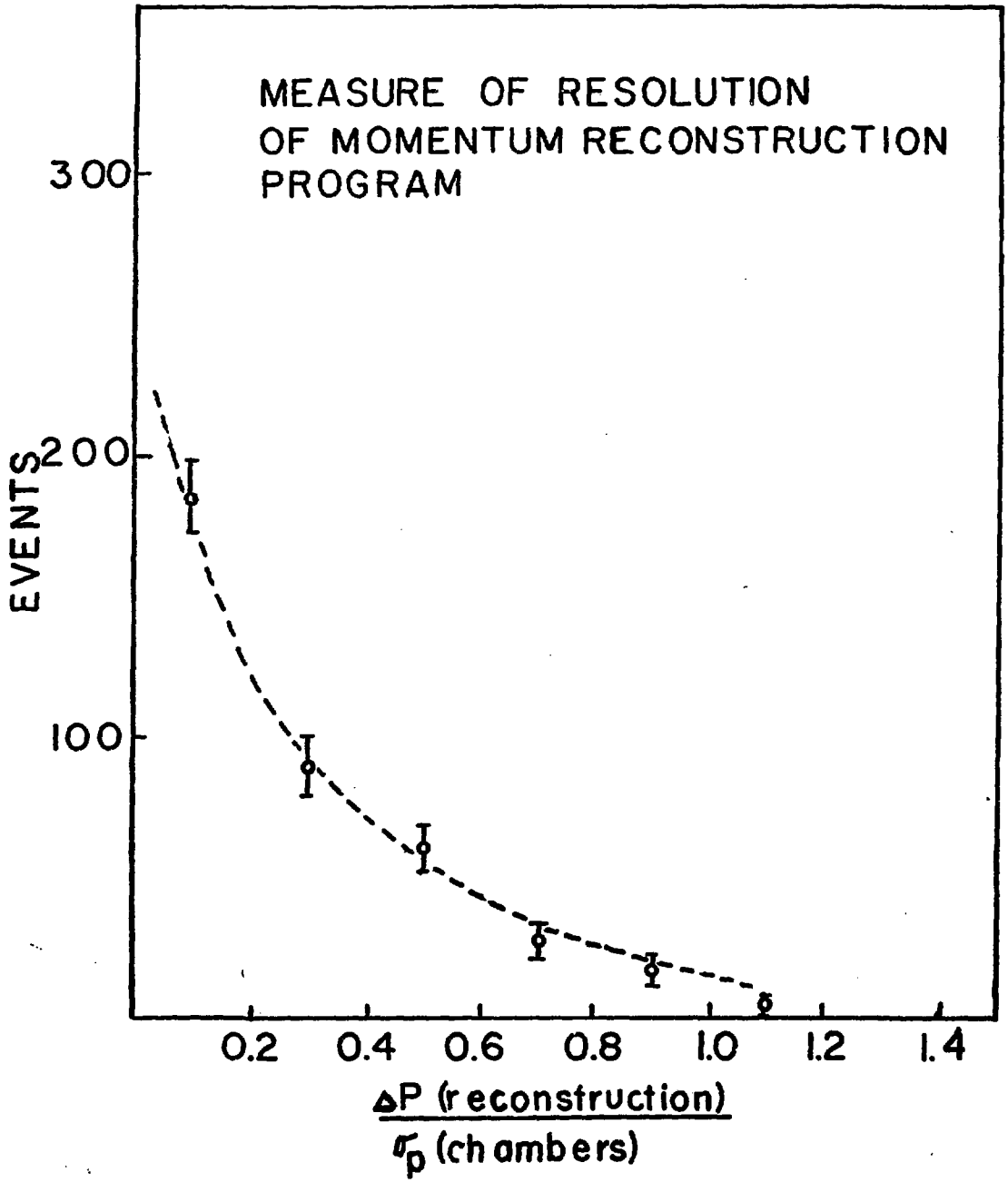

Fig. 12.

Fig. 12.--Resolution of momentum analysis program

CHAPTER III

DATA AND ERROR ANALYSIS

I. Introduction

Most High Energy Physics experiments are hybrids of several complex systems, hardware and software, linked together and interacting with each other. There are individual efficiencies for the component systems, and there is an overall efficiency for the whole system ("spectrometer"), which may include effects due to the interaction of the parts. To obtain quantitative information on measured quantities, one must weight each event which passes the battery of hardware and software tests with the reciprocal of the probability of its overall detection efficiency. There are usually a wide variety of items under the heading of "corrections to the data"; we distinguish two major categories, corrections derived from the data distributions and corrections derived independent of the data.

Under the first category, we include the following discussions. Section IIA deals with corrections to the beam flux. Section IIB discusses inefficiencies in the reconstruction programs, earlier described in Chapter II. Section IIC deals with corrections due to kinematic ambiguities, and Section IID with corrections for backgrounds which may erroneously be

included in the data. Finally, in Section IIE we discuss those events for which no satisfactory kinematic hypothesis was found.

Under the second category of corrections, Section IIIA will discuss the geometric acceptance calculation, which used the Monte Carlo method. Section IIIB discusses calculated corrections, including such effects as scattering, interactions, decays, delta rays, and so on. Finally, Section IIIC reviews overall consistency checks and gives a summary of the normalization uncertainty. In addition, we will discuss the problem of double counting the corrections in those sections where we found it to be a significant effect.

II. Corrections Derived from the Data

A. Corrections to the Beam Flux

A beam particle was defined by scintillation and Cerenkov counters, and by a group of spark chambers, as previously discussed. It was necessary to reject about 20% of the beam particles so defined because of certain losses. For example, 1) there was an ambiguous pattern in the momentum hodoscope; 2) there were too few (zero) beam tracks; or 3) too many (two or more) beam tracks present in the beam spark chamber; 4) a beam track passed through the apparatus within the resolving time of the chambers. For cases 1, 3, and 4 above the losses were random, i.e., the fraction of good events in these categories was, within the errors, the same as that for bona fide beam particles. For category 2 the loss was not random, and a correction had to be applied accordingly. For the random losses the fraction

of observed good events was simply scaled up by the appropriate factor.

The contamination of the beam due to e^- and μ^- was measured using a Cerenkov counter[55] and a correction of $\sim$5% was applied. Finally, corrections of $\sim$2% were applied for beam particles which interacted or decayed in the beam line.

B. Program Efficiencies

1. Reconstruction efficiency

The efficiencies of the analysis programs were determined by "visual" scanning of a limited sample of events, using a CRT display scope, and by studying the effects of using wider tolerances in each routine. Empirically determined criteria were applied to events as the calculation passed from one program to another. The processing stopped at that point in the analysis stream where an event failed to meet a given test; events had to pass all tests in order to be included in the final data distributions. For each failure category (there were several for each routine) we were able to examine events in complete detail and reconstruct the reason for the failure. It was possible to view a CRT display of an event, and to print out various measured and calculated quantities for the event. We then estimated how good a job a particular program was doing in passing good events and failing bad ones, by relying ultimately on the judgment of physicists. Physicists looked at events in each failure category. Events judged to be legitimate failures were sorted from those good events which appeared to fail due to a program error or due to too stringent a tolerance. The

human eye is much better at pattern recognition for something like the typical "vee" particle pattern produced by a $K^o \to \pi^+\pi^-$ decay (Figure 11) than is a computer program. Using the visual display of the events, it was quite easy to distinguish V particle triggers from other triggers. The programs are designed to be analytic, that is, to reconstruct tracks out of individual sparks (see IIB) and they do not use the overall pattern of the sparks. We believe the scanning to be more reliable and depend on it for determining the efficiencies of the programs.

For each failure category i we thus determine the fraction f_i of events which ought to have successfully passed the analysis at this point. We can easily tally up the ratio C_i of failures in category i to total successes, and finally sum over all categories i to obtain the overall correction factor f due to program inefficiency:

$$S_T = S_e + \sum_{i=1}^{k} f_i N_i = S_e (1 + \sum_{i=1}^{k} f_i c_i) = S_e f$$

(S_T = corrected number of total successes, S_e = uncorrected number of total successes, N_i = number of events in failure category i.) For example, preparatory to momentum analyzing the particle tracks, we took the precaution of requiring them to be continuous lines through the magnetic field. Line segments from the front and rear of the magnet were extrapolated to the center and required to meet there within a tolerance. A small fraction of the time (~2%) this requirement was found to eliminate perfectly good events. That these were, in fact, good events was established by making the association of front-rear line segments on the

basis of the more complete information from both the horizontal and vertical views of the event. The "eye" not only extrapolated the segments to the center of the magnet (a requirement which is approximate--not all segments meet in the center), but could judge whether the segments would meet anywhere in the field, which is an exact requirement. In addition, when there was more than one track, the typical "vee" particle spark pattern could easily be recognized. Other failure categories included: an insufficient number of straight line segments in the chambers, bad matchup of line segments between two chambers and so on. Table 3 summarizes the corrections found by scanning.

TABLE 3

PROGRAM INEFFICIENCIES FOUND BY SCANNING

Beam momentum:	3	4	5	6
TRAX Front	3.3±1.3%	..4±0.9%	.8±.5%	0 ±.4%
TRAX Rear	2.8±1.6	2.3±1.2	1.6±.8	2.5±.9
ORBIT	2.7±1.0	2.4±0.8	1.0±.5	.5±.3
FITT	4.3	4.3	4.3	4.3
	13.1±2.3%	11.4±1.7%	7.7±1.2%	7.3 ±.1%
After decay subtraction and averaging:				
	4.7±3%	4.7±3%	4.7±3%	4.7±3%

2. Momentum analysis efficiency

The momentum analysis routine (FITT) was the last in the chain of event reconstruction programs. Events passing FITT went

on to the next major analysis stage, that is, the fitting of kinematic variables to various physical hypotheses. This fact allowed us to improve on the determination of the FITT program efficiency over that obtained from the scanning technique. Now, failing events could be passed in FITT by relaxing the FITT program tolerances, allowing them to be analyzed by the kinematics routines. This allowed more insight to be gained into the nature of the failing events than was possible from the geometric considerations of scanning alone.

As we did for the other programs, we first scanned the events which failed in FITT to determine the fraction of these which appeared to be good events. One scan was done using the normal FITT χ^2 tolerances (see Chapter II, sec. IV.F for FITT description), and one scan with these tolerances greatly enlarged. Table 4 summarizes the results. The correction factor obtained for the large χ^2 tolerances was negligible (factor of $\sim$35 smaller) compared to that for the normal χ^2 values. In other words, nearly all the events which failed with the normal χ^2 were passed with the large χ^2 values. This assures that if we use the larger χ^2 tolerances, the kinematics routines will be operating on almost all of the events normally failing in FITT, so that valid (normalized) comparisons can later be made of the efficiencies found by programs and by scanning.

Proceeding to the kinematic analysis, and using the large χ^2 events, we calculate the K^o effective mass. For the identical data, but now using the normal χ^2, we again plot the K^o effective mass (Figure 13(a)). Subtracting the two distributions gives

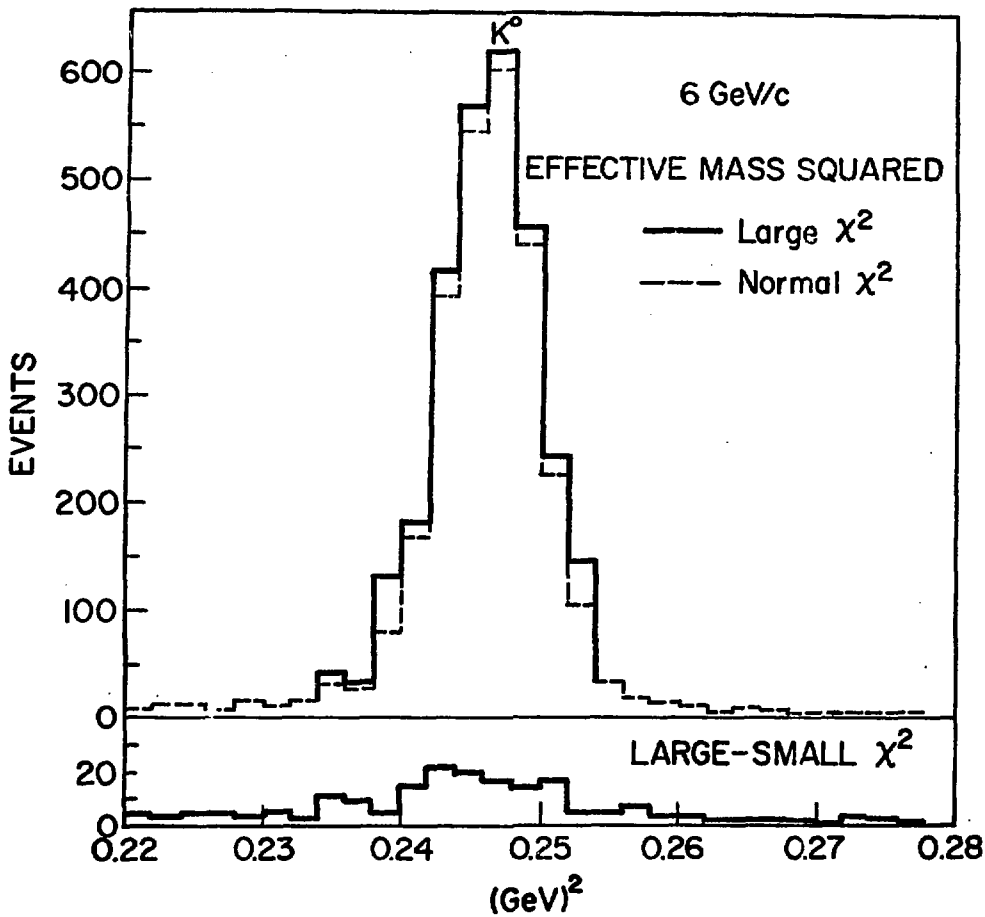

Fig. 13 a.

Fig. 13 a.--K° Effective Mass Distribution for Events with Normal (Upper histogram), and Large (Lower histogram) χ^2 Values in the Momentum Analysis Program FITT

the effective mass of the events which ordinarily fail in FITT (Figure 13(b)). This distribution shows a clear peak at the K^o mass, with a width that compares well with that found in the good data. After making background subtractions, we finally obtain the fraction of the failing events which are kinematically identified to be good K^o's. Table 4(b) summarizes the results.

As a consistency check, we compare the scanning and the program results. According to scanning, there should be an 8.5%±1.8% correction, approximately independent of momentum, in the number of total successes. This compares well, within the errors with a 9.4±.5% increase in the number of "successful" events found by the kinematics routines when the large χ^2 tolerances are used. However, after imposing cuts on effective mass width and subtracting background on the large χ^2 events, we find that the correction obtained by using the programs is 4.3%±.4%. That is to say, of the ∿8.5% events that appear to be good vee particles by "eye", only about half, or 4.3% turn out to be K^o's or Λ^o's.

The vee events identified by the scanning but rejected by the kinematics (a difference in the correction of ∿4.2%) are what populate the background under the K^o peak in Figure 13. In general we have no testable hypothesis as to the physical origin of this background; however, we can make some definite statements about physical processes that do <u>not</u> contribute to this background.

For example, we consider the possibility of e^+e^- pairs from γ ray conversions, since our neutral trigger frequently selects events with many γ's in the final state. By assigning electron masses to the tracks we are able to calculate the

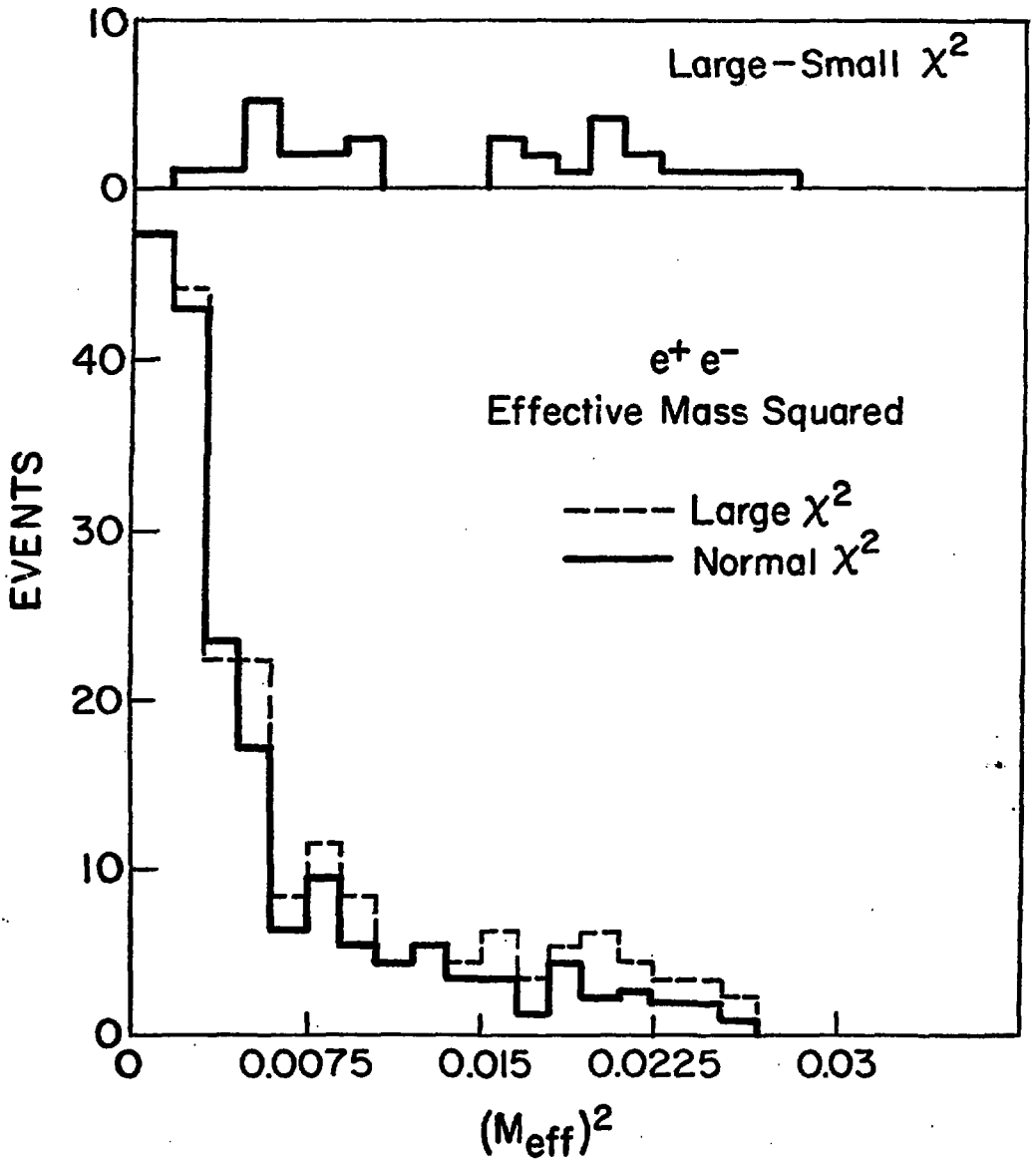

Fig. 13 b.--Test of Whether Events Failing the Momentum Analysis Program are e^+e^- pairs. Top Histogram Shows e^+e^- Effective Mass of Failing (Large χ^2) Events. The Distribution does not Show a Peak at zero, as is Typical for True e^+e^- Events (Fig. 16 a.)

e^+e^- effective mass for the events having large FITT χ^2. Comparing the resulting distribution (Figure 13b) with a typical e^+e^- effective mass spectrum (Figure 16(a)) (which we obtained by other means), we see that the large χ^2 events do not evince the typical peak above background at small values of effective mass. We conclude that e^+e^- pairs do not contribute to the background under the K^o peak, for the events with large FITT χ^2's.

Given the measured quantities available, we can know little else about this background. We note that it is flat, in fact we estimate the level by extrapolating from either side of the K^o effective mass region in the distribution of Figure 13a. The final FITT program efficiency is obtained by subtracting the background in the region of the K^o mass. We assign some systematic error in this procedure ($\pm\sim$2.5%) in consideration of the fact that in principle it is possible that a fraction of the background events may be actual decays of $\pi \to \mu\, \nu$ or small angle π elastic scatters. The systematic error arises from possible double counting, since corrections for decays and scatters are applied elsewhere. We conclude that the correction due to inefficiency of the momentum analysis routine FITT, found by kinematic analysis of events failing in FITT, is 4.3%±2.5%.

TABLE 4

(a)
FITT SCANNING

χ^2	#FITT fails/success	V-part./fail.	V-part./success
nominal	30.4 ±.7%	33.8±6.0%	8.5±1.8%
large	1.48±.17%	20.0±9.0%	0.3±0.%

TABLE 4

(b)
PROGRAM RESULTS ON FITT FAILURES

Inc. Momentum	Events in K^o peak	Large χ^2 events	V-part./succ.
3	440	20	4.5±1. %
6	2651	113	4.3±0.4%

3. Track coalescence

A possible loss or inefficiency may occur when two tracks from a vertex follow nearly the same trajectory. A spark chamber cannot resolve two sparks which occur $\lesssim$0.2" apart due to the magnetostrictive readout technique. Current flowing in adjacent wires, for example, produces a double humped pulse, digitized as only one coordinate by the SAC scaler pulse-center-finding circuit. Two almost collinear tracks, as might result from a $\phi \to K^+K^-$ particle decay, would be very inefficiently detected by the spark chambers; most of the time only one track would be seen, and it would be difficult to reconstruct the ϕ particle event. We gave the example of the $\phi \to K^+K^-$ because its low Q value (31 Mev) makes almost collinear laboratory K^+K^- very likely for incident beam energies of around 3 - 6 GeV/c.

We investigate this effect for the decay $K^o \to \pi^+\pi^-$ in the data by plotting the number of reconstructed K^o's as a function of the $\pi^+\pi^-$ track separation in the front chamber set K1 (see Figure 14). Comparison with a similar distribution produced by a Monte Carlo program can indicate whether such an inefficiency is present, and allow us to calculate its magnitude. Figure 14

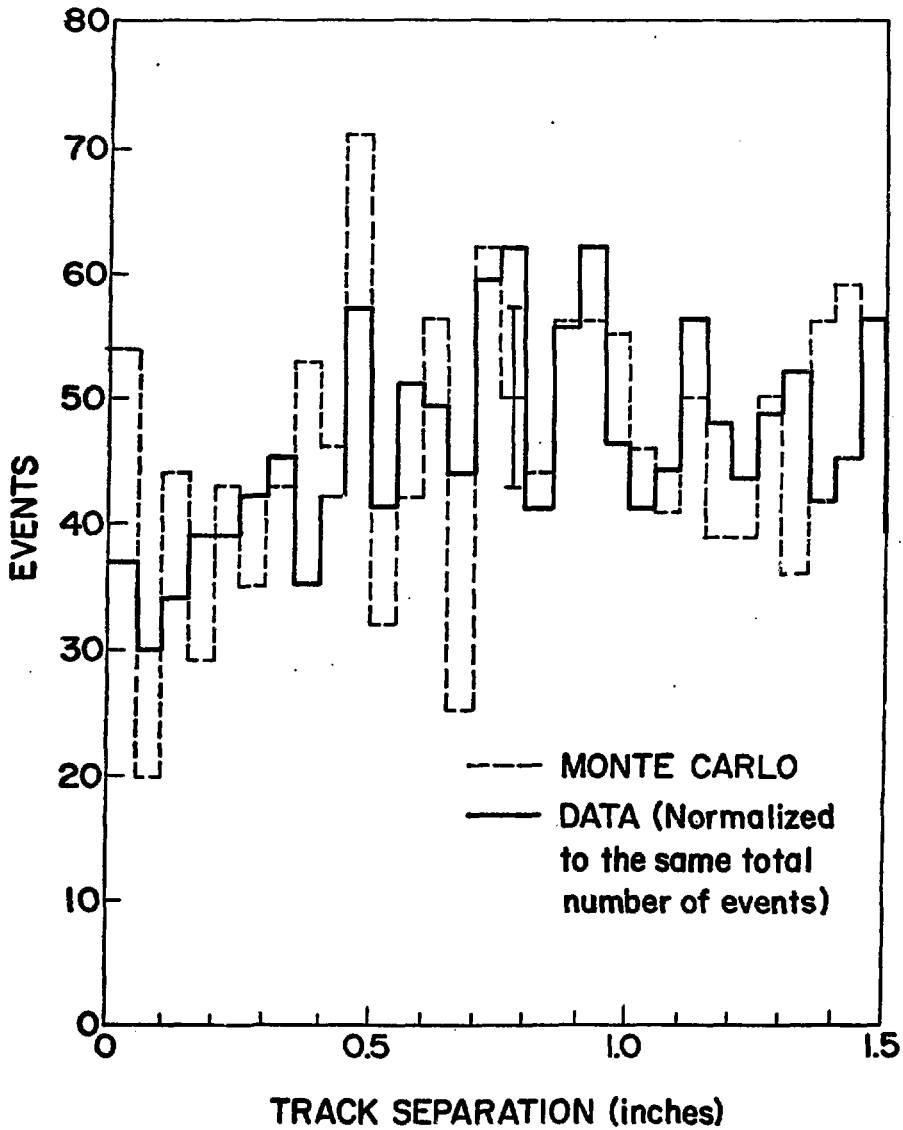

Fig. 14.

Fig. 14.--Number of reconstructed K^{o}'s as function of $\pi^{+}\pi^{-}$ horizontal track separation

shows the distribution for the data, and for the Monte Carlo events, normalized to the same number of events. Figure 15 is a histogram of the number of K^o's as a function of track separation in the ±30° views in the K1 and K2 chambers. The curve represents the Monte Carlo results. Within the errors, we see no inefficiency due to track coalescence for K^o decays. The large Q(220) MeV of the K^o decay is responsible for this in large part; however, we also were aware of this problem early on and gave special attention to it in the reconstruction routine. That is to say, whenever two or more tracks were detected in all chamber sets except the front K1, we assumed coalescence had taken place, and remedied the situation by simply using the K1 coordinates twice in the analysis for that event.

The way that possible coalescence of tracks would manifest itself as an inefficiency in our system, was that such events would fail in the geometric reconstruction program under the category of "not enough tracks ($\geq$2) in the K1 chamber" (called category A here for short). We found in fact that failures in category A were quite frequent--three for every totally successful event. As a check on the above Monte Carlo result, and also on the scanning technique as applied to the geometric reconstruction, we examined failure category A in greater detail.

From the scanning, we distinguished three main types of events in category A. Ninety percent of the time there was no clear pattern of continuous tracks through the spectrometer, due probably to interactions of neutrons and also γ-ray conversions; these were classified as legitimate failures. (This type of event

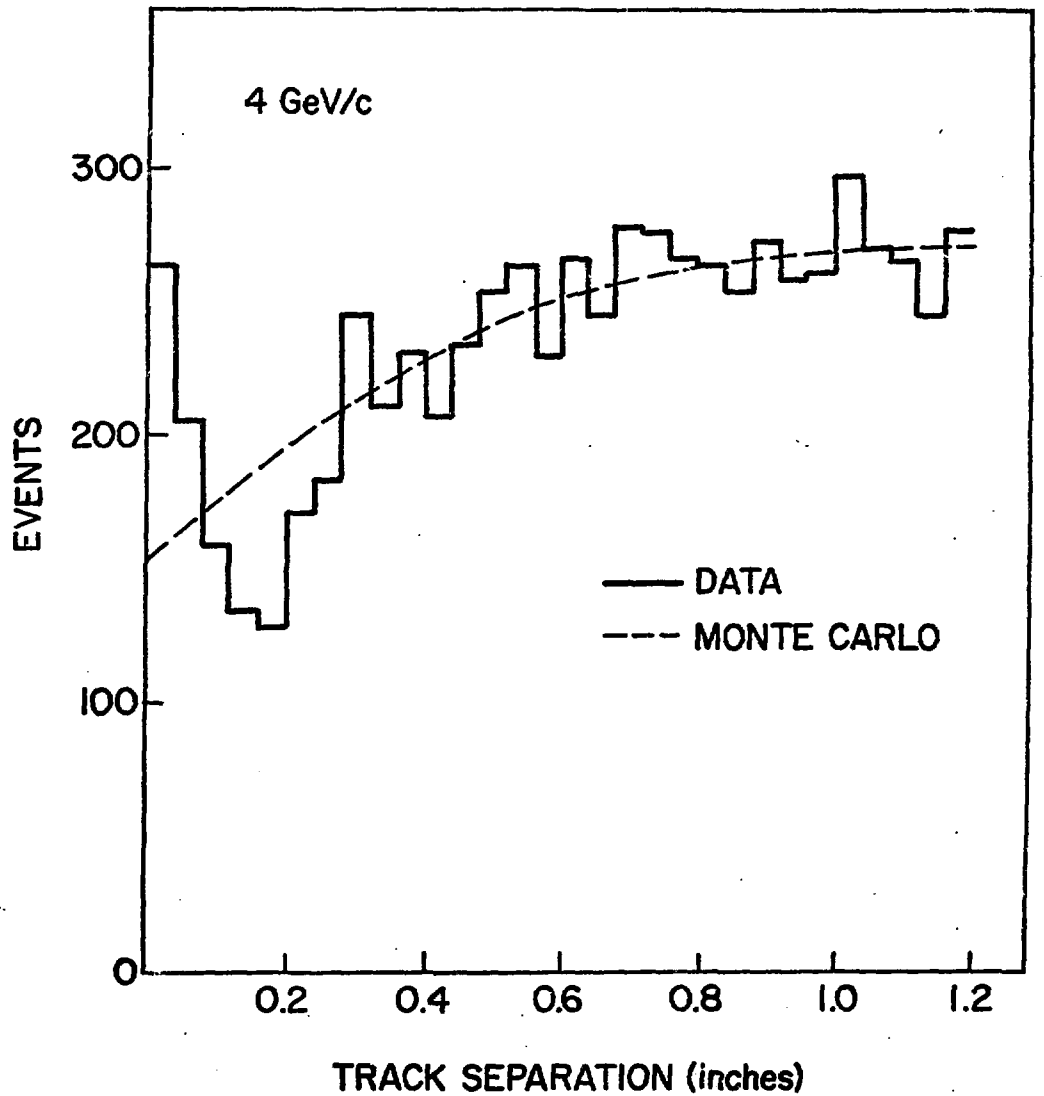

Fig. 15.

Fig. 15.--Reconstructed K^{o}'s vs. track separation, inclined readout view

would have failed in any one of several other categories, and ended up in category A simply because A was early on in the routine.) About eight percent of the category A failures showed a good "vee" particle pattern in the spectrometer, and upon hand calculation we found that these events had only slightly exceeded a tolerance; these were the events for which we had to correct (see Chapter II, IV. E). Finally, 2% of the time a good "vee" particle spark pattern was present, except that there was only one track visible in the front chambers. Here the geometrical configuration could tell us nothing about what the event was physically--whether it was a K^o or Λ^o or e^+e^- or ρ^o or any other hypothesized "vee" particle.

We then applied kinematics, trying various hypotheses and calculating effective mass. Figure 16(a) shows the effective mass distribution under the assumption that the spectrometer tracks were e^+e^-, Figure 17(a) under the assumption that they were $\pi^+\pi^-$, and Figure 17(b) under the assumption that they were $p\pi^-$. We conclude that these are primarily e^+e^- events coming from the conversion of γ-rays either in the CM counter or in one of the K1 chambers (Figure 3). Some of the events do fall in the K^o and Λ^o mass region. After subtracting background we find .15 ±14% of the failures may be true K^o's and 0 ±3% are true Λ^o's. Our conclusion is that the Monte Carlo result--namely that there was negligible loss of K^o's due to front coalescence, is verified and also that the scanning is reliable, since it did not miss a significant number of K^o's.

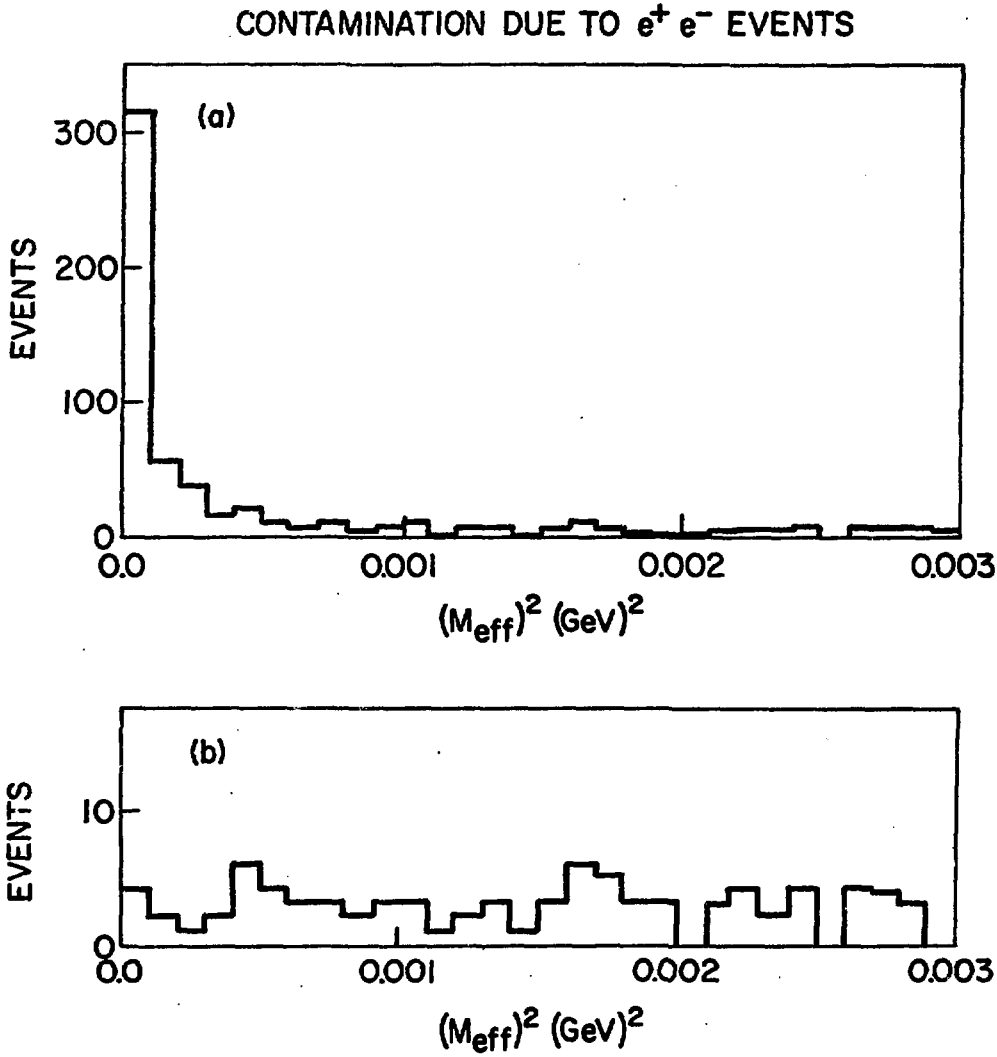

Fig. 16.

Fig. 16.--Study of e^+e^- effective mass as source of contamination. (a) e^+e^- mass distribution for known e^+e^-pairs; (b) e^+e^-mass distribution for events within K^o mass peak

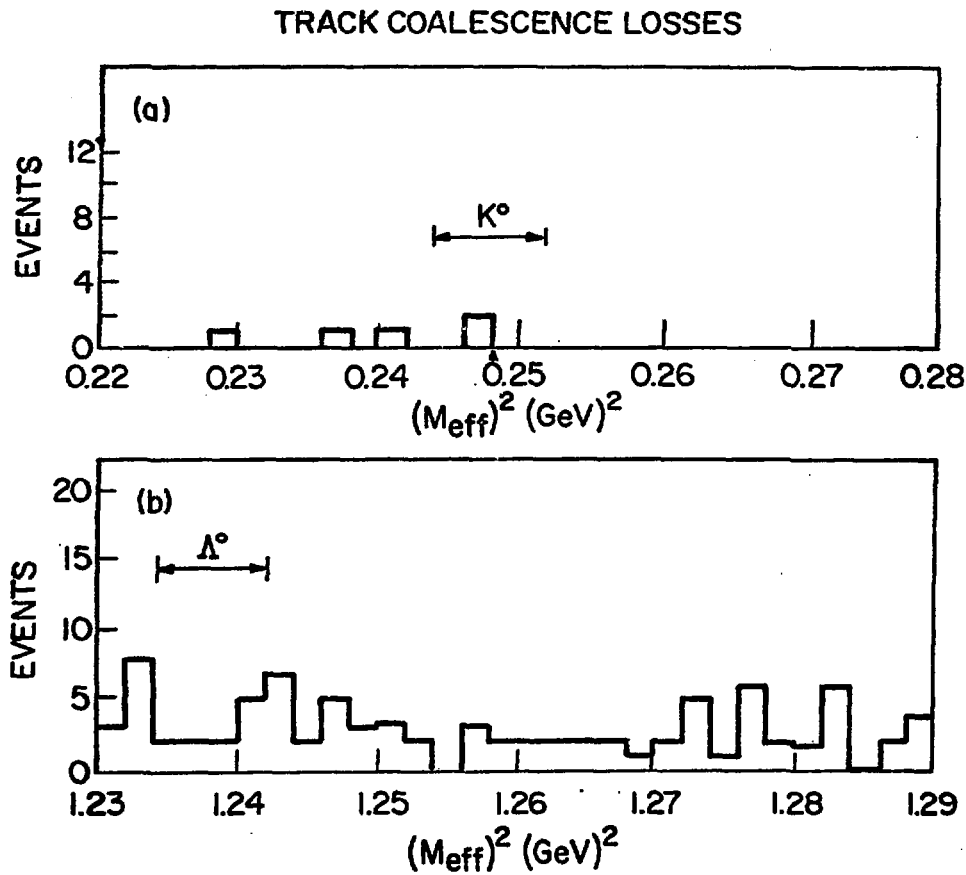

Fig. 17.

Fig. 17.--K° and Λ° effective mass for front coalesced events

C. Kinematic ambiguity

We now turn to corrections arising from kinematic ambiguities in the identification of events. It is possible to misidentify a $\Lambda^o \to p\pi^-$ decay as a $K^o \to \pi^+\pi^-$ decay for certain ranges of proton and π^- momenta, such that when the π^+ mass is assigned to the proton track, the calculated effective mass is close to the K^o mass. We calculate the correction as follows:

First we assume the $\pi^\pm$ masses for the two spectrometer tracks and calculate the $\pi^+\pi^-$ effective mass. For illustration purposes we use data at 3 GeV/c, shown in Figure 18. Events within the dotted lines are normally fitted to the K^o mass. We want to find the fraction of these events which in fact are really Λ^o's, "accidentally" considered to be K^o's due to kinematic ambiguity. To do this we take those events inside the K^o cut, assign the proton mass to the positive track (and π^- mass to the negative track), and plot the effective mass distribution in Figure 19. We see a distinct peak at the Λ^o mass above a background of true K^o's. Three percent of the K^o's appear to be these misidentified Λ^o events. That these are mostly events of the kind $\pi^- p \to \Lambda^o K^o$ (Λ^o forward) is further borne out by looking at the missing mass from the Λ^o. Figure 20 shows the clear peak in missing mass at the K^o mass, as expected for such events.

Not all of the 3% misidentified Λ^o's which slip in as K^o's contaminate the data. This is due to the fact that good $\pi^- p \to K^o \Lambda^o / \Sigma^o$ events must pass a cut on the missing mass from the K^o. We find the proper correction factor by taking the misidentified events which we now know to be Λ^o's, purposely consider them

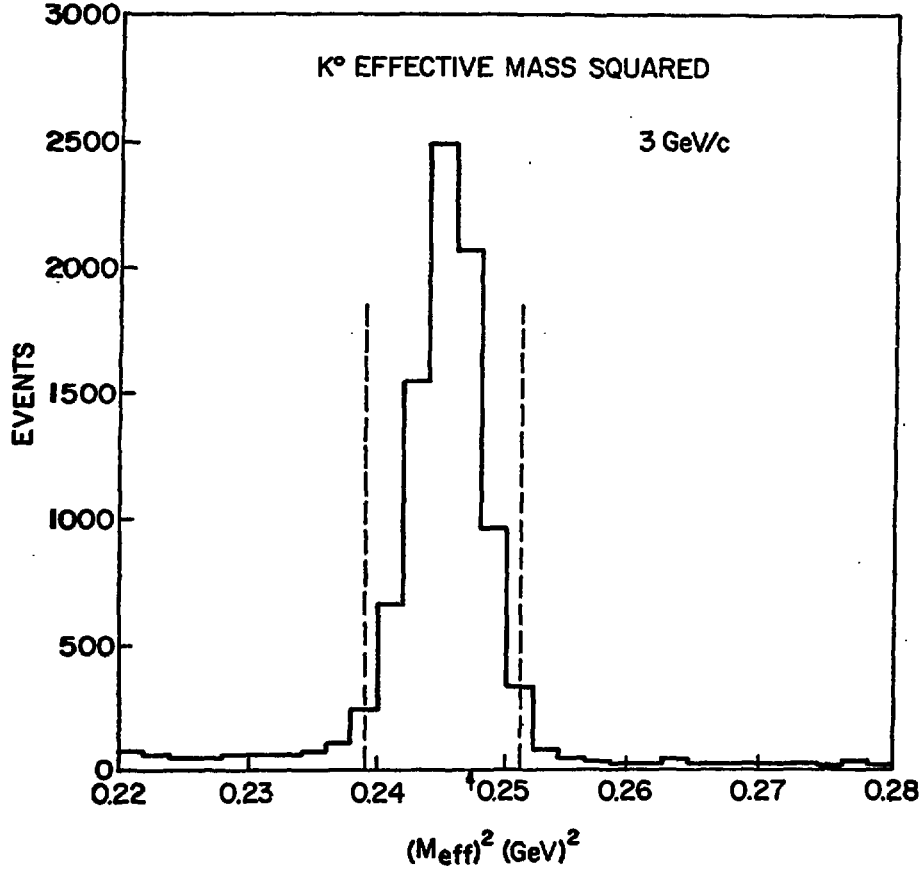

Fig. 18.

Fig. 18.--K^{o}, Λ^{o} cross contamination studies--K^{o} effective mass

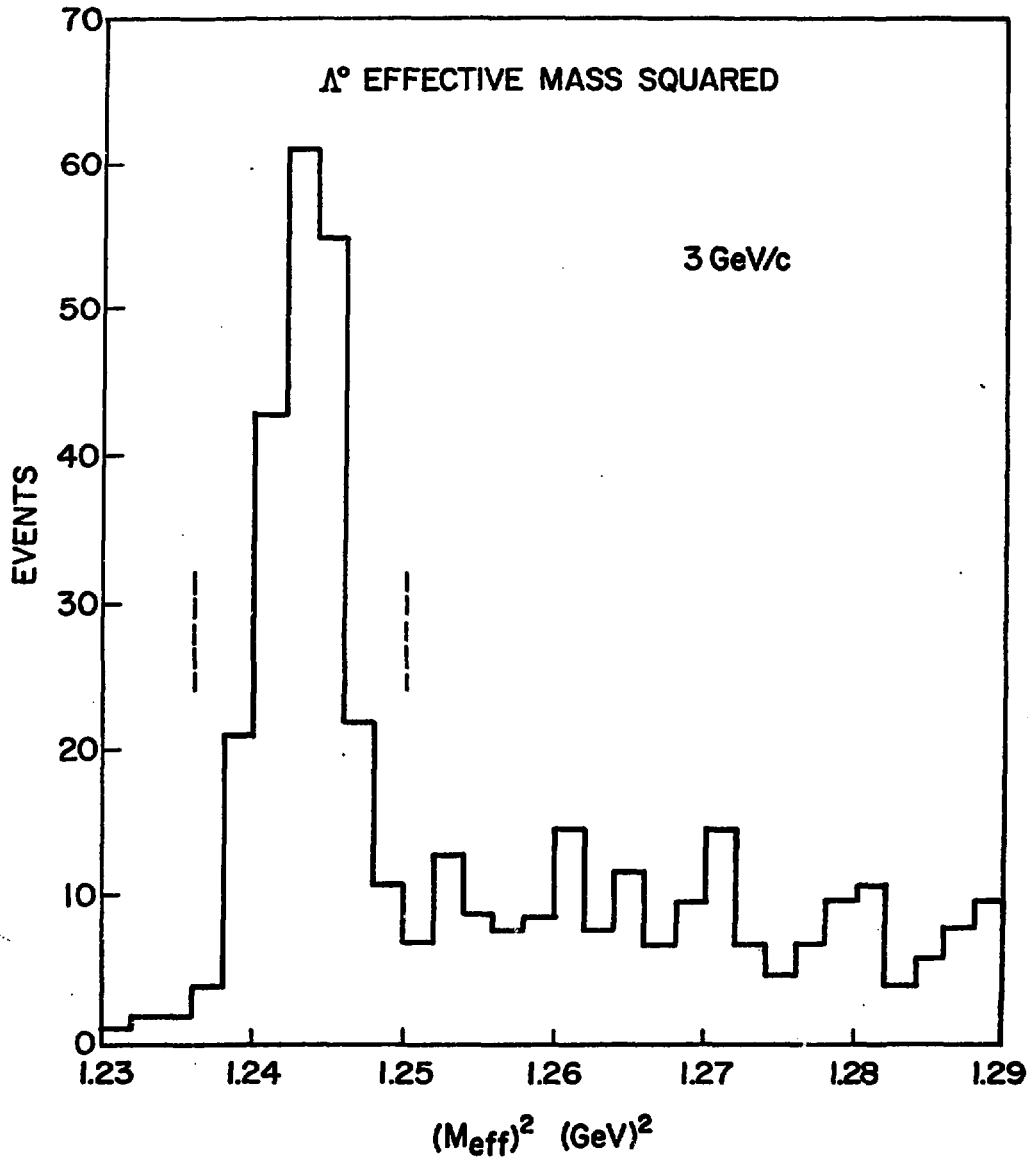

Fig. 19.

Fig. 19.--K^{o}, Λ^{o} cross contamination studies--Λ^{o} effective mass for events identified as K^{o}'s

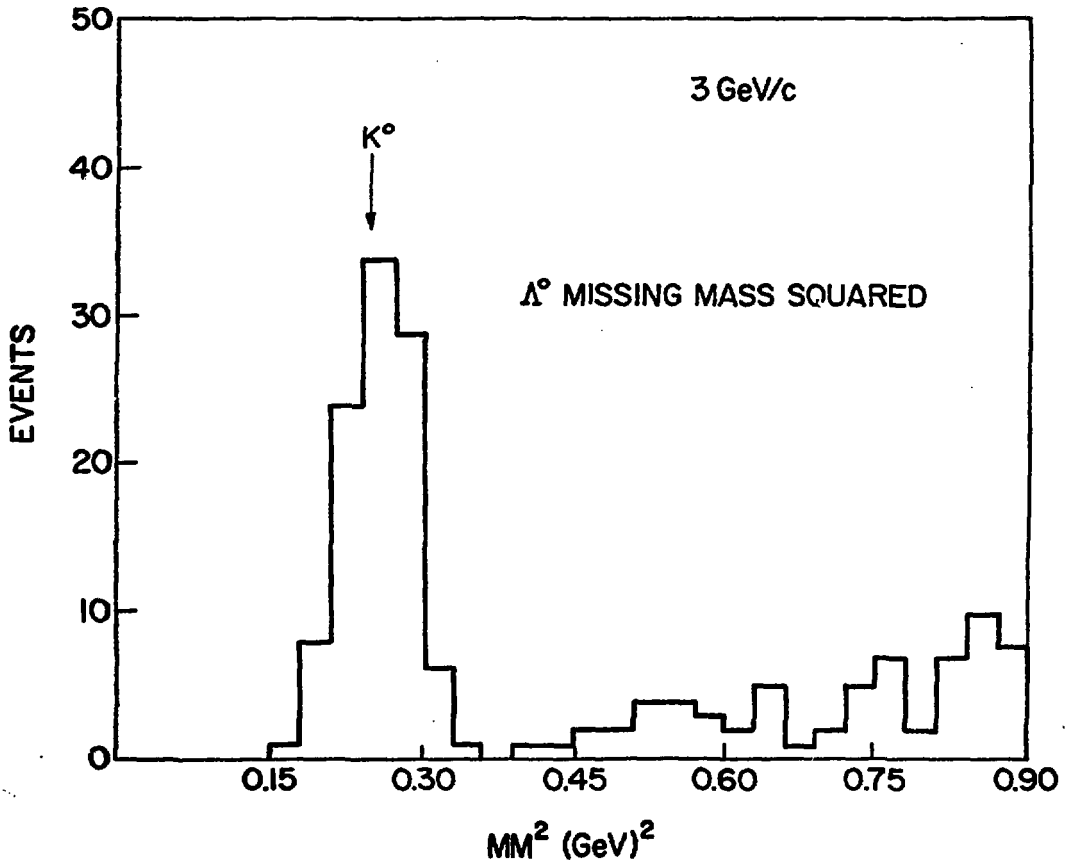

Fig. 20.

Fig. 20.--K^{o}, Λ^{o} cross contamination studies--missing mass from Λ^{o}'s in Figure 19

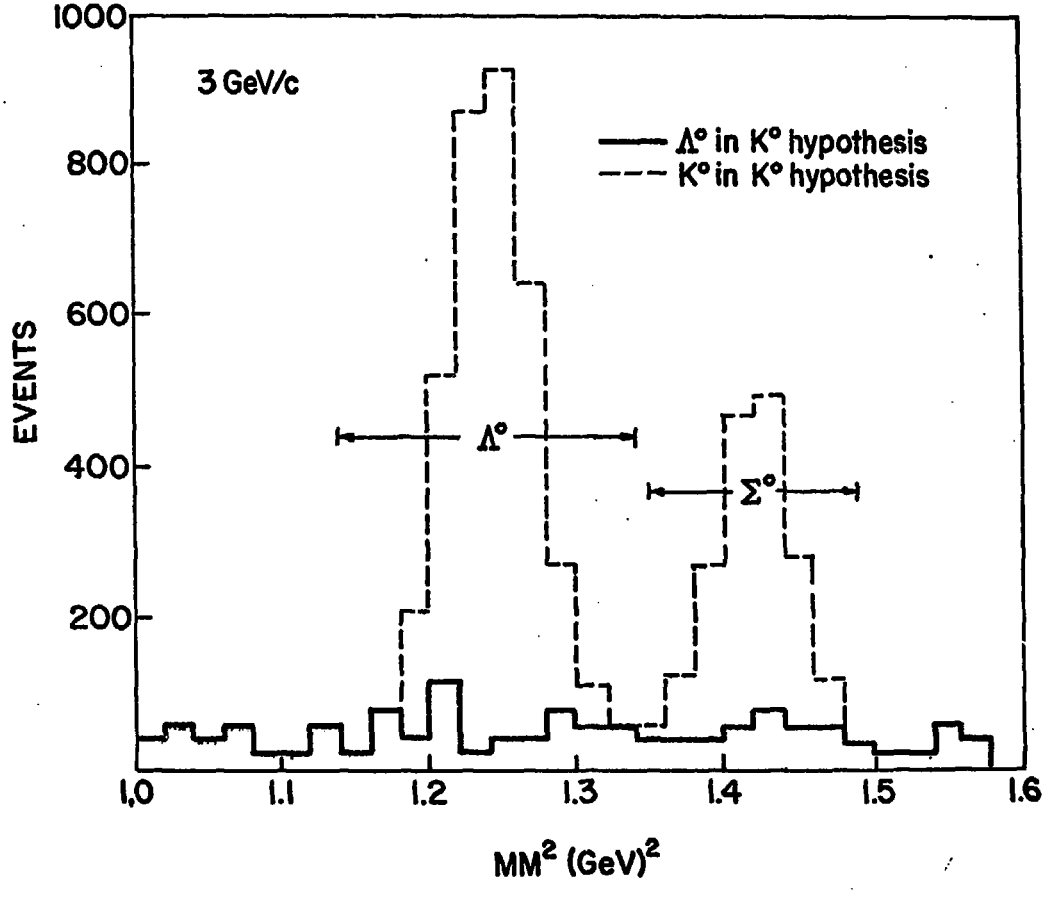

Fig. 21.

Fig. 21.--Missing mass from Λ^{o}'s in Figure 19, hypothesized as K^{o}'s

to be K^o's, and plot their missing mass. Only events in this missing mass distribution which satisfy the usual cuts placed on good data contaminate the data. Figure 21 shows this plot (solid line) and also shows for comparison the scaled-down missing mass distribution from true K^o events (dotted line). Final correction factors found in this way are summarized in Table 5 as a function of incident beam momentum.

D. Backgrounds

1. t-dependence

Since we measure $\frac{d\sigma}{dt}$ it is important to study the behavior of the background as a function of t. For example, if the background increased at higher t, the measured $\frac{d\sigma}{dt}$ distribution would be inflated there unless a t dependent correction factor was applied.

We study this correction by plotting the missing mass distribution for the data as a function of t; Figure 22 is a plot of missing mass from the K^o at incident beam momentum of 3 GeV/c. The dotted curve is for events at large $t(|t|>.2)$, the solid curve for events at small $t(|t|<.2)$, and the two histograms are normalized to have the same number of events in the Λ^o peak.

What is relevant to possible t-dependence of the background, is to compare the size and shape of the background just above the Σ^o missing mass cut (at about 1.5 - 1.6 GeV^2) for the two t regions. Within the errors it is evident that the distributions show no t-dependence in the level of background that may slip in under the Λ^o - Σ^o peaks. We apply the same analysis to data at incident beam momentum of 6 GeV/c, with the same results (Figure 23).

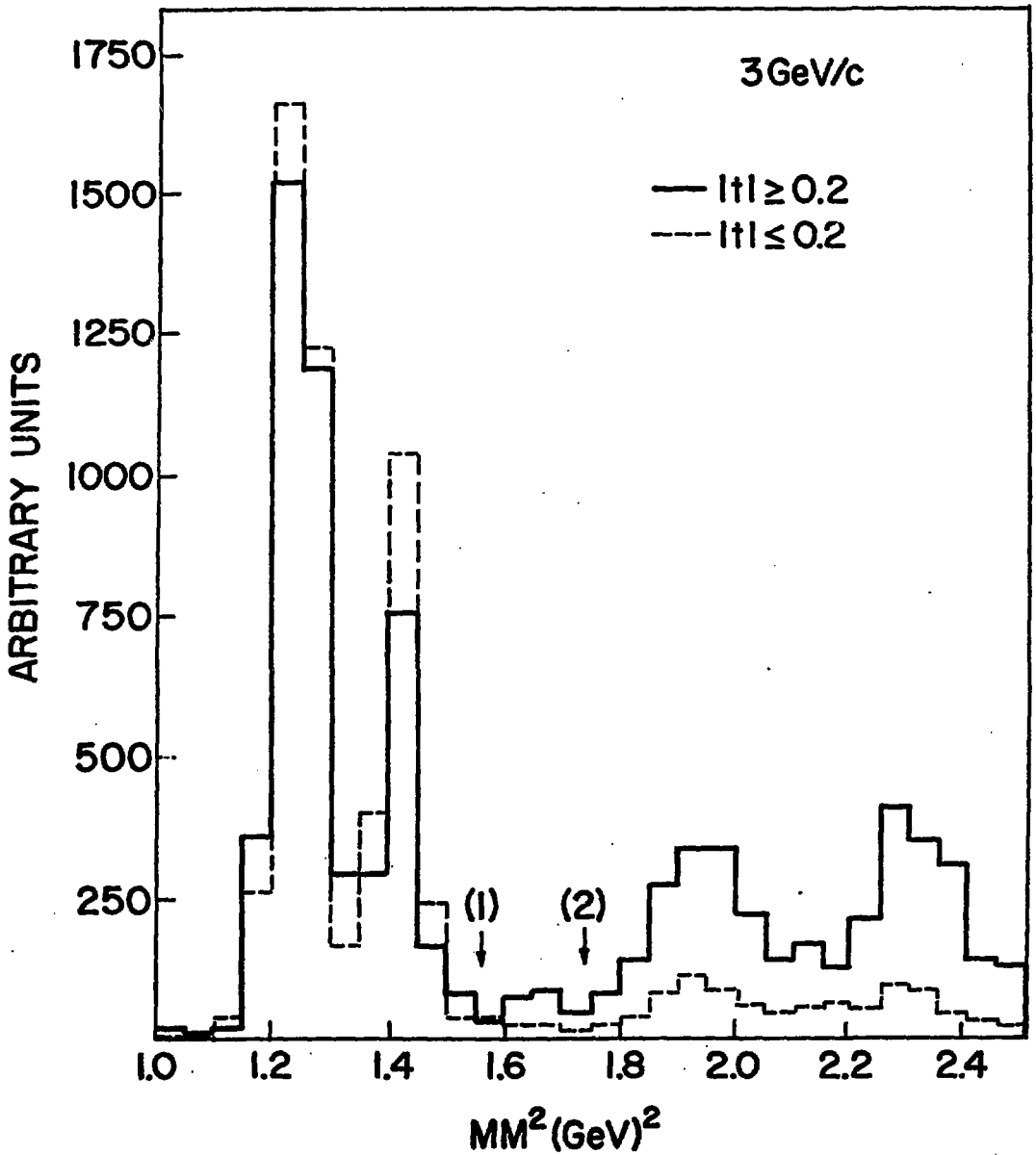

Fig. 22.

Fig. 22.--t-dependence studies of background. K^{o} missing mass for t above and below $|t| = .2$, 3 GeV/c

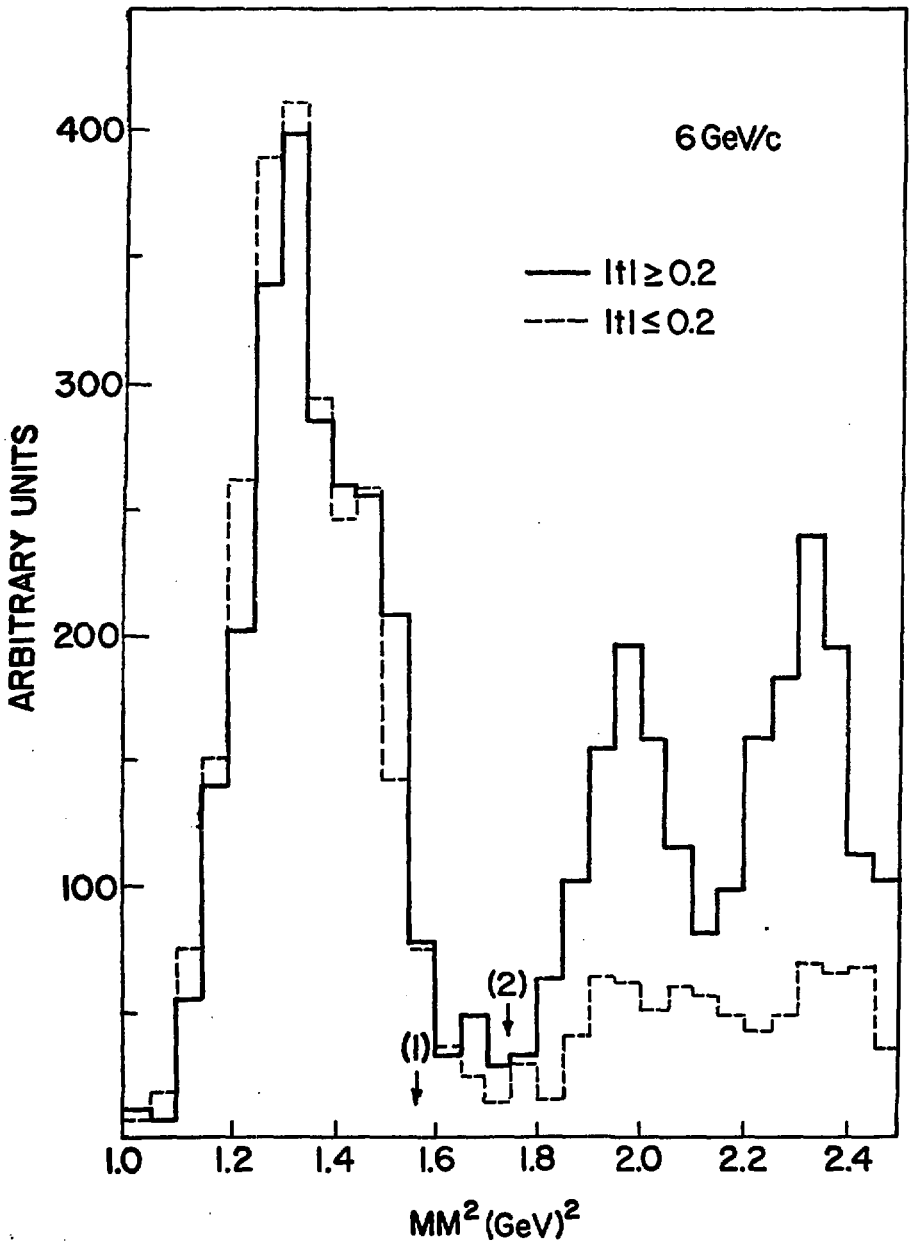

Fig. 23.

Fig. 23.--t-dependence studies at 6 GeV/c

2. Inelastics

Possible sources of the above background events which may mistakenly be included in the data come from reactions such as $\pi^- p \to K^o Y^*$, where the Y^* mass is close to the mass of the Σ^o, or from reactions like $\pi^- p \to K^o \Lambda^o \pi^o$ or $\pi^- p \to K^o \Sigma^o \pi^o$ where the $\Lambda^o \pi^o$ ($\Sigma^o \pi^o$) are uncorrelated.

The Y^* resonances have intrinsic mass widths in addition to a mass width due to the experimental mass resolution. Figure 22 shows the enhancements at the $\Sigma(1385)$, $\Lambda(1405)$ masses, and also at the $\Lambda(1520)$ mass, so clearly these reactions are present in our data. Such events, in the tail of the $\Sigma(1385)$ - $\Lambda(1405)$ peak especially, may be included within the cut on the Σ^o missing mass. Uncorrelated $\Lambda^o \pi^o$ and $\Sigma^o \pi^o$ events have K^o missing mass distributions which start at 1.57 and 1.74 GeV^2, respectively, shown by the two arrows in Figure 22. The experimental resolution smears these values, so that it is also possible for these events to appear at lower missing masses and within the cuts. We estimate the shape of the missing mass distributions for these events by using the data. With our good estimate of the experimental resolution, we can draw in the tail from the Σ^o missing mass peak. Extrapolating by eye, we also draw in the tail from the Y^* peak. The difference between these curves gives the contribution from the $\Lambda^o \pi^o$ and $\Sigma^o \pi^o$ events. Figure 24 (a) and (b) shows the three curves. Finally, using Figure 24, we obtain the following correction factors due to background contamination in the missing mass: .01% at 3 GeV/c, and .3% at 6 GeV/c.

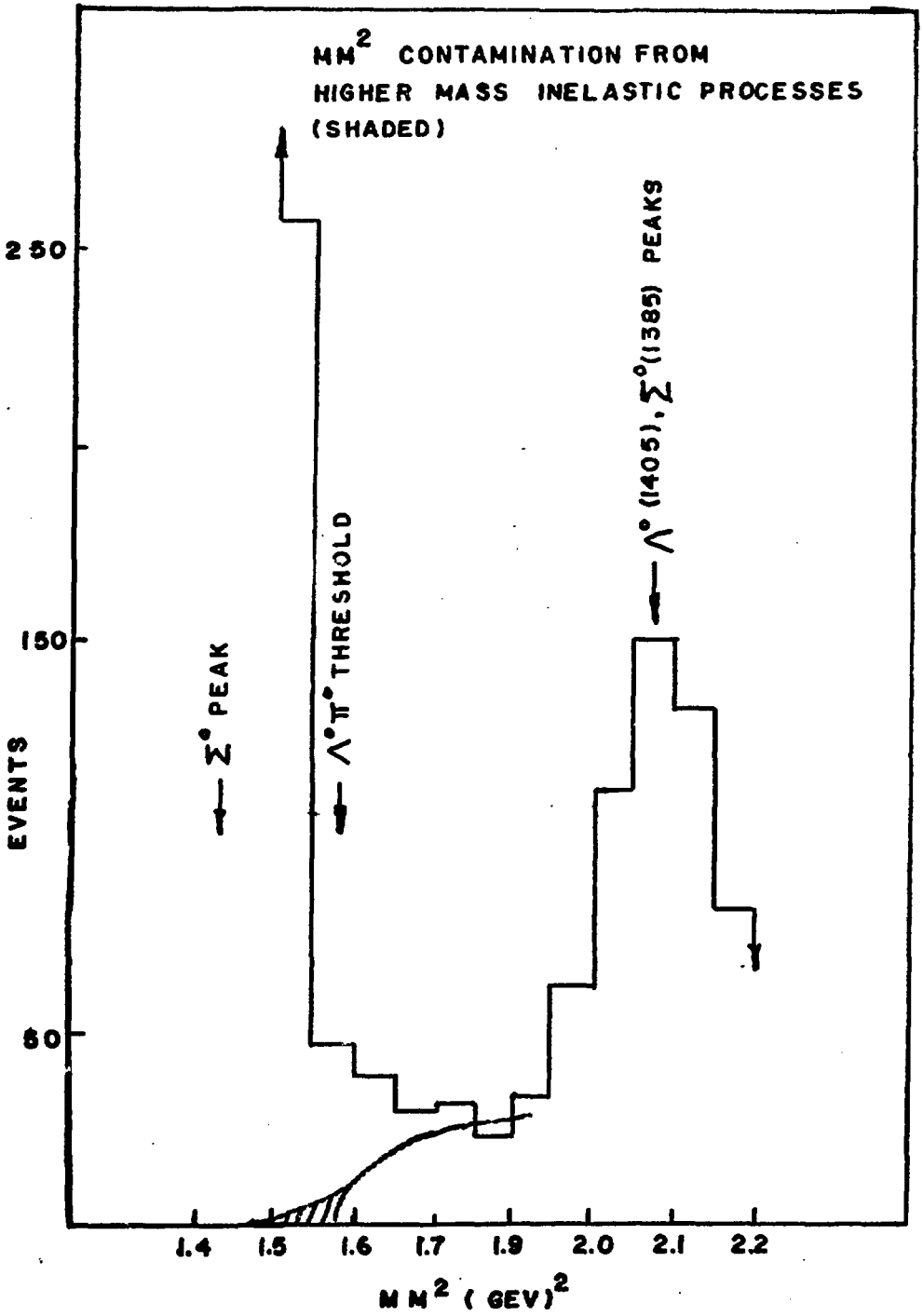

Fig. 24.

Fig. 24.--Study of Contamination from Higher Missing Mass Reactions.

This essentially completes the subject of corrections determined from the data. For reasons of continuity and clarity, however, we have allowed some overlap between this subject and other discussions, e.g., in the section on resolution, Chapter II, and on corrections independent of the data. Before getting on to discussing the latter more fully, we mention briefly a feature of the raw data which posed an interesting puzzle.

E. Hypothesis Failures

We found a component in our data consisting of tracks passing all the geometric and momentum analysis tests, but which were not identifiable as K^o's or Λ^o's. This is a consequence of the fact that we did not attempt to search for more than five possible kinematic hypotheses. We were, however, able to isolate out e^+e^- pairs in these hypothesis failures as follows:

Figure 25 shows the e^+e^- effective mass distribution for a sample of events which fit no hypothesis. We compare this with Figure 16(a), previously identified to be due to e^+e^- pairs, and conclude that indeed a large fraction of the non-fitting events are e^+e^- pairs. At 3 GeV/c, $\sim$27% of the non-fitting events are pairs. As a further check, we find the point of origin of the pairs by calculating the intersection point of the two tracks. Figure 26 shows this vertex distribution along the beam axis, for the "pair" events. Clearly, most of the pairs are produced in the CM counter; the ratio of events originating inside the CM counter to those originating in air is 5.5±.8. We expect this ratio to be 5.2, by comparing the mass of 21" of air with

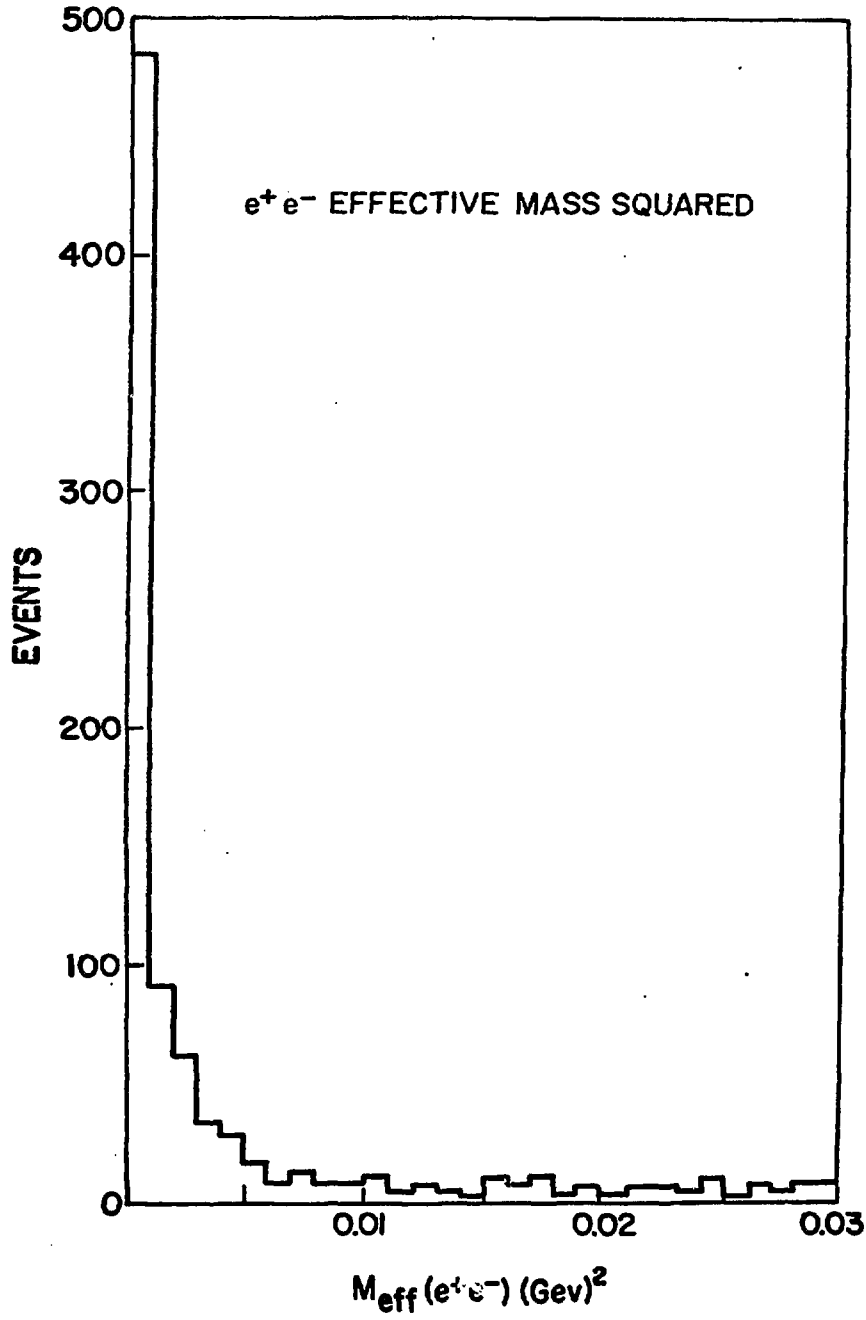

Fig. 25.--Hypothesis failure studies: e^+e^- effective mass for events not fitting K^o, Λ^o hypothesis

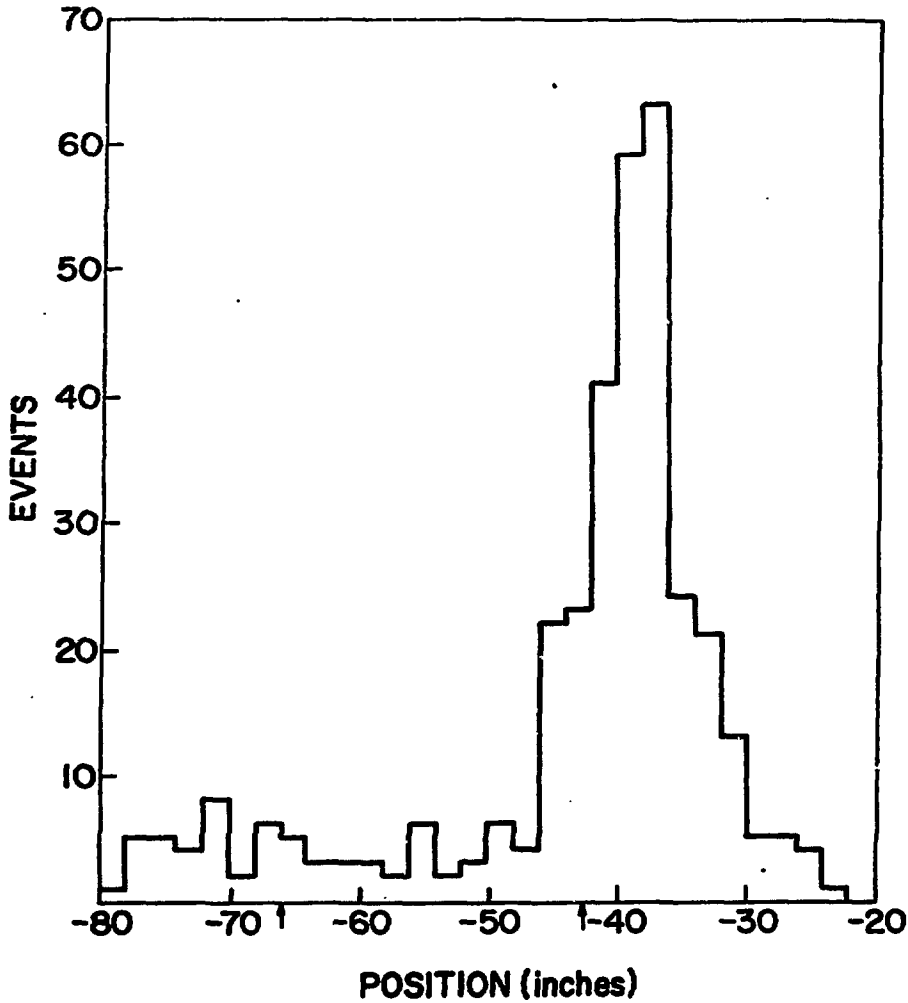

Fig. 26.

Fig. 26.--Vertex Distribution Along the Beam Axis for the e^+e^- Events, Identified by their Low Effective Mass in Figure 25. The Left and Right Arrows on the Abscissa Mark the Locations of the Veto Counters and CM Counter, Respectively. The Preponderance of Pairs are Produced in the CM Counter, as Expected.

that of 1/8" of scintillator--in good agreement with our result.

We can think of the remaining ∿23% of the analyzed events which do not fit the hypothesis of being K^o's, Λ^o's, or e^+e^- pairs, as events which "fail" the kinematic requirements. As was done previously for other failure categories, we want to determine the extent to which these events are legitimate failures so as to insure that there is no systematic loss or uncorrected inefficiency at this point.

In plots of effective mass (Figure 4) it is clear that there is very little background in the K^o effective mass peaks, at all incident momenta. The applied cuts are generous, and in addition, a 2-C fit to the K^o effective mass and to the Λ^o (or Σ^o) missing mass further cleanses these peaks of background contamination. The non-fitting events (with identified e^+e^- pairs subtracted) have effective masses well outside the cuts used to select K^o's. No doubt a fraction of these events are $K^o \to \pi^+\pi^-$ where one of the pions has decayed before the K1 chamber. Such tracks would have no problem in any of the reconstruction routines, but would show up as not fitting any kinematic hypothesis. The corrections we apply for decays already account for such events. We conclude that no correction need be applied to the data due to these non-fitting events and that they are "legitimate kinematic" failures.

III. Corrections Independent of Data

We now turn to the corrections obtained independent of the data. We will discuss first the geometrical acceptance of the

spectrometer, which was obtained by means of a Monte Carlo calculation.

A. Acceptance

In pseudoscalar meson-baryon scattering, an event is completely characterized by a number of parameters, where only two of these, s and t, are relevant to the dynamics. We find the probability that an event will be detected in the apparatus by picking values for s and t, and then averaging over all other quantities which specify the event. Using a computer, we generate many events at given s and t and choose the other parameters randomly within several distributions which we will describe. The acceptance at each s and t is then obtained by dividing the number of events which would have been detected within the physical boundaries of the apparatus, by the total number of events generated. We now give a table listing the kind of quantities that were averaged over (K), how many numbers were needed to specify each quantity (N), and the distributions from which these numbers were randomly chosen (D).

K	N	D
1. Incident beam angle.	2	A gaussian, with width 10 milliradians.
2. Production point.	3	Uniform within an 8" long, 2" diameter cylinder.
3. Azymuthal angle of the production plane.	1	Uniform from 0 to 2π radians.

K	N	D
4. Decay point of the K^o and the recoiling Λ^o.	1(1)	Exponential, using the known lifetime of the K^o (Λ^o).
5. Decay angles about the K^o (Λ^o) c.m. directions.	2(2)	Uniform from 0 to 2π radians. (Probability of proton decaying at θ from Λ^o direction: $N(\theta) = 1+\alpha P\cos\theta$; P measured polarization.)

The above distributions were taken to correspond closely with those observed in the data. For example, the width of the distribution in incident beam angle was taken from the observed angles, as measured in the spark chambers K0 (Figure 3). In using an isotropic c.m. decay angle distribution for $K^o_s \to \pi^+\pi^-$ we are following the known properties for this decay. For the $\Lambda^o \to p\pi^-$ decay, the Monte Carlo calculation used the measured polarization of the Λ^o (Chapter IV) and the known angular distribution of the proton about the Λ^o spin in the Λ^o center of mass.

Before showing some typical acceptance curves we will point out some major ingredients and problems in the calculation. The extent to which the decay products of the K^o fall within the physical boundaries of the apparatus determines the acceptance function in large part. There is an additional contribution, however, due to the decay products of the Λ^o (or Σ^o) particle, which must be carefully considered. This arises from the requirement that no

charged particle in a successful event may pass through the 5" x 10" x 1/8" veto counter (VC). This requirement is satisfied by those Monte Carlo events having the K^o's decaying downstream of VC, and having Λ decay products which do not intercept the veto counter.

The proton from the $\Lambda^o \to p\pi^-$ decay tends to follow the direction of the Λ^o in the laboratory. At small t this direction is almost directly forward, so that there is a high chance that the proton will strike the veto counters. Figure 27 shows the detection efficiency (independent of what happens in the K^o branch) for the Λ^o decay as a function of t. The sharp dip in this efficiency at small t is due to the proton intersecting the veto counters. If we now take into account the effect of the liquid hydrogen and of the walls of the target vessel and its wrapping in stopping the protons by energy loss due to ionization, we notice a significant change. The momentum distribution of protons from Λ^o decay at, for example, 4 GeV/c is maximum at $\sim$420 Mev/c. An average of .04 gm/cm^2 of hydrogen or other materials must be traversed by these protons. Except for the high end of the momentum spectrum, the result is that most of the protons are stopped. Figure 27 shows the Λ^o efficiency, with this ranging taken into account. The pion contributes to this efficiency also. However, the pion is not as constrained by kinematics as the proton, and can decay at almost any lab angle. This results in a relatively t-independent contribution to the efficiency. A typical result for the overall Monte Carlo acceptance is shown in Figure 28.

For proper normalization, we used identical criteria to

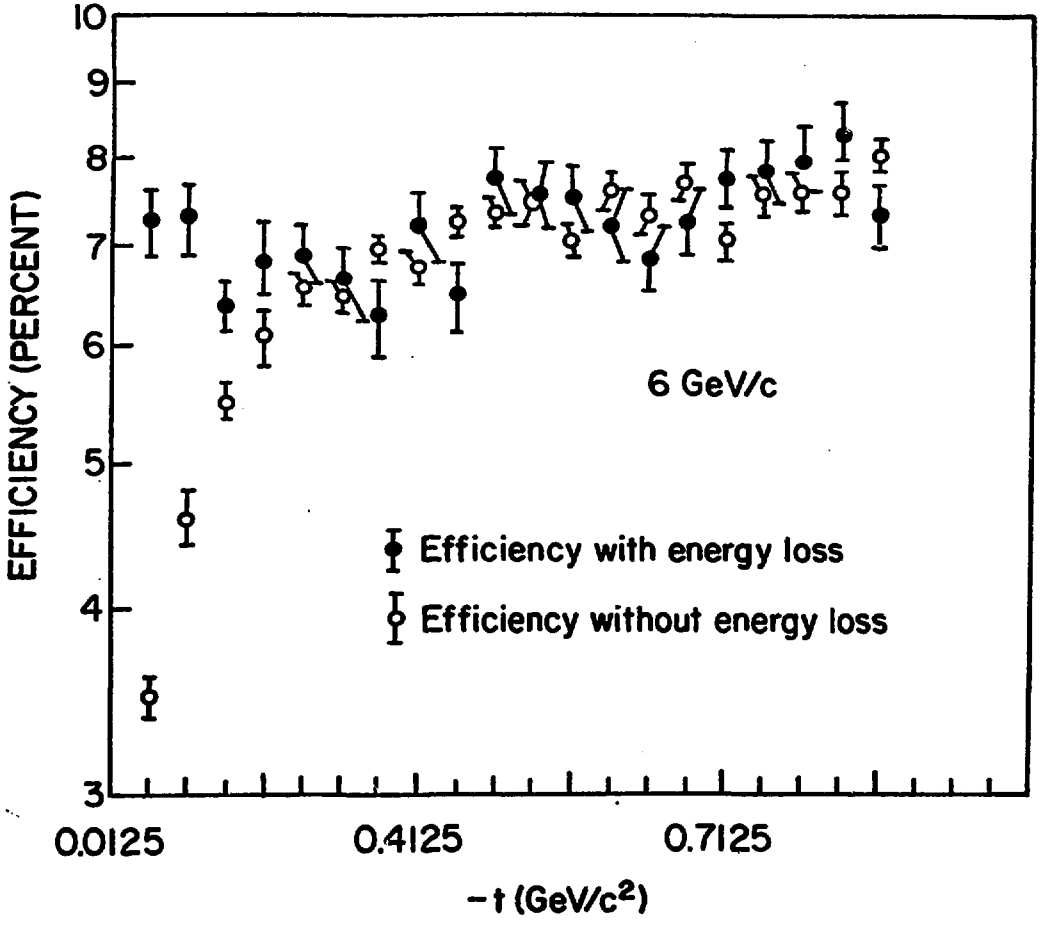

Fig. 27.

Fig. 27.--Detection efficiency due to Λ^0 decay in $\pi^- p \to K^0 \Lambda^0$, effect of energy loss

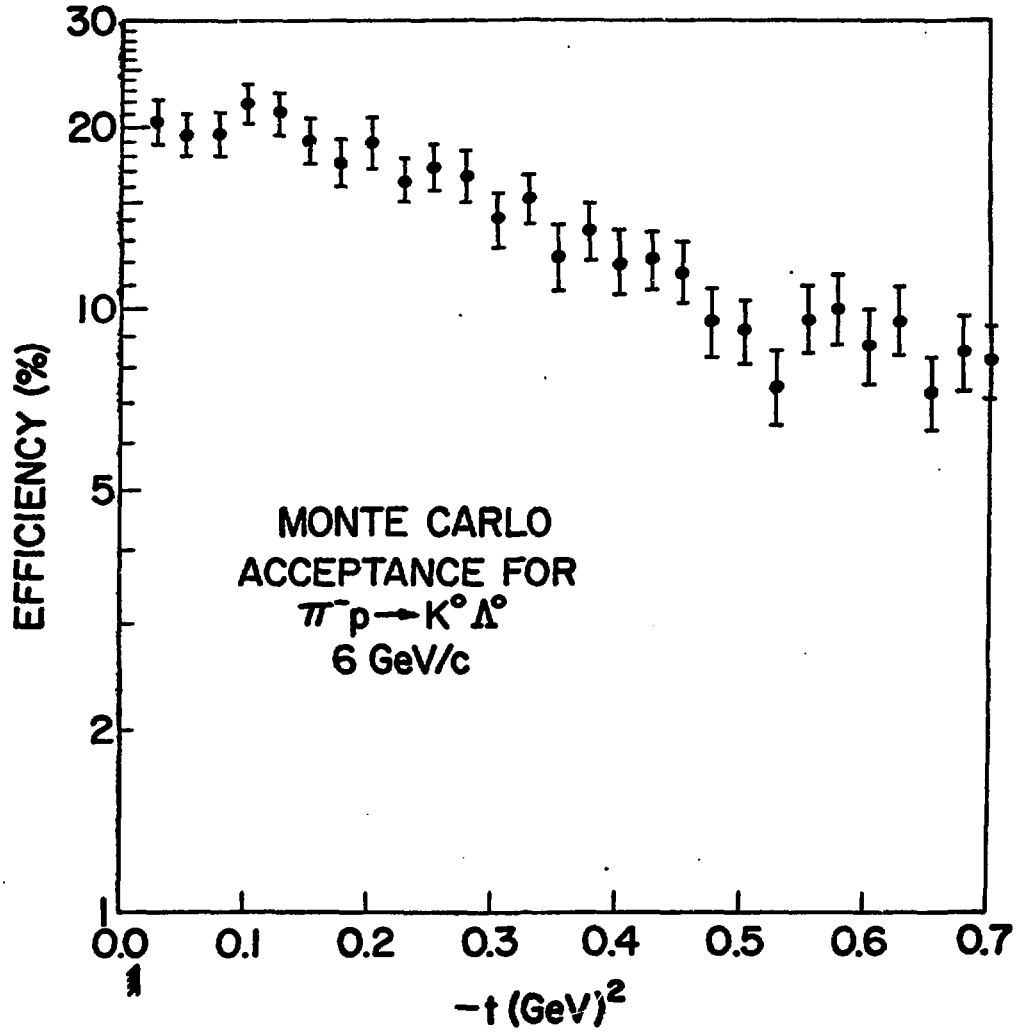

Fig. 28.

Fig. 28.--Monte Carlo acceptance

select "successful" events in the data and in the Monte Carlo calculation. This included cuts on the angle and position of particles in the spectrometer, vertex positions for the vee particles and other cuts. The same criteria were also applied to the target empty data, so that this subtraction correction was also properly normalized. In addition, wherever possible we used the identical routines to operate on data events as on Monte Carlo events. Examples of this were in the fringe field correction applied to tracks, and also in the routine which tracked particles through the magnet.

B. Double Counting; Decays and Absorption

We next describe other corrections obtained "independent" of the data. A difficult task in making corrections to the data was to guard against correcting for the same effect in several places. For example, a straighforward application of the corrections due to strong interactions of pions in the material of the spectrometer, or due to the decay of pions in flight, would make the assumption that all events in which pions interact or decay are in fact absent from the data. This of course is not true as has already been mentioned, because the analysis routines use finite tolerances in selecting and calculating on events. As a result some fraction of the interactions and decays will be analyzed as good events. We determine this fraction by applying the analysis routines to Monte Carlo generated events.

For pion decays, we obtain the result that about 1/3 of the pions decaying to μ's appear as perfectly good events in the

data. This fraction is found to be independent of the incident beam momentum. This can be understood as a geometric effect--decays which occur upstream of the analyzing magnet or inside the magnet will fail the event because the decay μ's, since they have lower momenta than the pions, will be considerably bent by the magnetic field. Their tracks will have kinks to which the reconstruction routines are sensitive. On the other hand, the muons decaying from pions downstream of the magnet are much less severely affected by the magnetic field, and less easily distinguished as decays in the programs.

A rough calculation bears out this interpretation. We take a typical pion momentum of ∿2 GeV/c and consider the longitudinal laboratory momentum (along the direction of the π) of the decay muon. For decays which occur upstream of the magnet, tracks differing in momentum by ∿3% are bent by the field through angles which also differ by ∿3%. For the typical bend angles of ∿270 mr, this amounts to an ∿9 mr difference between the bend angle of a non-decaying pion and that of a decay muon with momentum differing by ∿3% from the pion. When we include the additional angle difference due to the decay alone, we estimate that two such tracks would strike a spark chamber downstream of the magnet at points separated by nearly an inch. Such differences are easily distinguished by the programs. Most decay muons have longitudinal momentum differing from the pion momentum by more than 3%; the muon momentum as a function of the c.m. decay angle is $p_\mu = A \cos\theta + B$, where A = .429 GeV/c and B = 1.569 GeV/c (for 2 GeV/c pions). Hence, decays that occur upstream of the magnet can be

distinguished from non-decaying pions. For the pion decays downstream of the magnet, the angle difference between the tracks is due to the decay alone, with no additional effect due to the magnetic field. For the maximum c.m. muon decay angle, there is a laboratory angle difference of $\sim$15 mr between the muon and the pion tracks, corresponding to a .2" difference in the coordinate of a μ and that of a non-decaying pion, as measured by the spark chambers. Most decays occur at angles less than this maximum and hence will not be distinguishable as decays. We use the Monte Carlo result that $\sim$1/3 of the $\pi \to \mu \nu$ decays which take place are undetected as such, and included as good events in the data. This factor does not depend on momentum of the pions, but rather only on the distribution of decay points in the spectrometer.

The calculated correction for the decay of pions in the spectrometer was obtained using the known pion lifetime, and by averaging over the pion momenta at each incident beam momentum value. Other corrections that were obtained independent of the data were due to absorption of the beam in the hydrogen target, absorption of K's in the target and its walls and absorption of the decay pions in the material of the spectrometer. A complete accounting of these corrections, along with their uncertainties, is given in Table 5. The overall normalization uncertainty, obtained by adding the uncertainties in Table 5 in quadrature is $\sim$ 3%. Not all of these errors are independent, however; we estimate that a more realistic value for the normalization uncertainty is $\pm$10%.

TABLE 5

OVERALL CORRECTION FACTORS

Factor	3 GeV/c	4 GeV/c	5 GeV/c	6 GeV/c
a	0.966±0.007	0.948±0.005	0.956±0.005	0.938±0.004
b	0.998±0.0011	0.997±0.001	0.996±0.001	0.994±0.001
c	0.980±0.010	0.985±0.007	0.986±0.007	0.984±0.008
d	0.949± -	0.962± -	0.963± -	0.964± -
e	0.950±0.01	0.966±0.007	0.976±0.005	0.987±0.003
f	0.977±0.01	0.977±0.01	0.977±0.01	0.977±0.01
g	0.981±0.002	0.981±0.002	0.981±0.002	0.981±0.002
h	0.982±0.005	0.983±0.005	0.978±0.005	0.983±0.005
i	0.982±0.002	0.982±0.002	0.981±0.002	0.981±0.002
j	0.956±0.004	0.956±0.004	0.956±0.004	0.956±0.004
k	0.932±0.007	0.949±0.005	0.960±0.004	0.967±0.003
l	0.976±0.01	0.978±0.01	0.978±0.01	0.979±0.01
m	0.751±0.003	0.781±0.003	0.825±0.003	0.811±0.003
n	0.950±0.03	0.950±0.03	0.950±0.03	0.950±0.03
o	0.996± -	0.999± -	0.999± -	0.998± -
Overall	1.823±0.070	1.637±0.059	1.533±0.055	1.488±0.05
Quad. Sum	3.9% 10.3%	3.6% 9.3%	3.6% 9.9%	3.4% 8.5%

Key to Correction Factors

a = target empty

b = kinematic ambiguity

c = dead time

d = accidental vetos

e = decay of beam π

f = "slow" beam particle

g = strong alternation of K^o

h = trigger hodoscope ineff.

i = scattering of spectrometer π

j = interactions of spectrometer π

k = decay of spectrometer π

l = delta rays

m = logic config. and beam chr.

n = computer programs

o = tape reading losses

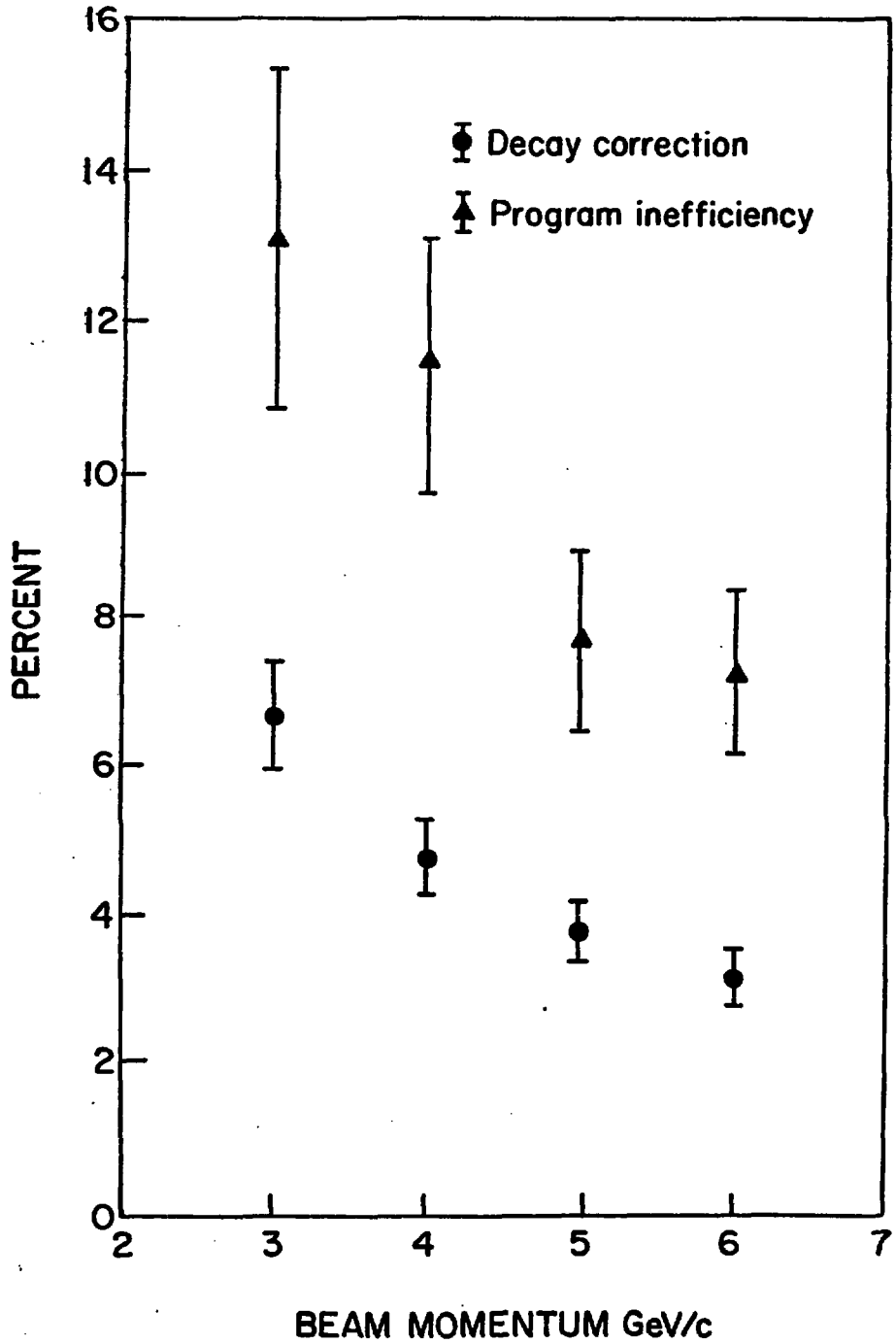

Fig. 29.

Fig. 29.--Decay correction vs. program inefficiencies

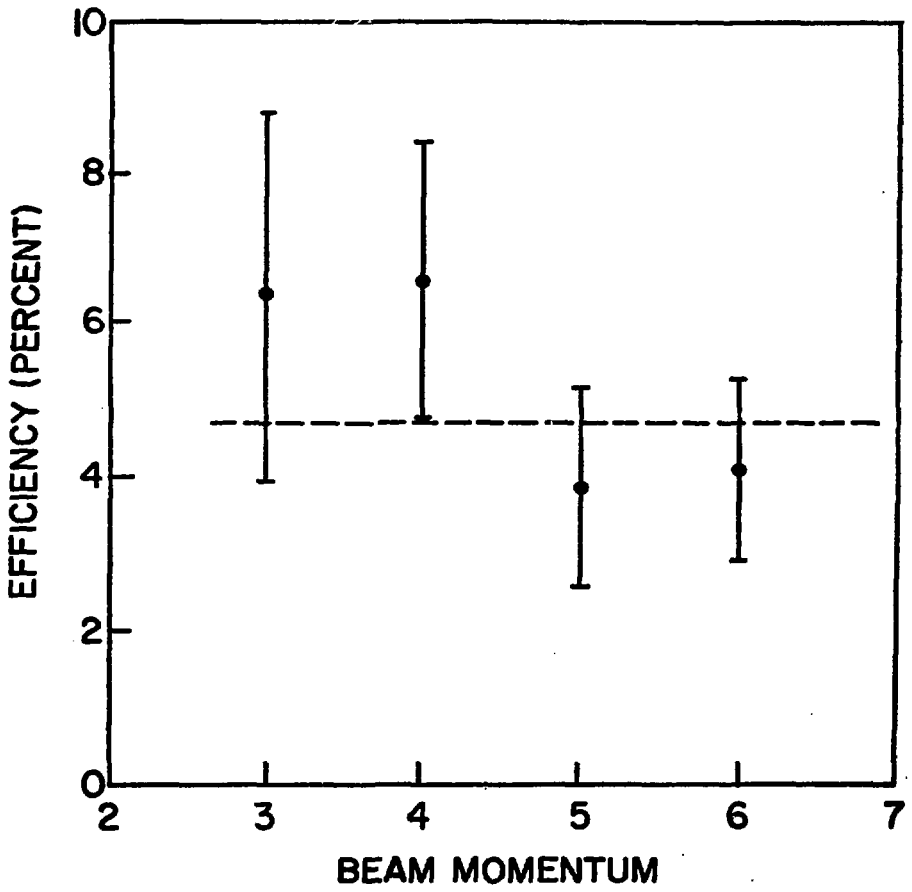

Fig. 30.

Fig. 30.--Final program corrections

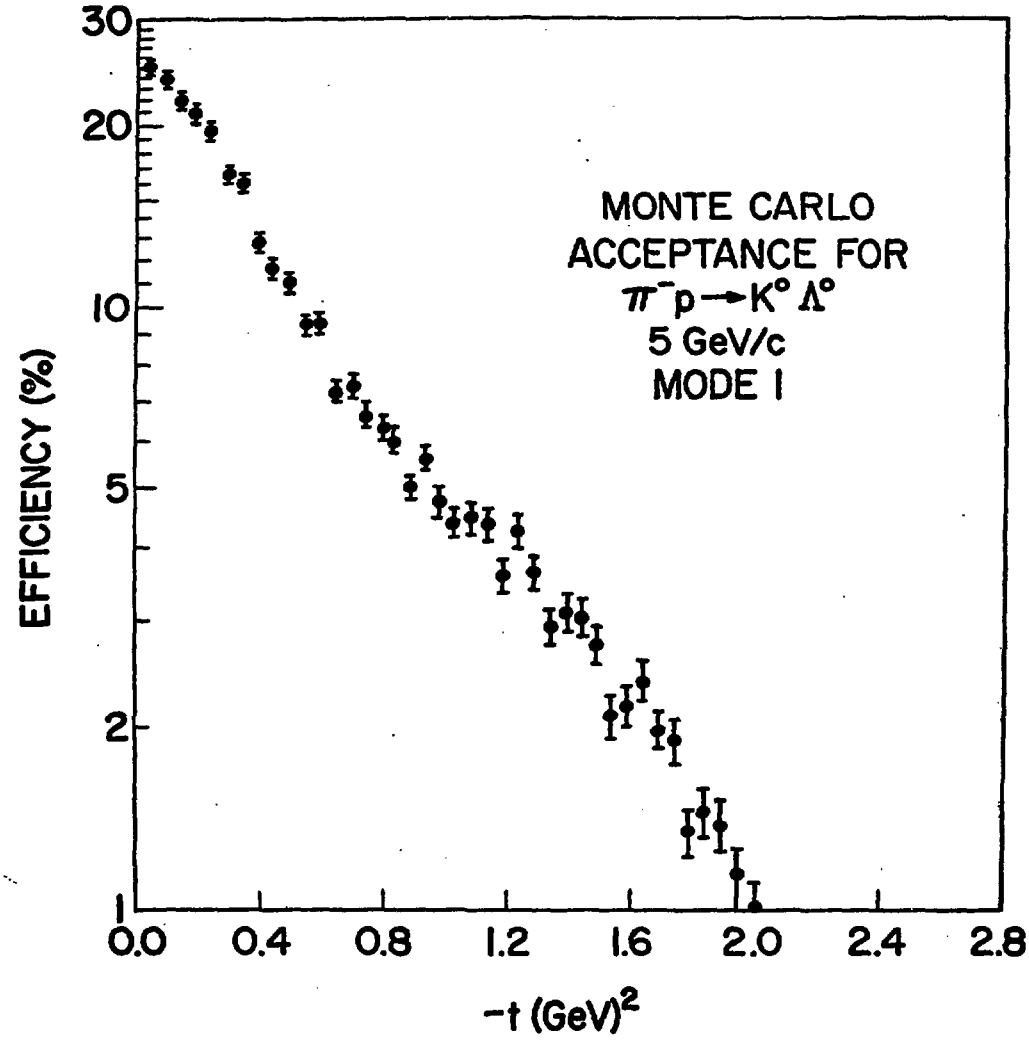

Fig. 31.

Fig. 31.--Mode 1 Acceptance

We briefly mention here a final instance where we explicitly avoided double counting in the analysis. The correction for pion decay in flight depends on incident beam momentum, since the average momentum of the decay pions increases as the incident beam momentum increases. Figure 29 shows the calculated correction factor as a function of incident beam momentum. The correction due to the geometric reconstruction program inefficiency (obtained by scanning -- Section B) is also shown in Figure 29. Some of the events which had the good vee particle spark pattern, but whose tracks failed to be reconstructed, failed because a decay took place (between K1 and K5 only) spoiling the track. The $\pi \to \mu \nu$ decays cannot be distinguished by eye.

In the scanning procedure, we have over-corrected for such events. We obtain the final value for the reconstruction in efficiency by subtracting the calculated decay probability from this correction, (Figure 30) and by averaging over the beam momenta. This results in the correction factor for reconstruction program inefficiency given in Table 5.

C. Consistency Checks

We made checks at several stages in the analysis for overall consistency. To avoid biases in the scanning, for example, the independent work of several physicists was compared and required to agree to within the statistical errors. A total of over 3000 events were scanned, covering all the failure categories previously discussed. To insure the correctness of the rather complicated Monte Carlo program, two separate and independent calculations

were done by two workers. Subsequent comparisons at different stages of the calculation were often found to be useful in the elimination of errors. An additional check was also possible since we measured the same reactions in two different experimental running modes. We calculated the cross sections in each mode separately, applying corrections to the data that were appropriate to each mode, and then compared the results, which should agree.

The data which was collected in the measurement of Λ^o polarization (Chapter IV) in $\pi^- p \to K^o \Lambda^o$, could of course also be used to measure $\frac{d\sigma}{dt}$. The aim in Mode 3 was to trigger on events likely to have particle tracks in the Λ^o chamber (beam's right) (Figure 3). Accordingly we desensitized the right half of the counter hodoscope to prevent triggering on events with final state charged particles passing to the right of the beam line, and we removed the veto counter to the right of the beam to allow Λ^o decay products to enter the recoil chambers without vetoing the event.

The largest difference in the corrections that were applied to data taken in the two running modes was in the acceptance calculation as a function of t. Figures 31 and 32 show the acceptance for Mode 1 and Mode 3. One might expect that the two curves would differ only in a scale factor, since at first glance the difference between the two modes is only in their fiducial volume. When we scale up the Mode 3 acceptance curve by a factor of 1.7 (Figure 33), it does seem to agree with the Mode 1 acceptance for $t \geq .4$. We expect this to be true at the higher t values

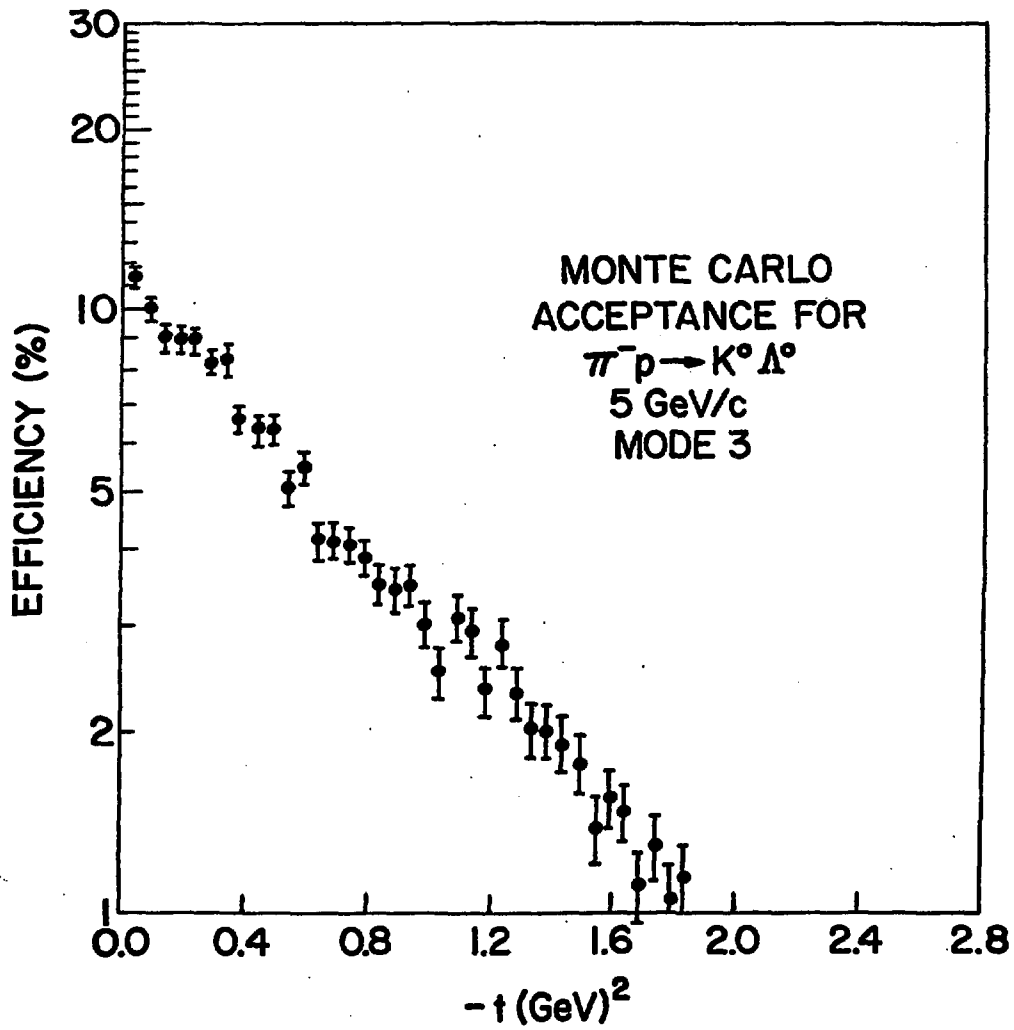

Fig. 32.

Fig. 32.--Mode 3 Acceptance

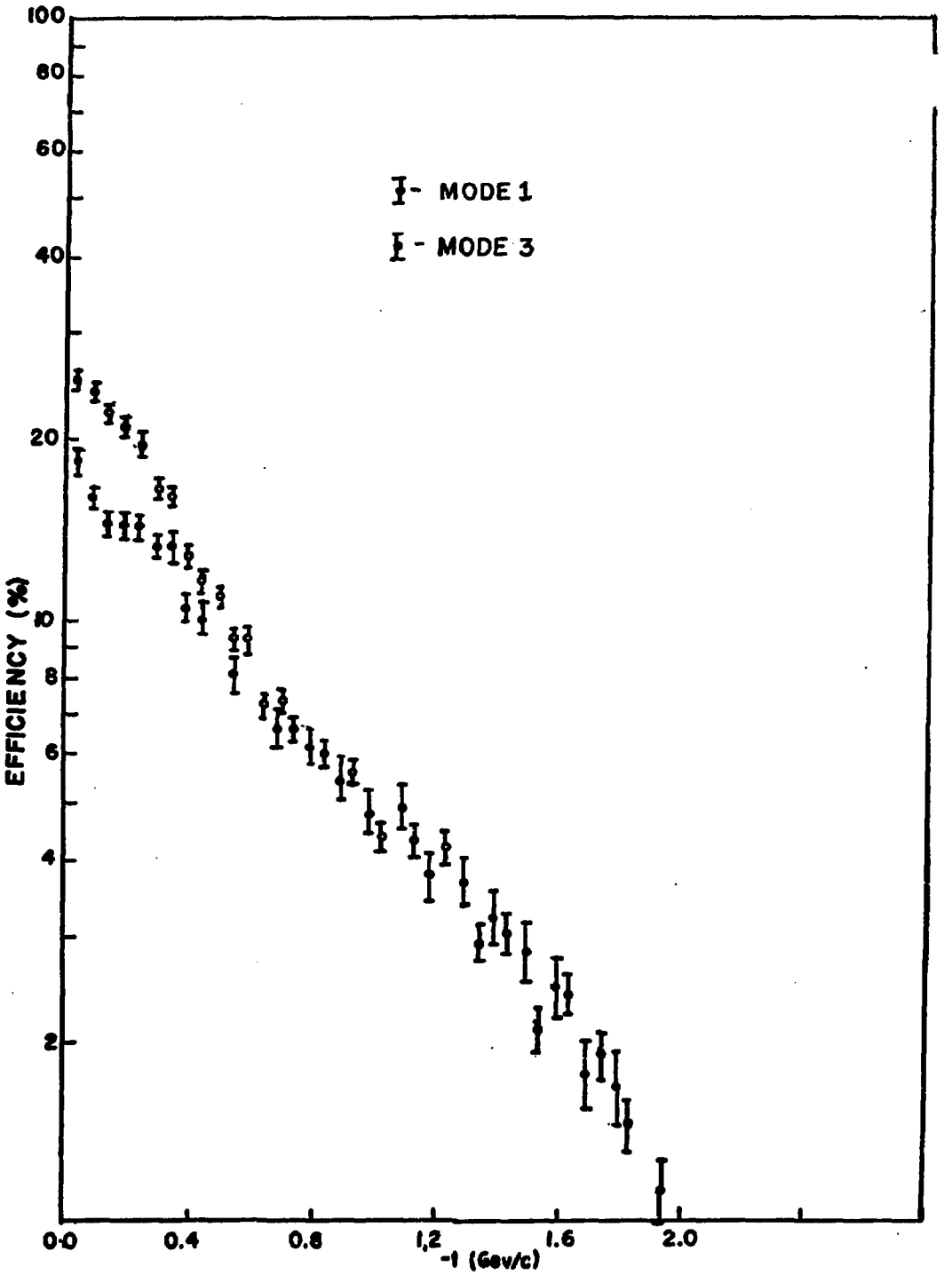

Fig. 33.

Fig. 33.--The Acceptances for Mode 1 and Mode 3 Normalized so as to Agree at Large $|t|$ Values (i. e. $|t|>0.4$)

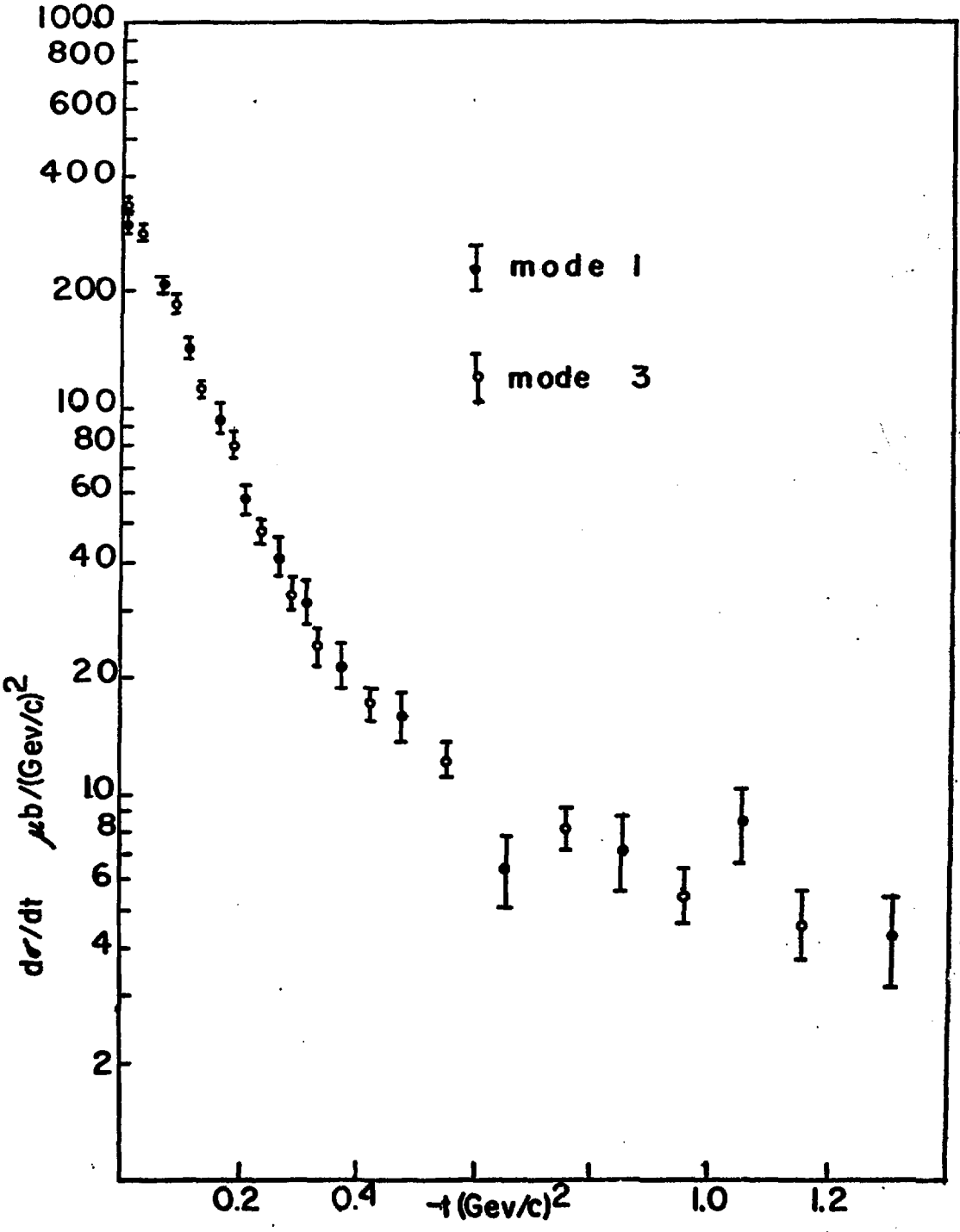

Fig. 34.

Fig. 34.--Comparison of $d\sigma/dt$ Data for $\pi^- p \to K^\circ \Lambda^\circ$, for Running Mode 1 and for Mode 3, which Tests the Overall Consistency of the Applied Corrections.

because these events have the K^o produced at sizable lab angles, so that the decay pions are likely to both go either through the right or left half of the trigger hodoscope. More than just a scale factor accounts for the difference between the Mode 1 and Mode 3 acceptance, however, because the Mode 3 acceptance is extremely sensitive to spatial correlations between the K^o decay pions, whereas the Mode 1 acceptance is not. The difference between the two at smaller t is due to the effect of at least one decay pion going through the right half of the hodoscope in the Mode 1 trigger. This occurs more frequently for the small t than the large t events, as is reflected in the curves in Figure 33. The comparison of $\frac{d\sigma}{dt}$ in these two modes is a valuable check to have, since the corrections are different for the two cases, yet the $\frac{d\sigma}{dt}$ must be the same. Figure 34 shows the comparison of $\frac{d\sigma}{dt}$ as obtained from the Mode 3 and Mode 1 running modes. We believe that the agreement, within the overall errors, is reasonable.

Finally, the reaction $K^-p \to \bar{K}^o n$, also studied with the same apparatus (in fact concurrently with the $\pi^-p \to K^o\Lambda/\Sigma$), provides a third albeit statistically weaker consistency check. Namely, in this reaction only the $\bar{K}^o \to \pi^+\pi^-$ acceptance applies without constrains of hyperon decays. Good agreement was found with other K charge exchange data independently for both triggering modes.

CHAPTER IV

POLARIZATION MEASUREMENT AND ERROR ANALYSIS

I. Introduction

Previously, we have been concentrating primarily on the K^o's in the reaction $\pi^- p \to K^o \Lambda^o / K^o \Sigma^o$. We will now consider the recoiling hyperon. The produced Λ^o has mainly two decay modes, $p\pi^-$ and $n\pi^o$. We are able to detect only the charged mode, constituting 64.5% of the total. The Λ^o's decay by weak interaction, with parity-violation, with the consequence that the directions of the decay particles are correlated with the polarization of the Λ^o particle. Hence, we can measure the polarization of the produced Λ^o by observing the decay. Our results are shown in Figure 45 and Table 7. For the measurement of the decay we do no momentum analysis of the Λ^o decay products (except for a subsample of events having both p and π^- detected), but use other kinematic constraints to identify the decay particles. Specifically, we use the fact that in the laboratory the protons emerge in a cone of angles about the Λ^o direction, the size of the cone angle depending on the Λ^o momentum. A set of side spark chambers (see Figure 3) measures the direction of the decay proton. For the reaction $\pi^- p \to K^o \Sigma^o$, this simple experimental setup did not provide enough

information for sufficiently precise event identification, and thus polarization was not measured for Σ^o.

A. Calculation of Polarization

Λ^o's produced in $\pi^- p \to K^o \Lambda^o$ may be polarized only along (or opposite) the normal to the scattering plane. The angular distribution of the decay protons in the Λ^o c.m., about the polarization axis is given by,

$$N(\cos\theta) = 1+\alpha P\cos\theta$$

θ -- c.m. decay angle

α - weak decay parameter = 0.645 (IV-1)

P - Polarization

Integrating distriubtion IV-1 over θ we obtain the probability of having a proton above (U) and below (D) the scattering plane:

$$P = \frac{2}{\alpha} \cdot \frac{U-D}{U+D} \qquad \text{(IV-2)}$$

The sign convention used for the polarization is as follows: "up" is defined as the direction of the normal to the scattering plane $\hat{\pi} x \hat{K}^o$; a positively polarized Λ^o decays preferentially with the decay proton "up".

Only events identified as 1) K^o's, 2) having missing mass in the Λ^o region, 3) having a track detected in the Λ^o chambers, and 4) having that track within the allowed Λ^o cone angle, are binned as "up" and "down" events to be used in the measurement of polarization. In addition, for a subsample of the Λ^o decays where both p and π^- are detected in the spark chambers, we were able to do a four-constraint fit to determine the p and π^- momenta. This was used as a consistency check on the alignment

constraints of the Λ^o chambers. (Section III.)

We next discuss the possible sources of error that may contribute in this method of measuring the polarization.

II. Sources of Error

Sources of error may be divided into three major categories: A) There may be bad survey and alignment of the spark chambers (rotation, skewness). B) There may be non-uniform efficiences in the spark chambers. C) There may be errors in the determination of the scattering plane.

A. Survey

The precision in the placement of spark chambers was on the order of $\sim$10 mils, and the alignment of wires with the vertical axis was to within a milliradian. The relative position of the chambers was checked by reconstructing πp elastic scattering events, where the proton was detected in the side chambers. Good agreement was found with the survey constants. Figure 35 shows the deviation of measured from predicted angles for elastic scattering tracks. The peaks at zero indicate correct alignment.

To check for relative rotation or skewness of chambers, we again make use of elastic scattering events. We plot the angular deviation of measured from predicted tracks as a function of position of the tracks in the side chambers. A skewness would be indicated if the peaks shifted systematically as a function of position in the chambers. Figure 36 and 37 show no such indication of skewness.

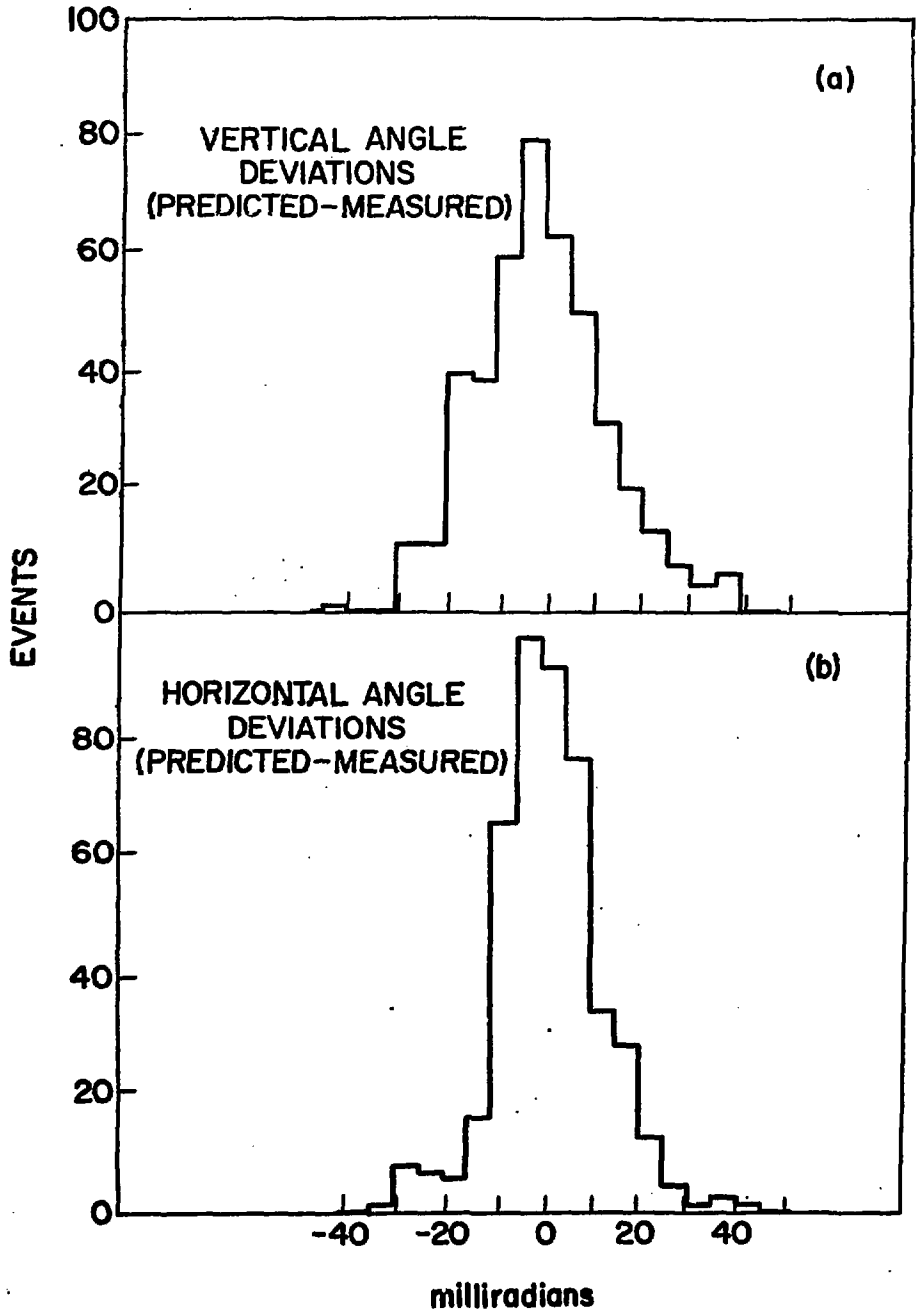

Fig. 35.

Fig. 35.--Angular deviation of elastic scatter tracks, (predicted-measured). (a) Vertical angle; (b) Horizontal angle

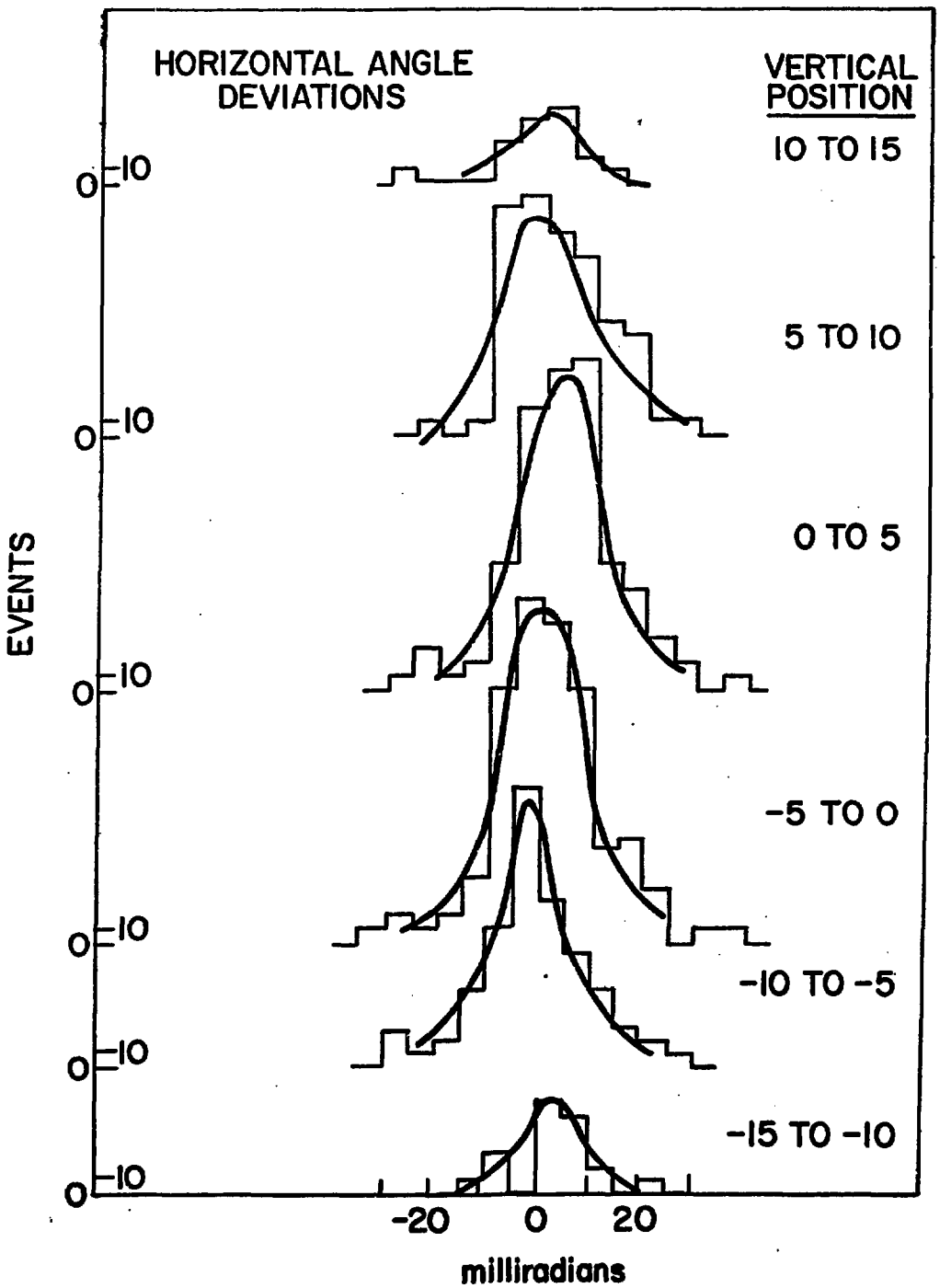

Fig. 36.--Horizontal angular deviations for elastic scattering tracks. The six distributions represent tracks having different ranges of vertical positions at the spark chamber.

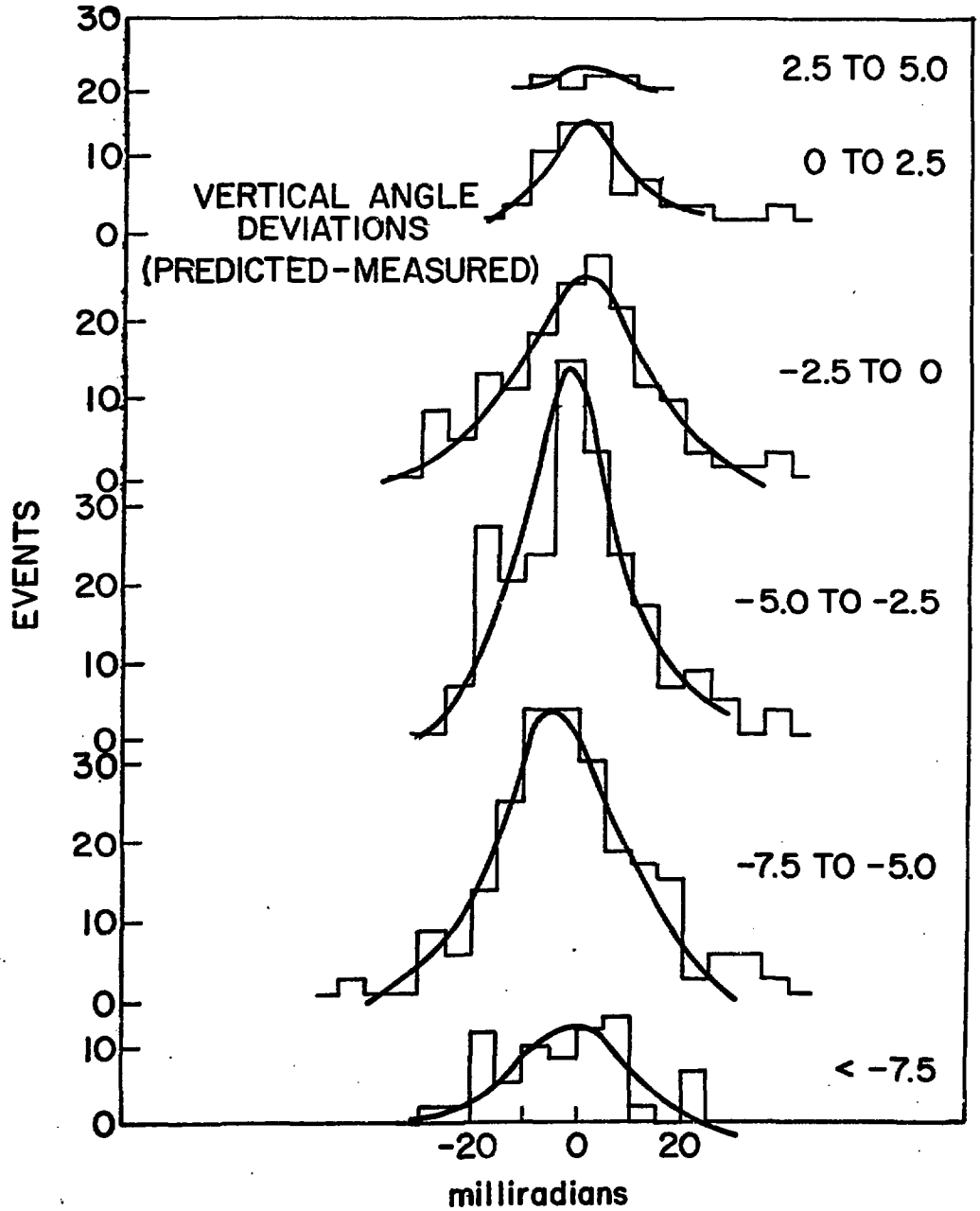

Fig. 37.

Fig. 37.--Vertical angular deviations for elastic scattering tracks. The six distributions represent tracks having different ranges of horizontal positions at the spark chambers.

B. Non-Uniform Efficiencies

This effect, if present, would bias the P measurement since events with the proton "up" or "down" with respect to the scattering plane would be detected with different efficiencies. Figure 38 shows a distribution of events across the area of the chambers (horizontal and vertical). No statistically significant "holes" in these distributions are evident.

C. Scattering Plane Errors

Polarization is calculated, as mentioned, by finding the asymmetry in the number of protons up or down with respect to the scattering plane, with the extra constraint that these protons lie inside the maximum decay cone angle.

If a systematic error placed the "measured" scattering plane consistently higher (or lower) than the "true" scattering plane, the polarization calculation would be affected. We investigate this by plotting the ratio of the measured proton angle to the maximum proton angle, for "up" and "down" events separately. Figure 39 shows distributions of the two ratios for events having $|t|<.25$, and Figure 40 for events having $|t|>.25$. There is no appreciable shift in the position of the "up" peak relative to the "down" peak. Such a relative shift would be caused by an error in the scattering plane determination.

Again elastic scattering events, known to be azymuthally isotropic, were used to check for biases of this and any other kind. This way the apparatus was checked to be free of any effect which would result in spurious polarization.

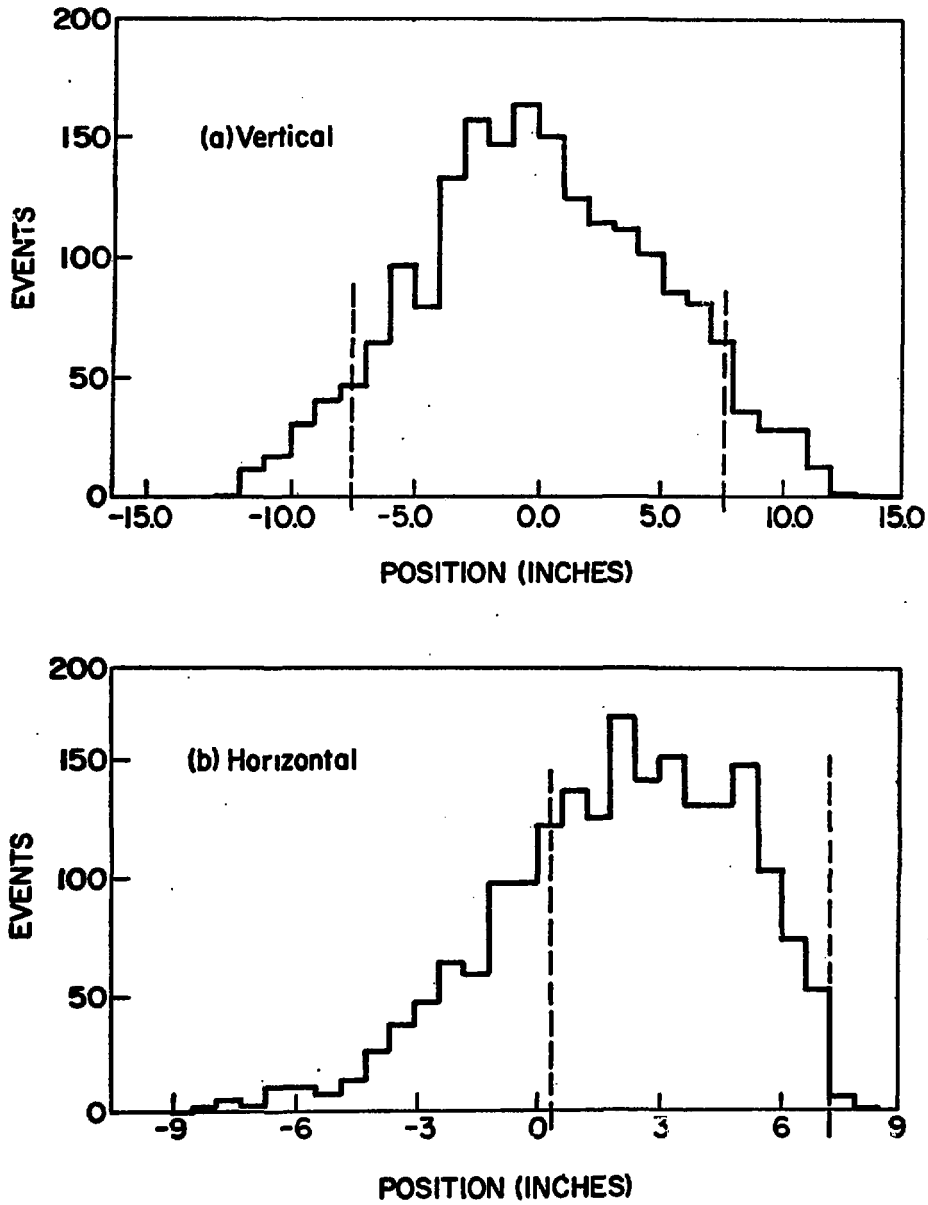

Fig. 38.

Fig. 38.--Frequency of tracks vs. position in the side spark chambers. (a) Vertical positions; (b) Horizontal positions

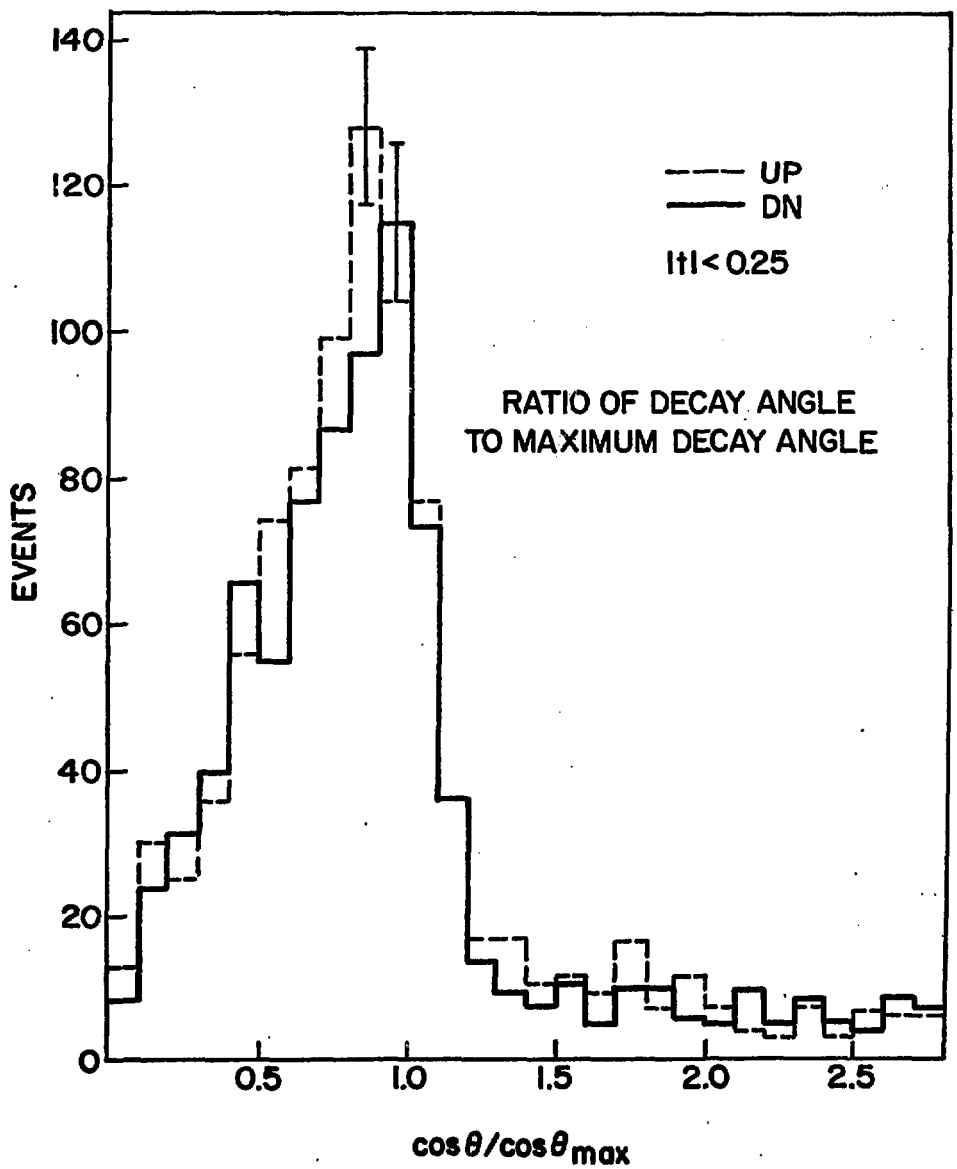

Fig. 39.

Fig. 39.--Events vs. $\frac{\cos\theta}{\cos\theta_{max}}$, where $\cos\theta = \hat{p}_{Lambda} \cdot \hat{p}_{proton}$. Ratio of measured angle to maximum possible laboratory decay angle, for $|t| < .25$

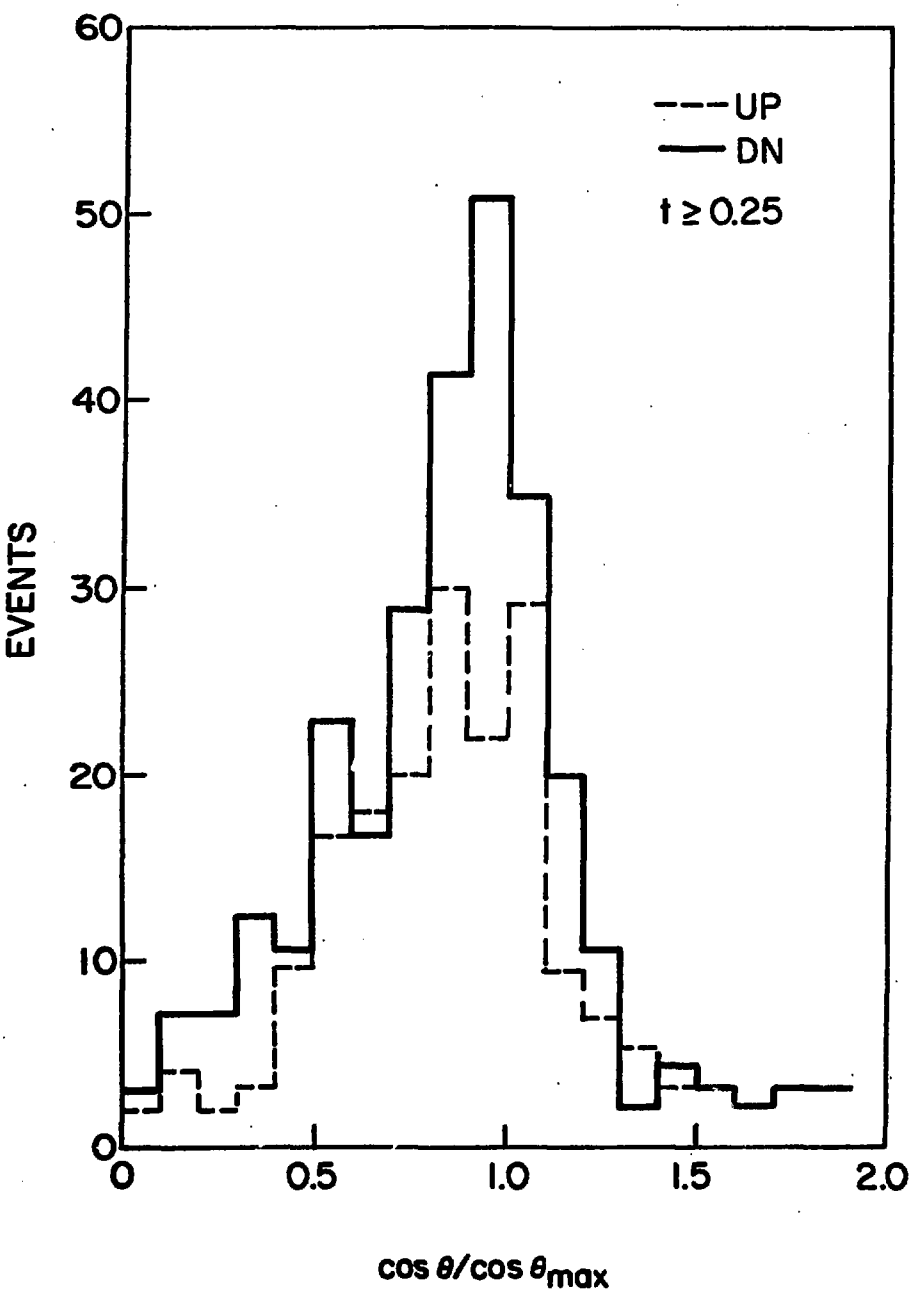

Fig. 40.

Fig. 40.--Same as Figure 39, for Events with |t|>.25

III. Overall Check Using Four-Constraint Fit

A. Detection Efficiency

Systematic error could be introduced in the polarization measurement if the detection efficiency for tracks within the Λ^o decay cone angle were not uniform. For example, if the efficiency were uniform (constant) then for U true "up" events only cU are detected, and for D true down events only cD are detected.

$$P_{expt.} = \frac{2}{\alpha} \frac{cU-cD}{cU+cD} = \frac{2}{\alpha} \frac{U-D}{U+D} = P_{true} \qquad \text{(IV-3)}$$

If the detection efficiency was not constant, then of U true up events only c_1U are detected, and of D true down events only c_2D are detected. Then

$$P_{expt.} = \frac{2}{\alpha} \frac{c_1U-c_2D}{c_1U+c_2D} \neq P_{true} \qquad \text{(IV-4)}$$

For events in which both the p and π^- from the Λ^o decay are detected in the side spark chambers, it is possible to do a four constraint fit and find all kinematic quantities for all final state particles. Thus, we can plot the c.m. decay angular distribution of protons about the scattering plane normal. This distribution (from Expression IV-1) is $N = 1+\alpha P\cos\theta$. We can see how well the actually measured distribution is fit by a straight line of arbitrary slop (slope here corresponds to polarization, the quantity to be measured). If there are gross deviations we can say that the efficiency is not uniform. Figure 41 shows the data split into two t regions. Figure 42 shows the same comparison for the data split into t bins of width .1.

Within the statistical errors, we can draw a straight line through these distributions. Accordingly, we can conclude that there are no significant systematic effects on the polarization

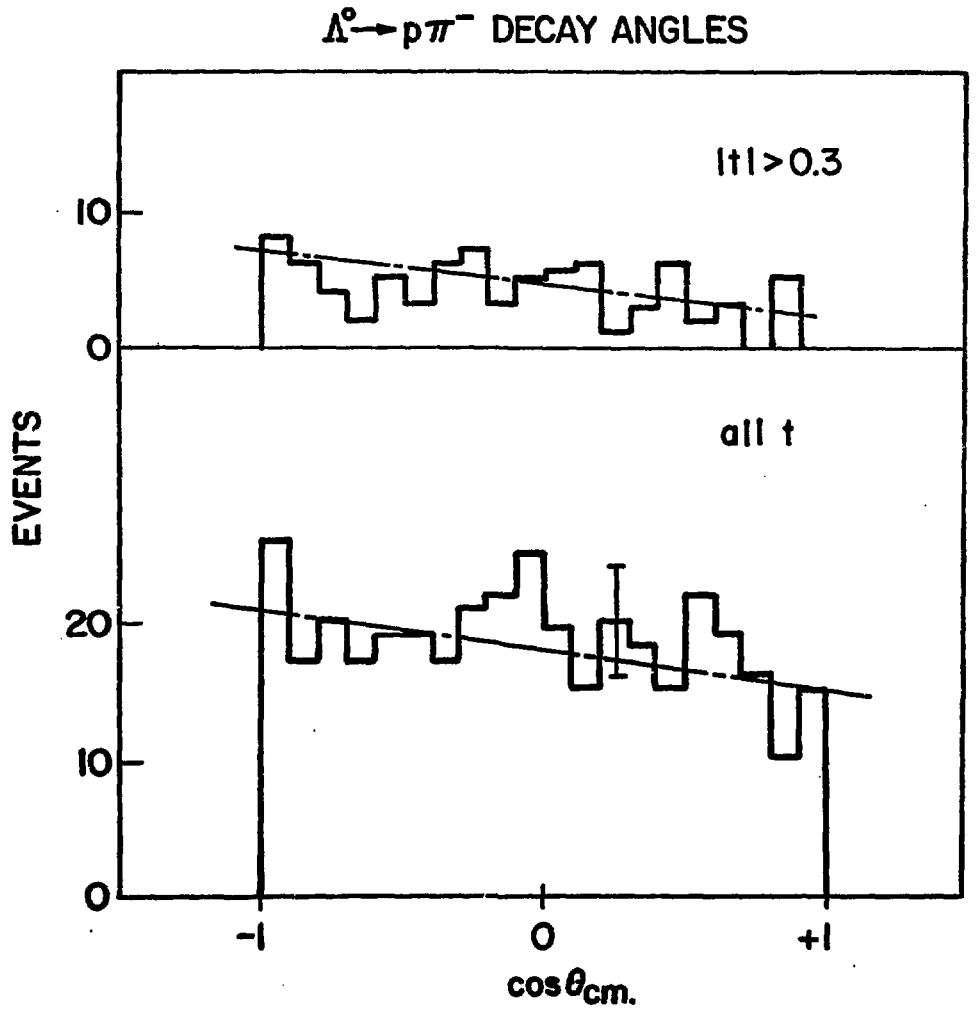

Fig. 41.

Fig. 41.--Distribution of Proton Decay Angles for $\Lambda^{\circ} \to p\pi^{-}$, Measured in the Λ Center of Mass Frame, where the Λ was Produced in $\pi^{-} p \to K\Lambda$

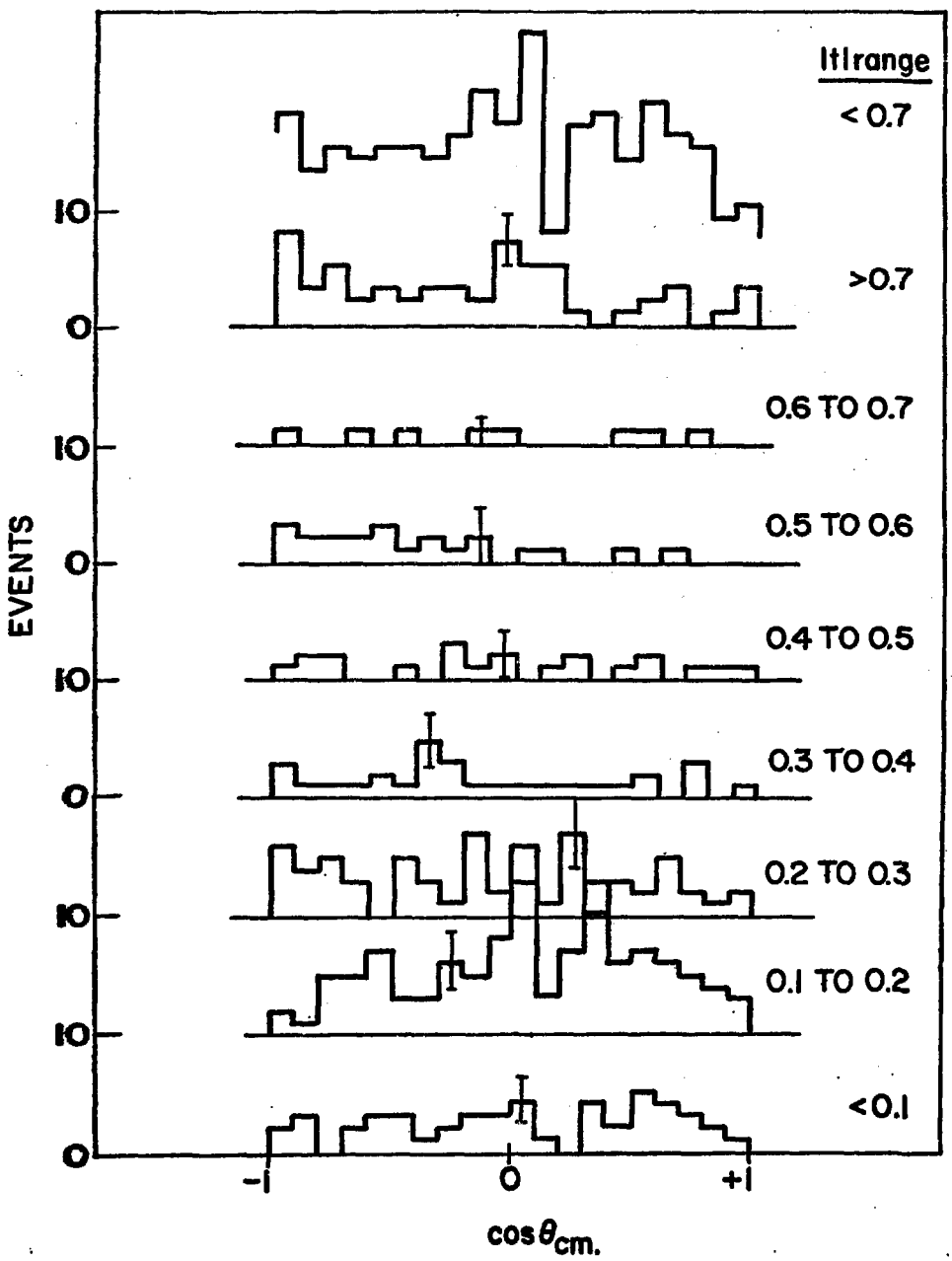

Fig. 42.

Fig. 42.--Same as Figure 41, where the Nine Distributions Show Events having Ranges in t between $|t| \leq .1$ and $|t| \geq .7$

measurement due to detection efficiency.

B. Calibration of Angle Measurements

We can also use the 4-C fit as an overall check as follows. We use the fit to calculate the angle of the proton from the Λ° decay, and compare it with the angle actually measured in the Λ° chamber. A systematic error would result in a distribution of these differences which was not centered at zero. The width of this distribution is a measure of the resolution in the angle measurement in the Λ° chamber.

Figure 43 shows the deviation of fitted from measured angles, horizontal and vertical, in bins of events per 4 milliradians. Overall shifts of the peaks of these distributions from zero are of order $\sim$4 milliradians. This is very small compared to the average opening angle in the Λ° decay, which is $\sim$50 milliradians, and would not significantly affect the measured polarization.

It is possible to do a four constraint fit to the reaction $\pi^- p \to K^\circ \Lambda^\circ$ only for those events which have both decay products of $\Lambda^\circ \to p\pi^-$ detected in the Λ° chamber. We have drawn a typical such event in Figure 3 and can briefly demonstrate this. Of the 21 quantities needed to completely specify the kinematics of the reaction (3 quantities per particle, 7 particles) we measure 13. These are-- 3 momentum components for the incident and decay pions from the K°, and 2 angles for the decay proton and pion from the Λ°. Included as assumptions in the fit are the masses of particles and the momentum of the target proton. The four equations of energy-momentum conservation can separately be applied at three

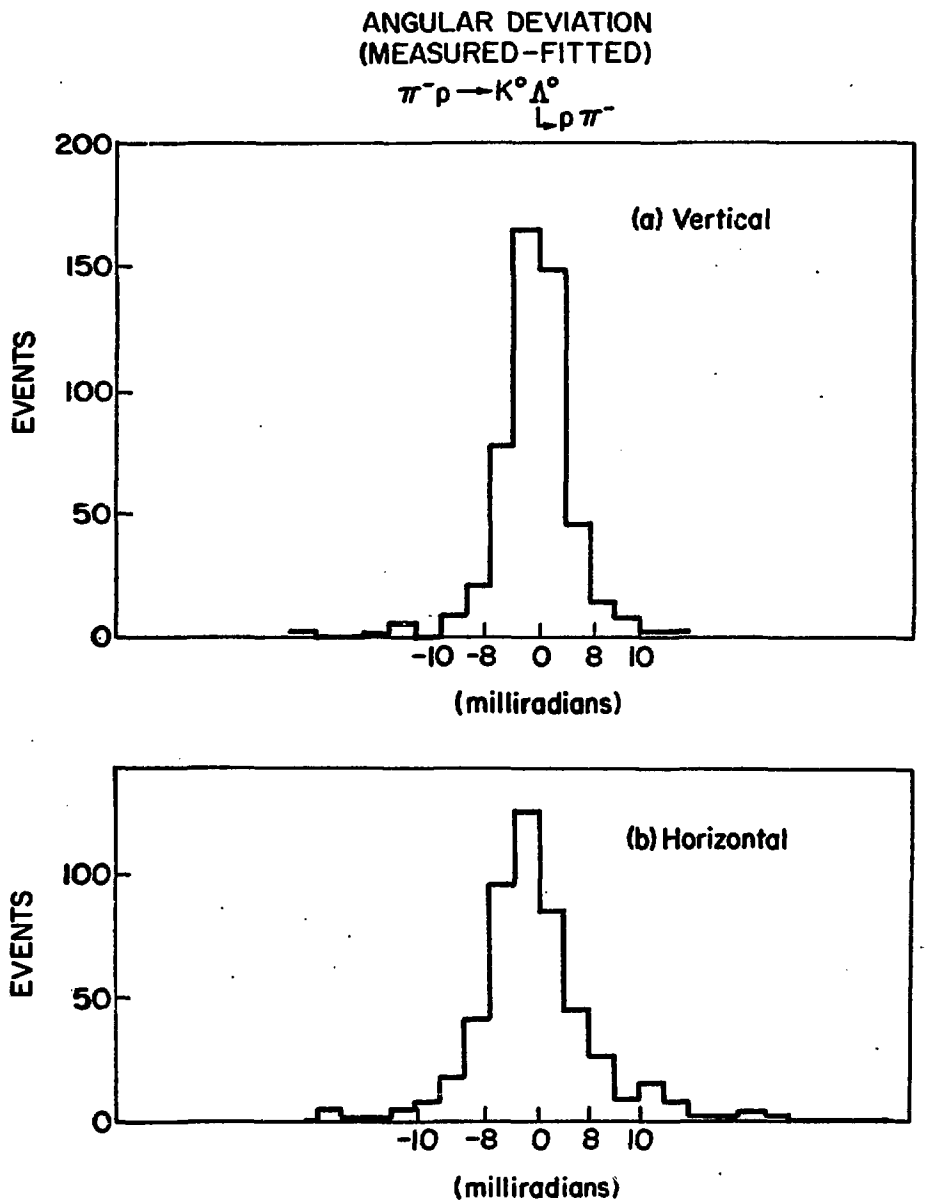

Fig. 43.

Fig. 43.-- The Decay $\Lambda^\circ \rightarrow p\pi^-$. Deviations of the Calculated Proton Angles (Obtained by a Four Constraint fit to the Λ Reaction) from the Measured Proton Angles

places, the production point, the decay point of the K°, and the decay point of the Λ°. This gives a total of 25 quantities either measured or calculated, when only 21 are needed for complete kinematic specification, resulting in a four constraint fit.

The constraints manifest themselves as (1) the requirement that the two decay pions detected in the spectrometer have invariant mass equal to the K° mass, (2) the requirement that the recoiling ("missing") mass be equal to the Λ° mass, and the requirements that the decay particles of $\Lambda^{\circ} \rightarrow p\pi^{-}$ have (3) the correct opening angle and (4) be co-planar with the Λ° particle. Roughly a third of the events used for the Λ° polarization measurement (obtained by the Mode 3 running condition) were of the kind that a 4-C fit was possible. These events were primarily used to study the systematic errors. For example, polarization was calculated by means of the cos θ distribution in the Λ° rest frame (Figure 41 and 42) rather than the "up" "down" distributions described earlier. In addition, the 4-C fit was used to work backwards to try to find possible shifts in the Λ° chamber alignment constants. Finally, detailed comparisons were made between several distributions for the 4-C events and for the remaining Mode 3 events. We found no evidence for any systematic difference between the two categories of events, or any systematic error in the measurement technique.

IV. Conclusion

In conclusion, we believe we have considered the possible sources of systematic error which might affect our polarization

measurement. We particularly were interested in investigating this at values of t greater than 0.8 $(Gev/c)^2$, where our data (Figure 45) shows the measured values exceeding 1.0 in absolute value. Our studies using the 4-C fit to the Λ° reaction, of the instrumental asymmetries using the elastic scattering data, of the possible alignment errors and of dead spots in the Λ° chambers, all led to the conclusion that the apparatus had no statistically significant non zero asymmetry. Our measured polarization points which exceeded 1.0 in absolute value could only be explained as a statistical fluctuation in the measured up-down asymmetry.

CHAPTER V

PRESENTATION OF RESULTS AND DISCUSSION

I. Features of the Data

We present the results of our measurements of $d\sigma/dt$ for the two reactions $\pi^- p \to K^o \Lambda^o$ and $\pi^- p \to K^o \Sigma^o$ in Table 6 and in Figure 44. The results of the Λ^o polarization measurement in $\pi^- p \to K^o \Lambda^o$ (the so called mode 3 data) is presented in Table 7 and Figure 45. The errors shown are statistical only, and do not include the systematic errors of $\sim \pm 10\%$, arising from the overall normalization procedure (Chapter III).

We point out the following common features in our data:

A. Diffraction Peak

The differential cross sections are well represented by an exponential of the form $\frac{d\sigma}{dt} = Ae^{bt}$ for $|t| < .4$. The slope parameters b for the forward peaks are given in Table 8. We note that the Σ^o cross section falls more rapidly than that of the Λ^o, but that both reactions show the same general shape.

B. Energy Dependence

In Table 8 and 9, and Figure 46 and 47 we show the energy dependence of the slope parameter b, and of the integrated differential cross section $\sigma_{tot} = \int_{t_{min}}^{t_e} \frac{d\sigma}{dt} dt$ where $|t_e|$ is .9, 1.3,

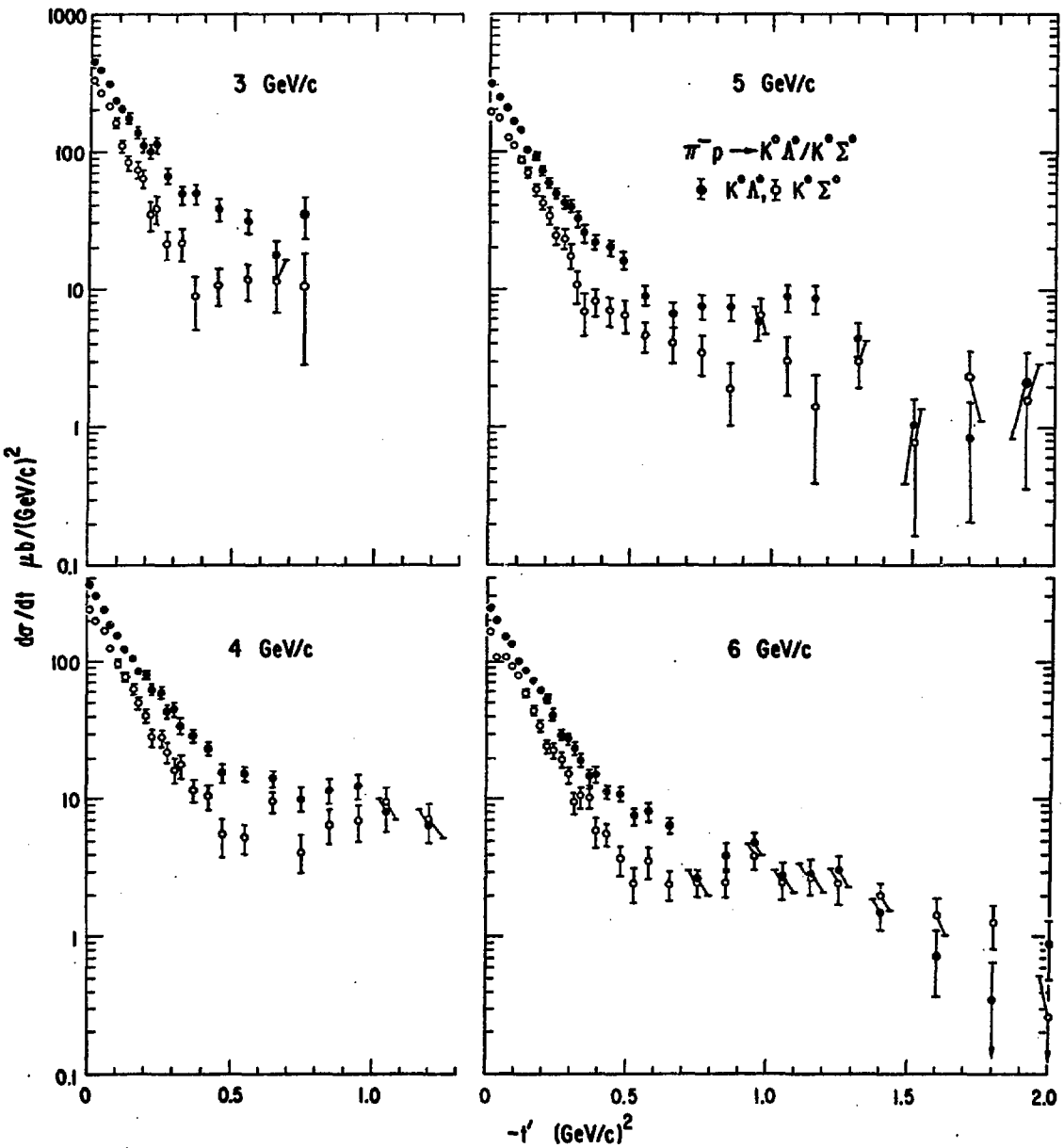

Fig. 44.

Fig. 44.--The Measured Differential Cross Sections

TABLE 6

DIFFERENTIAL CROSS SECTIONS,
IN $\mu b/(GEV/C)^2$

3.0 GeV/c			5.0 GeV/c			6.0 GeV/c		
-t'	$d\sigma(\Lambda)/dt$	$d\sigma(\Sigma)/dt$	-t'	$d\sigma(\Lambda)/dt$	$d\sigma(\Sigma)/dt$	-t'	$d\sigma(\Lambda)/dt$	$d\sigma(\Sigma)/dt$
.0125	438. ±16.	318. ±15.	.0125	303. ±11.	192. ±10.	.0125	245. ±8. 1	161. ±7. 3
.0375	380. ±16.	262. ±14.	.0375	247. ±10.	176. ±9. 7	.0375	200. ±7. 2	108. ±5. 9
.0625	301. ±14.	211. ±13.	.0625	204. ±9.0	129. ±8. 2	.0625	150. ±6. 1	110. ±5. 8
.0875	225. ±13.	161. ±12.	.0875	165. ±8. 1	111. ±7. 6	.0875	133. ±5. 7	91. 2±5. 2
.1125	202. ±14.	110. ±11.	.1125	143. ±7. 5	87. 9±6. 8	.1125	99. 1±4. 8	77. 9±4. 7
.1375	171. ±13.	83. 7±10.	.1375	103. ±6. 4	70. 1±6. 1	.1375	85. 1±4. 4	58. 4±4. 0
.1625	137. ±13.	73. 3±10.	.1625	94. 3±6. 2	51. 9±5. 3	.1625	71. 0±4. 0	43. 8±3. 5
.1875	111. ±12.	62. 8±10.	.1875	71. 5±5. 4	41. 8±4. 8	.1875	60. 7±3. 7	34. 3±3. 1
.2125	101. ±12.	34. 4±7. 9	.2125	58. 8±5. 0	33. 7±4. 4	.2125	51. 6±3. 4	24. 2±2. 6
.2375	112. ±14.	37. 5±8. 6	.2375	48. 9±4. 6	24. 0±3. 9	.2375	41. 5±3. 0	23. 0±2. 5
.275	65. 2±8. 1	21. 3±4. 9	.2625	41. 8±4. 4	23. 4±3. 9	.2625	29. 4±2. 6	19. 9±2. 3
.325	47. 9±7. 6	21. 6±5. 3	.2875	39. 4±4. 3	17. 8±3. 5	.2875	27. 8±2. 5	15. 3±2. 1
.375	48. 3±8. 2	8. 8±3. 8	.3125	31. 5±4. 0	10. 6±2. 9	.3125	23. 7±2. 3	9. 4±1. 8
.45	37. 1±5. 6	10. 5±3. 1	.3375	24. 8±3. 6	6. 8±2. 4	.3375	19. 3±2. 1	10. 3±1. 8
.55	30. 4±5. 7	11. 7±3. 6	.375	21. 9±2. 5	8. 1±1. 9	.3625	14. 3±1. 9	10. 2±1. 8
.65	17. 4±5. 0	11. 4±4. 7	.425	19. 9±2. 6	6. 9±1. 8	.3875	15. 4±2. 0	5. 8±1. 5
.75	34. 3±11.	10. 7±7. 9	.475	16. 1±2. 4	6. 4±1. 8	.425	11. 4±1. 2	5. 6±1. 0
			.55	8. 9±1. 4	4. 5±1. 1	.475	11. 0±1. 3	3. 75±. 91
4.0 GeV/c			.65	6. 5±1. 3	4. 0±1. 1	.525	7. 5±1. 1	2. 48±. 77
			.75	7. 4±1. 5	3. 5±1. 1	.575	8. 0±1. 2	3. 56±. 92
.0125	368. ±11.	246. ±9. 7	.85	7. 3±1. 6	1. 95±. 95	.65	6. 41±. 81	2. 44±. 58
.0375	302. ±10.	200. ±8. 6	.95	5. 7±1. 5	6. 4±1. 7	.75	2. 67±. 60	2. 55±. 58
.0625	242. ±8. 8	168. ±7. 9	1. 05	8. 7±1. 9	3. 0±1. 3	.85	3. 90±. 75	2. 51±. 62
.0875	186. ±7. 6	127. ±6. 8	1. 15	8. 5±2. 0	1. 4±1. 0	.95	4. 81±. 89	3. 95±. 81
.1125	158. ±7. 1	97. 4±6. 1	1. 30	4. 4±1. 1	3. 1±1. 1	1. 05	2. 82±. 72	2. 52±. 67
.1375	125. ±6. 4	75. 6±5. 5	1. 50	1. 01±. 62	. 77±. 61	1. 15	2. 91±. 77	2. 76±. 73
.1625	107. ±6. 1	61. 8±5. 1	1. 70	. 82±. 71	2. 3±1. 2	1. 25	3. 10±. 81	2. 47±. 73
.1875	84. 1±5. 6	50. 2±4. 8	1. 90	2. 1±1. 3	1. 6±1. 3	1. 40	1. 50±. 45	2. 02±. 48
.2125	78. 6±5. 7	40. 5±4. 5				1. 60	. 72±. 36	1. 46±. 44
.2375	61. 8±5. 3	28. 3±3. 9				1. 80	. 35±. 31	1. 27±. 45
.2625	59. 2±5. 5	28. 4±4. 1				2. 00	. 89±. 40	. 26±. 27
.2875	43. 4±4. 8	22. 2±3. 7						
.3125	45. 1±5. 1	16. 6±3. 4						
.3375	34. 6±4. 6	17. 5±3. 5						
.375	29. 1±3. 2	11. 6±2. 2						
.425	23. 7±3. 0	10. 4±2. 2						
.475	15. 8±2. 6	5. 4±1. 7						
.55	15. 5±2. 0	5. 3±1. 2						
.65	14. 4±2. 1	9. 6±1. 8						
.75	9. 9±1. 9	4. 2±1. 3						
.85	11. 3±2. 3	6. 4±1. 8						
.95	12. 4±2. 6	6. 9±2. 0						
1. 05	8. 0±2. 3	9. 6±2. 7						
1. 20	6. 6±1. 8	7. 1±2. 0						

Momentum GeV/c	Intercept a	Slope b
3.0 (Λ)	476. ±14.	7. 39±. 28
3.0 (Σ)	371. ±13.	10. 07±. 40
4.0 (Λ)	391. 4± 8. 8	7. 79±. 19
4.0 (Σ)	279. 2± 8. 0	9. 06±. 25
5.0 (Λ)	333. 0± 8. 6	7. 95±. 20
5.0 (Σ)	232. 9± 8. 2	9. 17±. 28
6.0 (Λ)	261. 8± 6. 0	7. 95±. 17
6.0 (Σ)	176. 3± 5. 3	8. 56±. 22

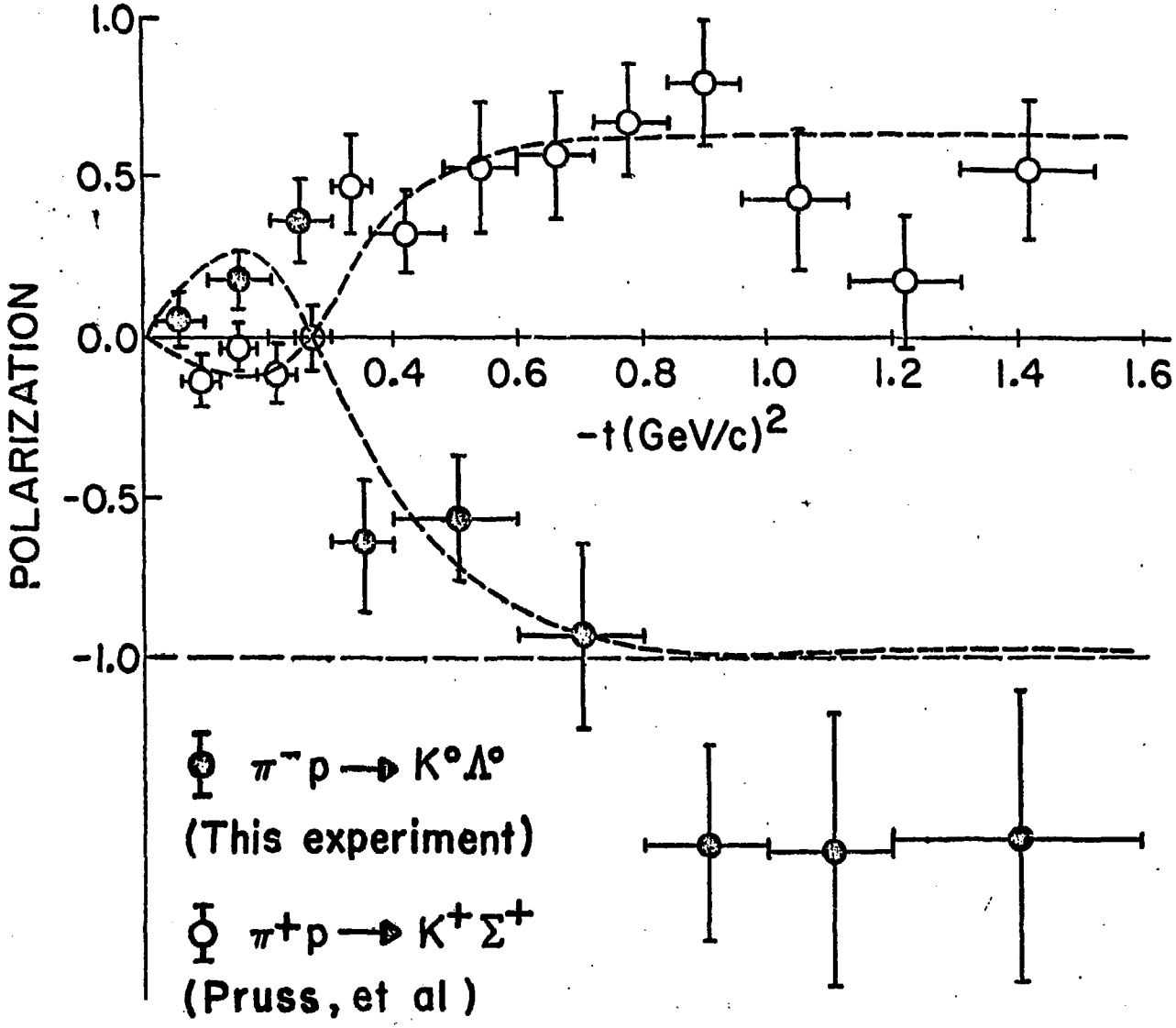

Fig. 45.

Fig. 45.--The Measured Λ° Polarization at 5 Gev/c. The Curves are to Guide the Eye and do not Represent any Model. Σ Polarization is also Shown for Comparison

TABLE 7

Λ^{o} POLARIZATION IN $\pi^{-}p \rightarrow K^{o}\Lambda^{o}$ at 5 GEV/C

-t	P	ΔP
0.055	0.045	±0.84
0.150	0.175	±0.091
0.250	0.364	±0.137
0.350	-0.641	±0.197
0.500	-0.566	±0.201
0.700	-0.930	±0.296
0.900	-1.57	±0.300
1.100	-1.59	±0.42
1.400	-1.55	±0.45

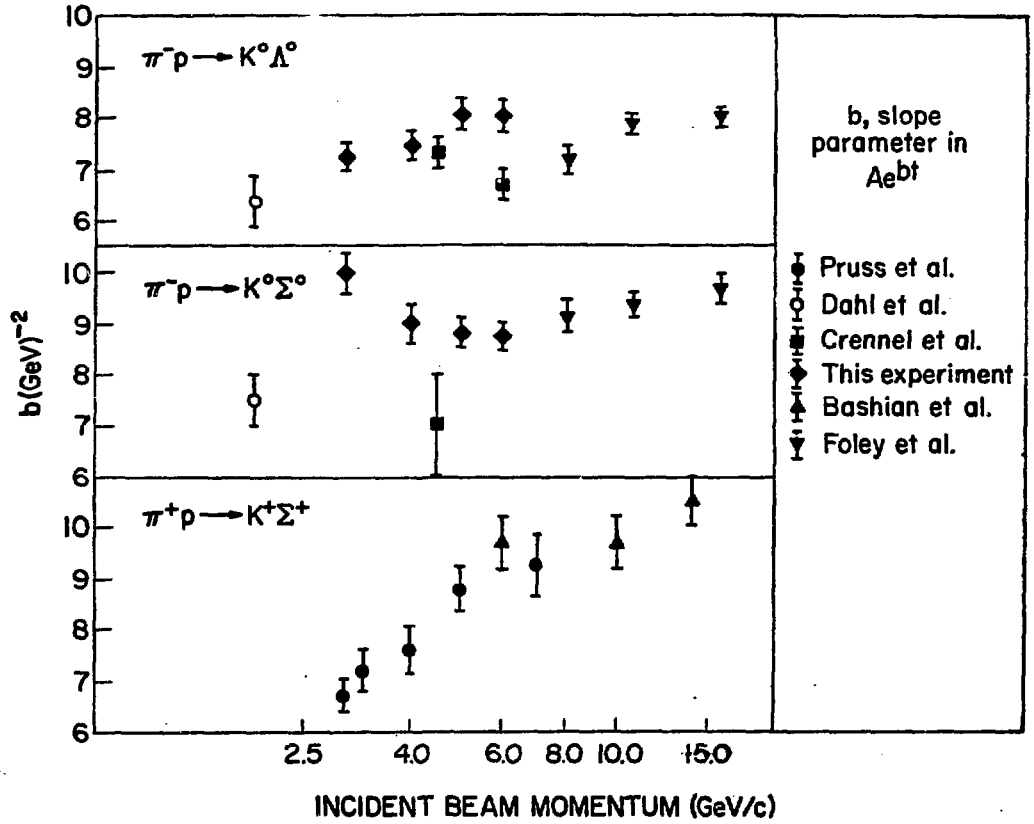

Fig. 46.

Fig. 46.--The Slope Parameter b in $d\sigma/dt=Ae^{bt}$ for Several Hypercharge Exchange Reactions

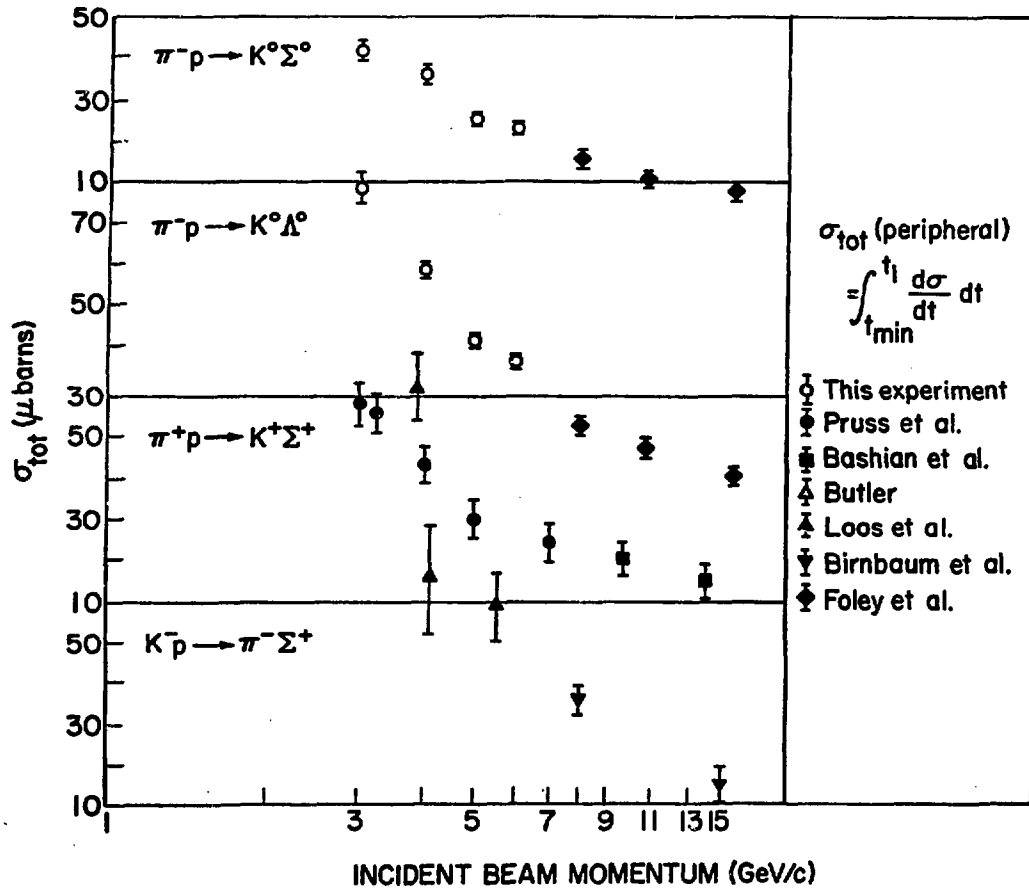

Fig. 47.

Fig. 47.--The Total Peripheral Cross Section for Several Hypercharge Exchange Reactions

TABLE 8

SLOPES AND INTERCEPTS A AND b IN FITTING CROSS SECTION WITH Ae^{bt}

Energy (GeV/c)	Reaction ($\pi p \to$)	A	b
4.5[a]	$K^o\Lambda^o$	318.±12.	7.3 ±.3
6.0[a]	$K^o\Lambda^o$	231.±14.	6.7 ±.3
4.5[a]	$K^*(890)\Lambda^o$	130.±11.	2.5 ±.2
6.0[a]	$K^*(890)\Lambda^o$	92.±14.	3.2 ±.4
4.5[a]	$K^o\Sigma^o$	186.±28.	7.0 ±1.0
4.5[a]	$K^*(890)$	52.±08.	2.1 ±.2
6.0[b]	$K^+\Sigma^+$	564.±26.	9.7 ±.5
10.0[b]	$K^+\Sigma^+$	265.±12.	9.7 ±.5
14.0[b]	$K^+\Sigma^+$	223.±11.	10.5 ±.5
6.0[b]	$K^+Y^*(1385)$	97.±12.	5. ±.5
10.0[b]	$K^+Y^*(1385)$	70.±10.	6.2 ±.6
14.0[b]	$K^+Y^*(1385)$	34.±05.	5.7 ±.6
1.9-2.1[c]	$K^o\Lambda^o$	-	6.4 ±.5
1.9-2.1[c]	$K^o\Sigma^o$	-	7.5 ±.5
3.0[d]	$K^+\Sigma^+$	500.±40.	6.4 ±.4
3.25[d]	$K^+\Sigma^+$	540.±40.	7.2 ±.4
4.0[d]	$K^+\Sigma^+$	430.±30.	7.6 ±.4
5.0[d]	$K^+\Sigma^+$	360.±40.	8.8 ±.5
7.0[d]	$K^+\Sigma^+$	320.±50.	9.3 ±.6
8.0[e]	$K^o\Lambda^o$	158.±04.	7.17±.23
10.7[e]	$K^o\Lambda^o$	117.±03.	7.85±.18
15.7[e]	$K^o\Lambda^o$	70.±02.3	7.97±.19
8.0[e]	$K^o\Sigma^o$	145.±04.	9.16±.32
10.7[e]	$K^o\Sigma^o$	103.±03.	9.38±.24
15.7[e]	$K^o\Sigma^o$	64.±03.	9.69±.24
3.0[f]	$K^o\Lambda^o$	476.±14.	7.39±.28
4.0[f]	$K^o\Lambda^o$	391.±09.	7.79±.19
5.0[f]	$K^o\Lambda^o$	333.±09.	7.95±.20
6.0[f]	$K^o\Lambda^o$	262.±06.	7.95±.17
3.0[f]	$K^o\Sigma^o$	371.±13.	10.07±.4
4.0[f]	$K^o\Sigma^o$	279.±08.	9.06±.25
5.0[f]	$K^o\Sigma^o$	233.±08.	9.17±.28
6.0[f]	$K^o\Sigma^o$	176.±05.	8.56±.22

[a] Crennel et al. Ref. 56
[b] Bashian et al. Ref. 57
[c] Dahl et al. Ref. 41
[d] Pruss et al. Ref. 37
[e] Foley et al. Ref. 58
[f] This experiment

TABLE 9

TOTAL PERIPHERAL CROSS SECTIONS $\pi^- p \to K^o \Lambda^o/\Sigma^o$

Energy	σ_{tot} for Λ^o (μb)	σ_{tot} for Σ^o (μb)
3[a]	78.96±2.79	41.72±1.73
4[a]	58.88±0.92	35.86±0.73
5[a]	41.66±0.41	25.39±0.37
6[a]	36.48±0.44	23.59±0.36
8[b]	22.1	16.7
10.7[b]	15.7	11.0
15.7[b]	9.1	7.0

[a]This experiment

[b]Foley et al. Ref. 58

2.0, 2.1 at incident beam momenta 3, 4, 5, and 6 GeV/c respectively. For comparison we also plot data from other hypercharge exchange reactions,[37,41,47,56-59] and at other measured energies. From Figure 46 there appears to be evidence for shrinkage in $\pi^+p\to K^+\Sigma^+$, but not in $\pi^-p\to K^oA^o$ or $\pi^-p\to K^o\Sigma^o$. The total cross section can be well represented by $\sigma\sim p_{lab}^{-1.7}$ for $K^+\Sigma^+$ and $K^o\Sigma^o$, and by $\sigma_{tot}\sim p_{lab}^{-2.1}$ for K^oA^o.

C. Break in $\frac{d\sigma}{dt}$ at $t\sim.4$

At $|t|\sim.4$ the differential cross sections have a change in slope, becoming much less steep. We also note that the polarization of the A^o changes sign at $|t|$ close to .4.

D. No Turnover of $\frac{d\sigma}{dt}$ at Small t

As t approaches t_{min} the spin flip amplitude $f_\pm$ must vanish, since it is not possible to define scattering plane at t_{min}.

$$\frac{d\sigma}{dt} = |f_\pm|^2+|f_\pm|^2$$

It is possible to infer the relative magnitudes of f_+ and f_- by looking for turnover in $\frac{d\sigma}{dt}$ at small t. Our data confirms the evidence from other hypercharge exchange reactions, namely, that these reactions are dominated by the spin non-flip amplitude, since no turnover is present. We compare our data with previous bubble chamber measurements, which had much lower statistical precision. Figure 48 shows our data at 4 GeV/c compared with the measurement of Abramovich et al.[60] at 3.9 GeV/c. Figure 49 shows our data at 6 GeV/c compared to D. Crennel et al.[61] Both comparisons show good agreement.

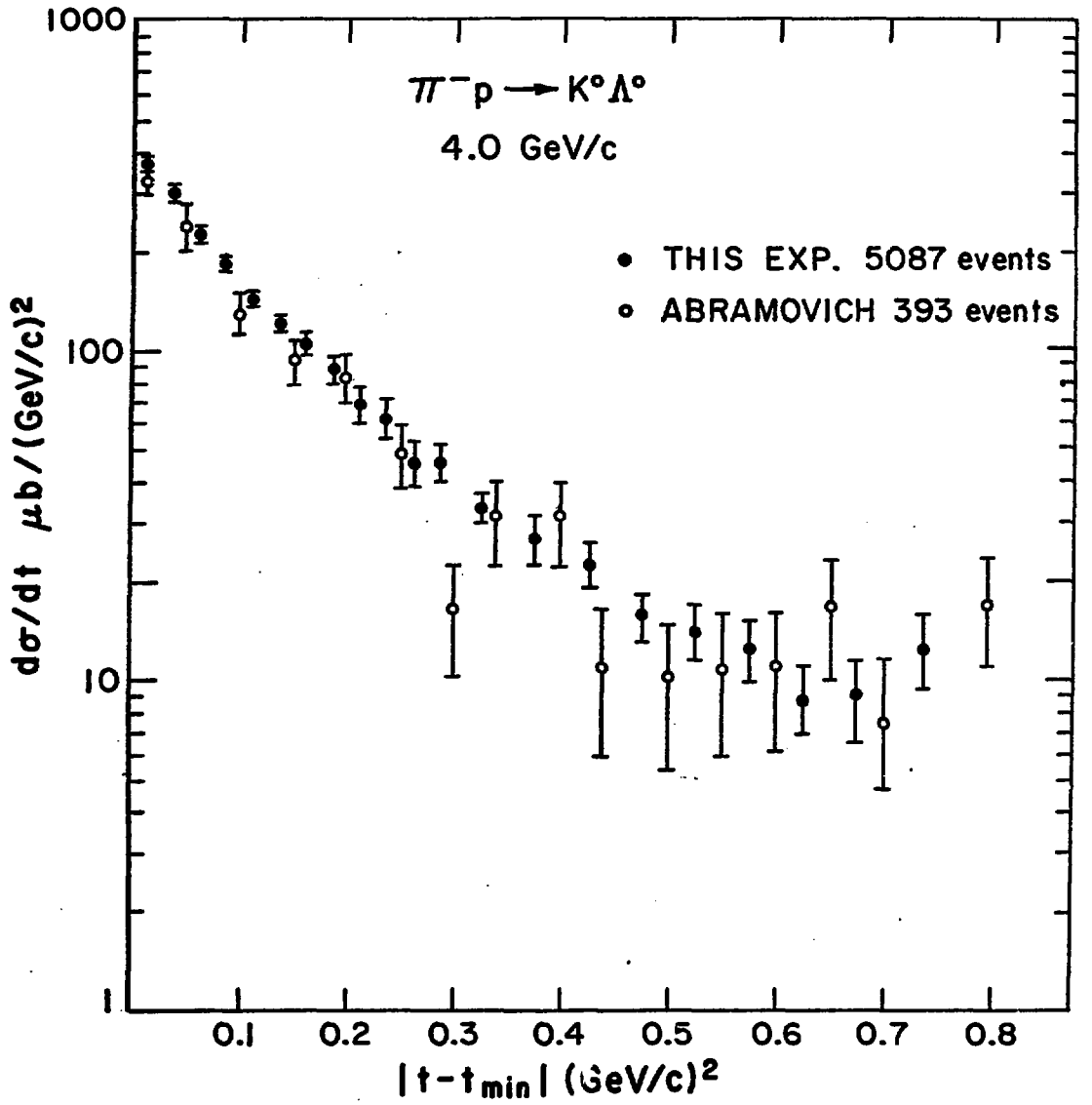

Fig. 48.

Fig. 48.--Comparison of 4 Gev/c Data with Abramovich, Ref. 60

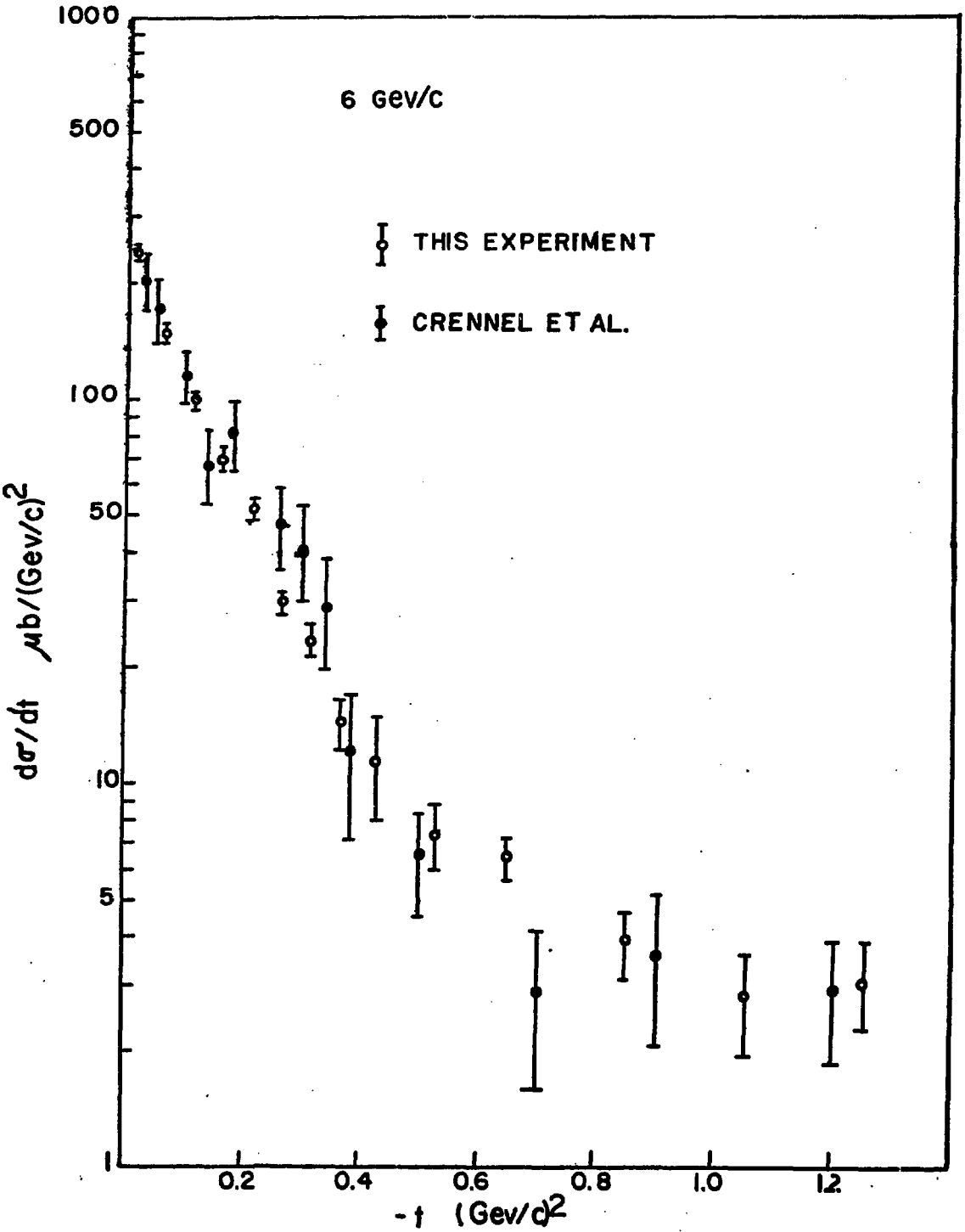

Fig. 49.

Fig. 49.--Comparison of 6 Gev/c Data with Crennel, Ref. 61

II. I = 1/2 Exchange

The charge independence of strong interactions relates the cross sections in the three following reactions by the triangle inequality:

$\pi^+ p \to K^+ \Sigma^+$ (1)

$\pi^- p \to K^o \Sigma^o$ (2) $\qquad \frac{d\sigma}{dt}$: (1)+(2)$\geq$(3)

$\pi^- p \to K^+ \Sigma^-$ (3)

According to charge independence, the amplitudes (determined from t-channel exchanges) may be expanded in terms of intermediate states of total isospin. The only possible values of the i-spin for the exchanges possible in the 3 above reaction are: I = 1/2, 3/2. Hence,

$$\text{Amplit } (K^+\Sigma^+) = 1/3\ T_{3/2} + 2/3\ T_{1/2}$$

$$\text{Amplit } (K^o\Sigma^o) = 2/3\ T_{3/2} - 2/3\ T_{1/2}$$

$$\text{Amplit } (K^+\Sigma^-) = T_{3/2}$$

$T_{3/2}$ and $T_{1/2}$ denote the amplitudes for I = 3/2, I = 1/2 exchange, respectively. The coefficients are the Clebsch-Gordan coefficients for the coupling of spins. There is no experimental evidence for the existence of an I = 3/2 (exotic) meson, (Akerlof, Ref. 40) hence, we set $T_{3/2} = 0$. This gives the result that the cross section for the $K^o\Sigma^o$ reaction should be 1/2 that of the $K^+\Sigma^+$ reaction. We make this comparison in Figure 50, and conclude that there is no appreciable I = 3/2 component present.

The absence of the $T_{3/2}$ amplitude is the justification in the amplitude analysis for setting the polarization in $\pi^- p \to K^o \Sigma^o$ (not measured) equal to the polarization in $\pi^+ p \to K^+ \Sigma^+$, (Pruss et al., Ref. 37).

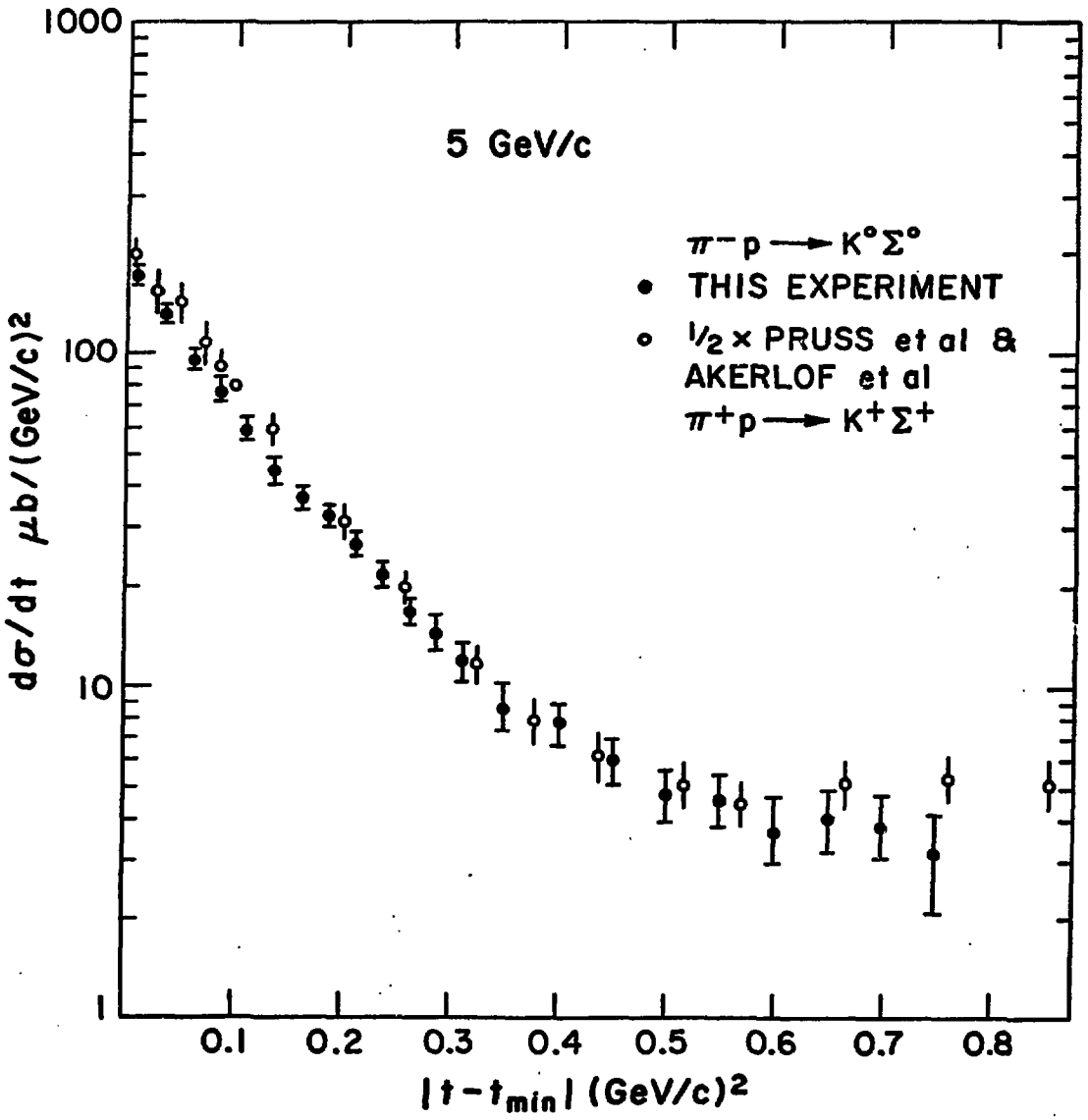

Fig. 50.

Fig. 50.--Comparison of Differential Cross Sections for $\pi^- p \to K^\circ \Sigma^\circ$ and $\pi^+ p \to K^+ \Sigma^+$, Demonstrating Negligible Contribution of I=3/2 Exchange to the Amplitude

III. Models

As mentioned in Chapter I, there do exist models that can represent the hypercharge exchange data.

Regge pole models[62-63] assume that the reactions are dominated by the t-channel exchange of the K^* (890) and the K^{**} (1420) trajectories, and that these two are approximately coincident (Exchange Degeneracy, Ref. 63). The cross section is then expressed as

$$\frac{d\sigma}{dt} = f(t)s^{\alpha_{eff}(t)-2} \qquad \text{(V-1)}$$

where α_{eff} is the effective trajectory function for the combined K^* (890) and K^* (1420) poles. Figure 51, taken from Reference 64, shows α_{eff} and includes our data.

The assumption of exchange degeneracy leads to the predictions that: (1) pairs of reaction related by the reversal of meson lines, e.g.,

$\pi N \to KY$ N - nucleon

$KN \to \pi Y$ Y - hyperon

should have equal differential cross sections. 2) The polarization is predicted to be zero. In the region 4 - 8 GeV/c, prediction (1) is violated by a factor of 2. At 14 GeV/c there is conflicting experimental evidence[48,59,65-66] on this point, with the prediction satisfied at 14 GeV/c, but violated by a factor of 2 at 16 GeV/c. The polarization is found to be non zero over the t-range. In the Regge models the non zero polarization may be obtained by "weak" exchange degeneracy, which is a relaxation of the requirements placed on the residues f(t) in V-1. The residues are not required to be equal for exchange of the K^* and the K^{**} trajectories.

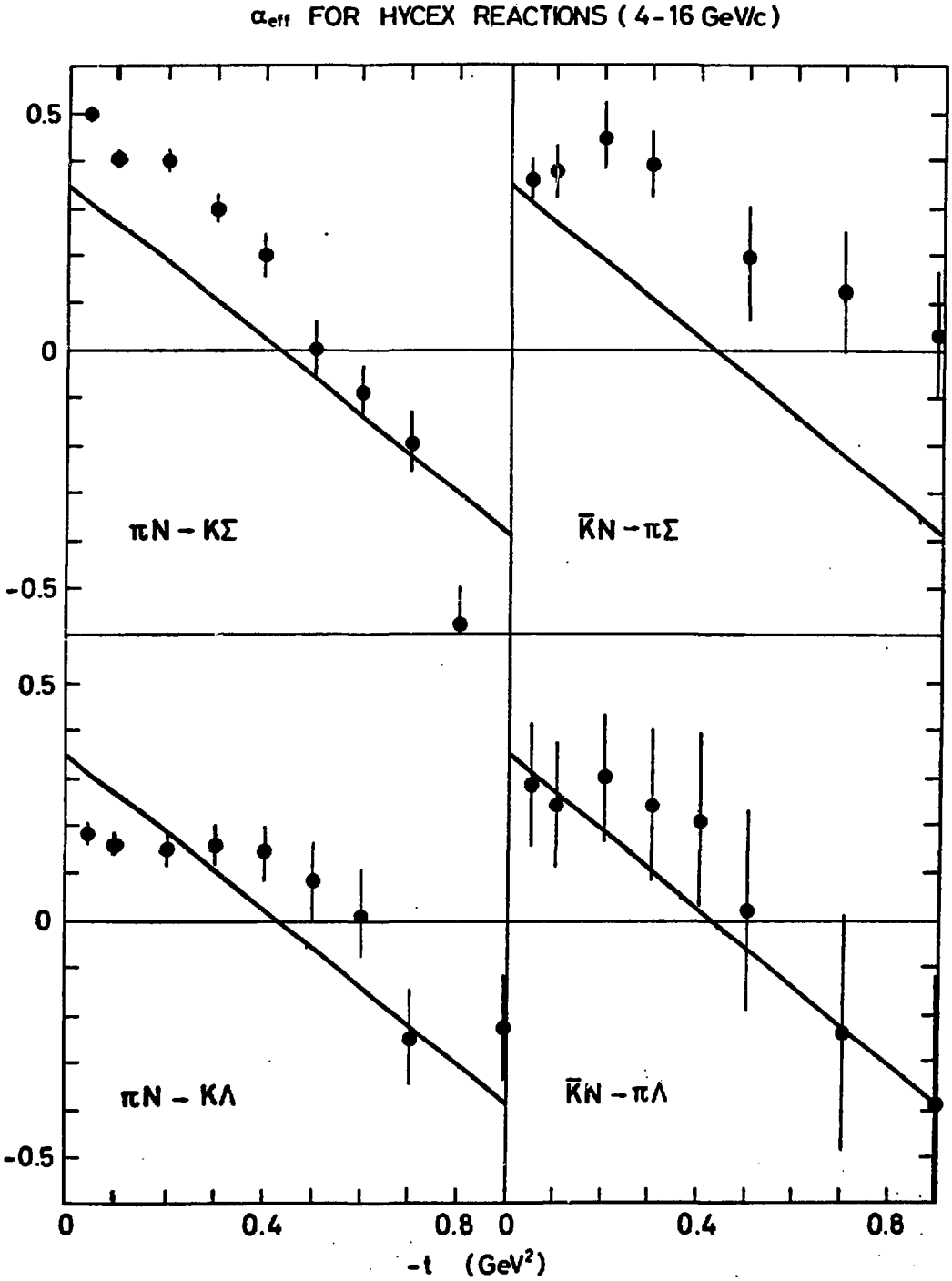

Fig. 51.

Fig. 51.--Effective Regge Trajectories for Hypercharge Exchange Reactions, from Ref. 64

Non equality of line reversed reaction may be obtained by allowing non-coincident K^* and K^{**} trajectories, with equal residue factors f(t). This seems unlikely, however.

There are other models,[67-68] involving cuts and absorption. Exchange degeneracy is not assumed here, and the hypercharge exchange data is well represented. However, these models require a large number of parameters to be determined from the data.

IV. Qualitative Observations

In conclusion, we would like to make some qualitative observation about the hypercharge exchange (HCEX) reactions, with reference to elastic scattering processes.

There are certain regularities in HCEX data (Figure 44) which bear some resemblance to elastic scattering (Figure 52). Both show sharp exponential falloff of $\frac{d\sigma}{dt}$, a break, and a flattening out in $\frac{d\sigma}{dt}$ at the larger t. For HCEX the break takes place at t $\sim$.4, while for πp elastic scattering the break is at t $\sim$.6. For πp elastic scattering the slope of the forward peak is 7 - 9 (GeV^{-2}) and shows slight energy dependence. For HCEX there is energy dependence in the $K^+\Sigma^+$ channel, but not in the K^oA^o and $K^o\Sigma^o$ channels. The HCEX slope parameters are in the range 6 - 9 GeV^{-2}. The total cross section of the HCEX falls more rapidly with energy than for the elastic scattering processes. If $\sigma_{tot} \sim p_{lab}^{-n}$ then $n \gtrsim .2$-.4 for elastic scattering, while $n \gtrsim 1.5$-2.5 for HCEX.

There are additional resemblances when we compare the

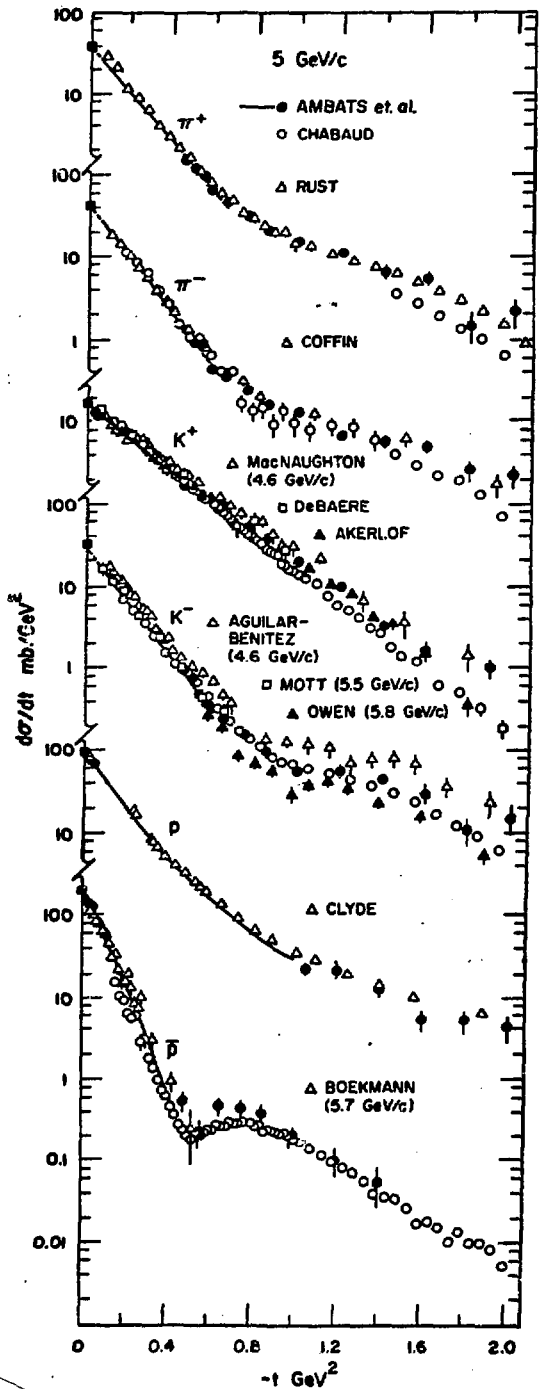

Fig. 52.--Compilation of Data on Elastic Scattering, from Ref. 69, to be Compared with Hypercharge Exchange Data in General Features

polarization data for HCEX and elastic processes. $\pi^{\pm}p$ elastic polarizations (Figure 53) shows the striking mirror symmetry about zero. Figure 45 shows a similar symmetry for the HCEX reactions $\pi^{+}p \rightarrow K^{+}\Sigma^{+}$ and $\pi^{-}p \rightarrow K^{o}\Lambda^{o}$. In addition, the zero in the polarization occur at t values where there are breaks in the differential cross section.

These resemblances are interesting in view of the extensive data currently available over a very wide energy range for both elastic scattering processes, and hypercharge exchange processes.

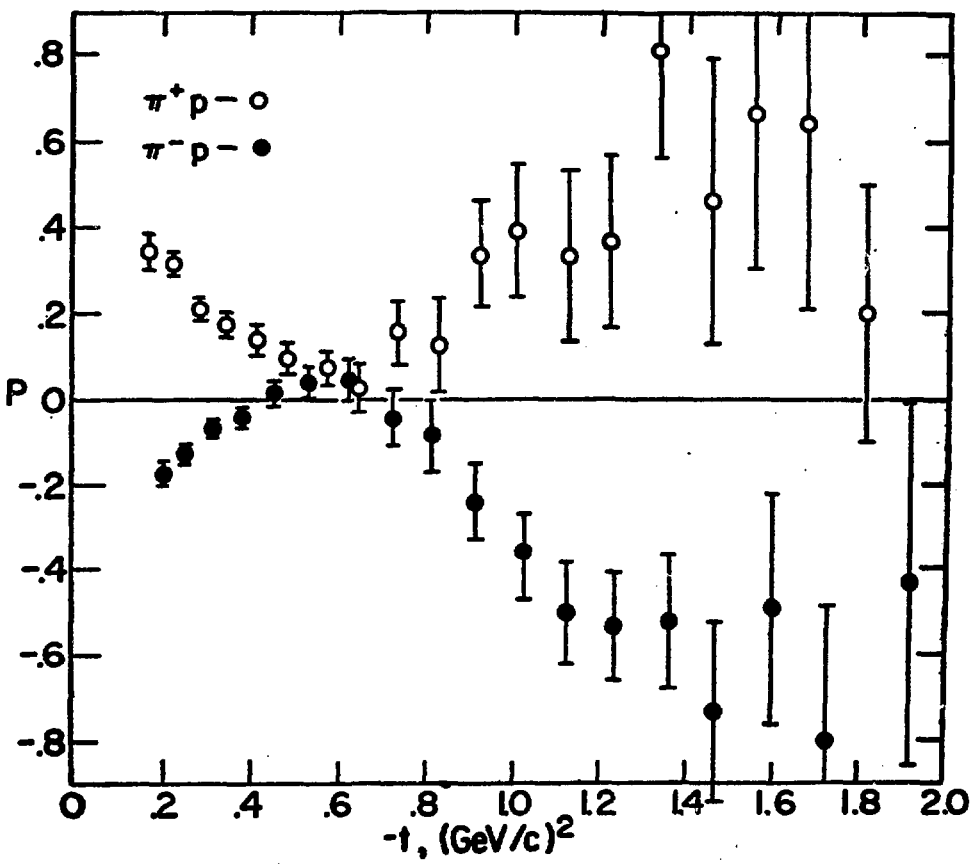

Fig. 53.

Fig. 53.--Polarization in πp Elastic Scattering, for Comparison with Hypercharge Exchange Polarization Data (Fig. 45). Fig. 53 is from Esterling et al., Ref. 70

APPENDIX

AMPLITUDE ANALYSIS*

Under the assumption of unbroken SU(3) symmetry and of K^* exchange in the t-channel, it is possible to specify the amplitudes for the following hypercharge exchange reactions:

Reaction	Measured Quantity	Energy Range
$\pi^- p \to K^o \Lambda^o$	$P, \frac{d\sigma}{dt}$	5,3-6 GeV/c
$\pi^- p \to K^o \Sigma^o$	$P^{**}, \frac{d\sigma}{dt}$	3-6 GeV/c

For complete specification of the amplitudes, the real and imaginary parts of the spin flip and spin non-flip amplitudes must be found for each reaction. Since there is an indeterminate overall phase, only three numbers are required (in each process). The measurements above give two quantities for each reaction. The following describes the method for applying SU(3) symmetry at the baryon-meson-baryon vertex in the scattering diagram (below), used to obtain the remaining two quantities needed for the complete amplitude analysis.

---

*See D. R. Rust and C. E. W. Ward (to be published)

**Polarization data taken from Pruss et al. $\pi^+ p \to K^+ \Sigma^+$, Ref. 37.

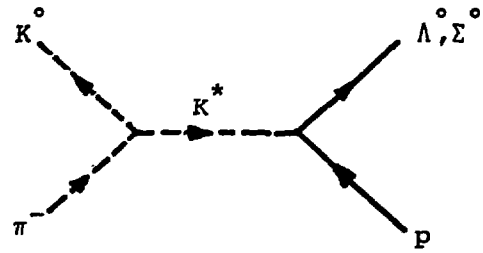

(I-1)

From the assumption that the Λ,Σ,K^* belong in SU(3) octets, only two types of independent couplings are possible--denoted by the F and D couplings. SU(3) Clebsch-Gordan (C-G) coefficients are then used to find the relative coupling strenghts at the baryon vertex for the Λ and Σ reactions (above).

In general, for the scattering diagram shown the decay at the vertex V is represented as follows:

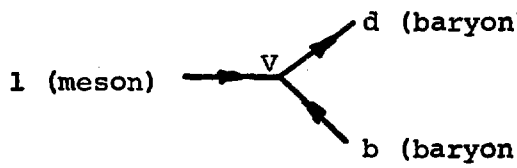

$$B_d^8 \rightarrow B_b^8 + M_1^8 \qquad \text{(I-2)}$$

The B^8 and M^8 stand for the baryon and meson SU(3) octets, respectively, and the subscripts stand for the quantum numbers (Y,I,Iz). At the vertex V, the coupling G giving the relative strength with which two members of the B_d^8 octet, (namely the Λ and Σ) couple to the B_b^8 and M_1^8 octets is:

$$G = \text{const. } A \cdot B \cdot C \cdot D$$

where:

A = a sum over all possible coupling constants, multiplied by appropriate SU(3) C-G coefficients.

B = Phase space factor. (I-3)

C = SU(3) symmetry breaking factor.

D = Model dependent barrier factor.

In this application, all factors except A are neglected. For

the reactions we have measured, then:

$$G = g_F \langle (YII_z)^8_1 (YII_z)^8_b | (YII_z)^8_F \rangle + g_D \langle (YII_z)^8_1 (YII_z)^8_b | (YII_z)^8_D \rangle \qquad \text{(I-4)}$$

where the quantities inside the brackets are the SU(3) C-G coefficients. These are reducible to products of SU(3) isoscalar factors and the usual C-G i-spin factors. Referring to the wallet card, we have for the Λ and Σ reactions:

$$G(\Lambda^o \to pK^*) = \underbrace{(-\sqrt{10}/10 g_D + \sqrt{2}/2 g_F)}_{\text{SU(3) isoscalar factors}} \underbrace{\sqrt{2}/2}_{\text{i-spin factor}} \qquad \text{(I-5)}$$

$$G(\Sigma \to pK^*) = (-\sqrt{30}/10 g_D + \sqrt{6}/6 g_F)\ 2/2$$

$$G(N \to N\pi) = (3/2\sqrt{5} g_D + 1/2 g_F)$$

As a definition we set: $G(N \to N\pi) \equiv D+F$

hence: $g_D = 2\sqrt{5}/3D$ and $g_F = 2F$

This gives, $$\frac{G(\Lambda \to pK^*)}{G(\Sigma \to pK^*)} = \frac{1/3D+F}{1/\sqrt{3}(-D+F)} \qquad \text{(I-6)}$$

and setting $x = F/D$, $(x_{\pm} = F_{\pm}/D_{\pm})$ gives, $R = G(\Lambda)/G(\Sigma) =$

$$(3x+1)/(\sqrt{3}(x-1)) \qquad \text{(I-7)}$$

The measured quantities $\frac{d\sigma}{dt}$ and P are expressible in terms of the spin flip amplitude f^+ and the spin non flip amplitude f^-, for each reaction.

$$\frac{d\sigma}{dt}(\Lambda) = |f^+_\Lambda|^2 + |f^-_\Lambda|^2$$

$$P\frac{d\sigma}{dt} = 2\mathrm{Im}(f^{+*}_\Lambda f^-_\Lambda) \qquad \text{(I-8)}$$

Rewriting (I-7):

$$f_\Lambda = (3x+1)f$$

$$f_\Sigma = \sqrt{3}(x-1)f \qquad \text{(I-7')}$$

gives:

$$\begin{aligned}
\frac{d\sigma}{dt}(\Lambda^o) &= (3x_+ + 1)^2 |f^+|^2 + (3x_- + 1)^2 |f^-|^2 \\
\frac{d\sigma}{dt}(\Sigma^o) &= 3(x_+ - 1)^2 |f^+|^2 + 3(x_- - 1)^2 |f^-|^2 \\
P\frac{d\sigma}{dt}(\Lambda^o) &= 2(3x_+ + 1)(3x_- + 1)\,\mathrm{Im}(f^{+*} f^-) \\
P\frac{d\sigma}{dt}(\Sigma^o) &= 6(x_+ - 1)(x_- - 1)\,\mathrm{Im}(f^{+*} f^-)
\end{aligned} \qquad \text{(I-9)}$$

f^- must vanish at zero scattering angle (since no scattering plane is then defined), this gives,

$$\frac{\frac{d\sigma}{dt}(\Lambda^o)_o}{\frac{d\sigma}{dt}(\Sigma^o)_o} = \frac{(3x_+ + 1)^2}{3(x_+ - 1)^2} \qquad \text{(I-10)}$$

and this ratio is obtainable from our data. Moreover, by using the relation $P\frac{d\sigma}{dt}(\Lambda^o)/P\frac{d\sigma}{dt}(\Sigma^o) = (3x_+ + 1)(3x_- + 1)/6(x_+ - 1)(x_- - 1)$, x_- can also be obtained from the data. Using our data at 5 GeV/c incident beam momentum, and also using the polarization data of Pruss et al. at 5 GeV/c, the following values are obtained:

$$x_+ = -2.74 \pm 0.17$$

$$x_- = +0.491 \pm 0.118$$

$$|f^+|^2 = .0283\frac{d\sigma}{dt}(\Sigma^o) - .0036\frac{d\sigma}{dt}(\Lambda^o)$$

$$|f^-|^2 = .194\frac{d\sigma}{dt}(\Lambda^o) - .241\frac{d\sigma}{dt}(\Sigma^o)$$

$$\sin\phi_{+-} = \pm\frac{P\,\frac{d\sigma}{dt}(\Lambda^o)}{35.71|f^+||f^-|}$$

The magnitude and phase of the amplitude obtained by this method is presented in Figure 54.

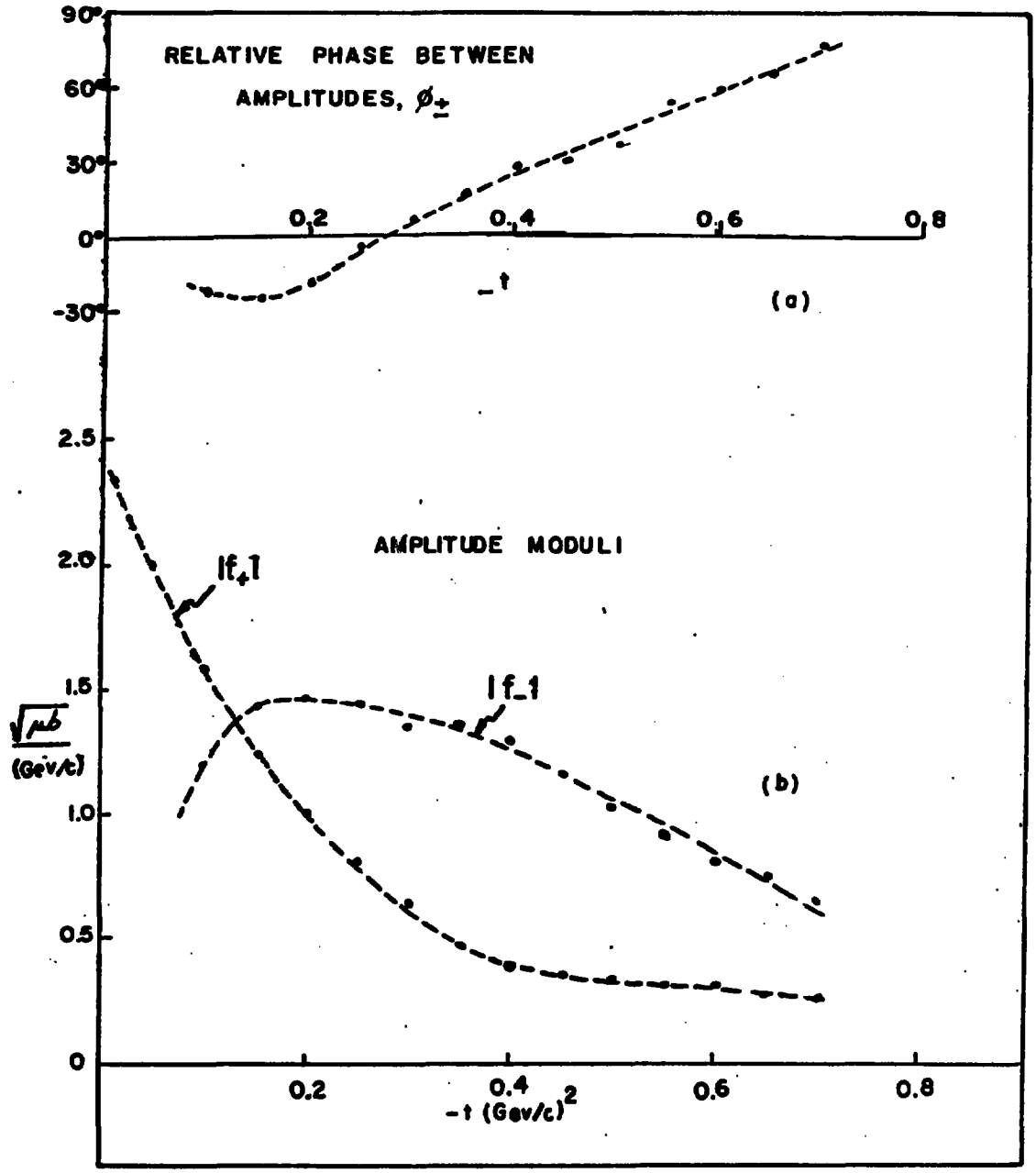

Fig. 54.

Fig. 54.--Amplitude Moduli and Phase for Hypercharge Exchange Reactions, from the Amplitude Analysis of Rust and Ward, Ref. 22

LIST OF REFERENCES

[1]L. Le Prince-Rinquet and M. Lheritier, Compt. Rend. 219, 618 (1949). Also see R. W. Thompson, A. V. Buskirk, L. R. Etter, C. J. Karzmark and R. H. Redikes, Phys. Rev. 90, 1122 (1953).

[2]This principle states that reactions must proceed at the same rate in either direction at thermodynamic equilibrium.

[3]A. Pais, Phys. Rev. 86, 663 (1952).

[4]R. L. Garwin, Phys. Rev. 90, 274 (1953). W. B. Fowler et al., Phys. Rev. 93, 861 (1954). W. D. Walker, Phys. Rev. 98, 1407 (1955). C. M. York et al., Phys. Rev. 90, 157 (1953). A. Bonetti et al., Nuovo Cimento 10, 1736 (1953). E. W. Cowan, Phys. Rev. 94, 161 (1954).

[5]M. Gell-Mann, Nuovo Cimento Suppl. 4, 2, 848 (1956). K. Nishijima, Progr. Theoret. Phys. (Kyoto) 13, 285 (1955).

[6]Foley et al., Ref. 58.

[7]See rapporteur reviews: C. Michael, in Proceedings of the Oxford Conference on High Energy Collisions, (1972). R. J. N. Phillips, in Proceedings of the Amsterdam Conference on Elementary Particles, (1972).

[8]W. Rarita, R. J. Riddell, Jr., Charles B. Chiu, and R. J. N. Phillips, Phys. Rev. 165, 1615 (1968).

[9]B. Amblard, thesis (1971).

[10]O. Guisan, Proceedings of the Rencontre de Muriond sur les interaction electro-magnetitiques, March 1971.

[11]P. Bonamy et al., Phys. Lett. 23, 501 (1966).

[12]F. Halzen and C. Michael, Phys. Lett. 36B, 367 (1971).

[13]G. Ringland and D. P. Roy, Phys. Lett. 36B, 443 (1971).

[14]V. Barger and R. J. N. Phillips, Phys. Rev. 187, 2210 (1969).

[15]V. Barger and F. Halzen, Phys. Rev. D6, 1918 (1972).

[16]B. J. Hartley and G. Kane, Phys. Lett. 39B, 531 (1972).

[17]M. Ross, Phys. Lett. 38B, 321 (1972).

[18]R. C. Johnson, Phys. Lett. 38B, 325 (1972).

[19]A. Martin and P. R. Stevens, Phys. Rev. D5, 158 (1972).

[20]J. Anderson and K. J. M. Moriarity, Royal Holloway preprint RHCM 71/4 (1972).

[21]V. Barger, K. Geer, and F. Halzen, Nucl. Phys., (to be published).

[22]D. R. Rust and C. E. W. Ward, (to be published).

[23]S. Mandelstam, Phys. Rev. 115, 1344 (1959).

[24]See for example: W. S. C. Williams, An Introduction to Elementary Particle Physics (Academic Press, 1941), p. 400. R. J. Eden, High Energy Collisions of Elementary Particles (Cambridge University Press, 1967).

[25]G. F. Chew, M. L. Goldberger, F. E. Low and Y. Nambu, Phys. Rev. 106 1337 (1957).

[26]V. Barger and D. Cline, Phenomenological Theories of High Energy Scattering (W. A. Benjamin, 1969), p. 43.

[27]Rust and Ward, Ref. 22.

[28]C. Goebel, Phys. Rev. Lett. 1, 337 (1958).

[29]G. F. Chew and F. E. Low, Phys. Rev. 113, 1640 (1959).

[30]J. V. Allaby et al., Phys. Lett. B27, 49 (1968).

[31]H. Kanada, T. Kobayashi, and V. Sumi, Progr. Theoret. Phys. (Kyoto) Supp. 1 41, 42, (1967).

[32]Barger and Cline, Ref. 26.

[33]L. Van Hove, Phys. Lett. 24B, 183 (1969).

[34]L. Durand, Phys. Rev. 161, 1610 (1967).

[35]See for example: R. J. N. Phillips and G. A. Ringland, High Energy Physics (Academic Press, 1972) Vol. V.

[36]V. Barger, Rev. Mod. Phys. 40, 129 (1968).

[37]S. M. Pruss, C. W. Akerlof, D. I. Meyer, S. P. Ying, J. Lales, R. A. Lundy, D. R. Rust, C. E. W. Ward and D. D. Yovanovitch, Phys. Rev. Lett. 23, 189 (1969).

[38]R. R. Kobler, R. W. Hartung, and D. D. Reeder, Phys. Rev. 163, 1479 (1967).

[39]J. Badier et al., Saclay Report, (1966).

[40]P. Kalbaci et al., Phys. Rev. Lett. 27, 74 (1971).

[41]O. I. Dahl et al., Phys. Rev. 163, 1430 (1967).

[42]V. Barger and D. Cline, Phys. Rev. 156, 1522 (1967).

[43]S. Meshkov, G. A. Snow, and G. B. Yodh, Phys. Rev. Lett. 12, 87 (1964); 13, 213 (1964); H. Harari and H. J. Lipkin, ibid. 13, 208 (1964). J. Leitner, Syracuse University Report No. ONR-66-1, (unpublished).

[44]V. Barger and M. Olsson, Phys. Rev. Lett. 18, 294 (1967).

[45]See for example: Frazer, Introduction to Elementary Particle Physics, p. 85.

[46]Barger and Cline, Ref. 42.

[47]J. S. Loos and J. A. J. Mathews, SLAC Report No. SLAC-PUB-1068.

[48]H. Harari, "Phenomenological Duality", SLAC-PUB-914.

[49]H. Harari, Phys. Rev. Lett. 26, 1400 (1971).

[50]Halzen and Michael, Ref. 12.

[51]Rust and Ward, Ref. 22.

[52]David R. Rust, "On-Line Computer Facilities at Argonne", ANL/HEP 7025 (1970).

[53]Charles E. W. Ward, "An On-Line Software Package for the Argonne EMR-6050 Computers", ANL/HEP 7206 (1972).

[54]Arthur B. Wicklund, "Analysis of Particle Orbits in Magnetic Spectrometers", ANL Internal Report (1971).

[55]D. R. Rust, Argonne Internal Report (1972).

[56]D. J. Crennel et al., Phys. Rev. D6, 1220 (1972).

[57]A. Bashian et al., Phys. Rev. D4, 2667 (1972).

[58]K. Foley et al., BNL Report 16681 (1973).

[59]D. Birnbaum et al., Phys. Lett. 31B, 484 (1969).

[60]M. Abramovich et al., Nucl. Phys. B22, 477 (1971).

[61]Crennel et al., Ref. 56.

[62]D. D. Reeder and K. V. L. Sarma, Phys. Rev. 172, 1566 (1968).

[63]R. C. Arnold, Phys. Rev. 153, 1506 (1967).

[64]A. C. Irving et al., CERN preprint 1585 (1972).

[65]R. J. Miller et al., RHEL Ecole Polytechnique, Saclay preprint, Batavia Conference (1972).

[66]E. H. Willen et al., Brookhaven Lab. preprint BNL 16681 (1972).

[67]P. R. Auvil et al., Phys. Lett. 31B, 303 (1970).

[68]F. S. Henyee et al., U. of Michigan preprint (1971), and also Phys. Rev. 182, 1579 (1969).

[69]I. Ambats et al., to be published in Phys. Rev. D.

[70]R. J. Esterling et al., Phys. Rev. Lett. 21, 1420 (1968).